ELECTROCHEMICAL OXYGEN TRANSFER REACTION ON SYNTHETIC BORON-DOPED DIAMOND THIN FILM ELECTRODE

THÈSE N° 3057 (2004)

PRÉSENTÉE À LA FACULTÉ SCIENCES DE BASE

Institut des sciences et ingénierie chimiques

SECTION DE CHIMIE ET GÉNIE CHIMIQUE

ÉCOLE POLYTECHNIQUE FÉDÉRALE DE LAUSANNE

POUR L'OBTENTION DU GRADE DE DOCTEUR ÈS SCIENCES

PAR

Béatrice MARSELLI

chimiste diplômée de l'Université de Genève, Suisse
et de nationalité française

acceptée sur proposition du jury:

Prof. C. Comninellis, directeur de thèse
Prof. A. De Battisti, rapporteur
Dr C. Pulgarin, rapporteur
Prof. M. Rodrigo, rapporteur

Lausanne, EPFL
2004

Remerciements

Ce travail de thèse a été réalisé dans le laboratoire de génie électrochimique à l'EPFL. Mes remerciements vont tout d'abord à son directeur, le Professeur Christos Comninellis pour m'avoir permis de faire mon doctorat au sein de son groupe, pour son aide scientifique, sa disponibilité et pour ses nombreux conseils. Je le remercie également de m'avoir offert la possibilité de participer à de nombreuses conférences.

Merci aux autres membres du jury: Professeur Achille De Battisti, Professeur Manuel Rodrigo, Dr César Pulgarin pour l'intérêt qu'ils ont porté à ma thèse, et au président du jury: Professeur Claude Friedli.

Je voudrais aussi remercier le Centre Suisse d'Electronique et de Microtechnique à Neuchâtel pour avoir préparé les électrodes de diamant sans lesquelles rien n'aurait pu être fait. Merci aussi à toutes les personnes de l'atelier mécanique pour leur disponibilité et leur aide ainsi qu'à Pierre-André Perroud, pour le support informatique. Merci également à Madame Ingrid Margot et Madame Paule Anken, Sara et Vida pour le support administratif.

J'ai eu, tout au long de ma thèse, la chance de collaborer avec de nombreux diplômants, stagiaires et apprentis très motivés qui m'ont permis de faire avancer le projet à grands pas. C'est donc avec beaucoup de gratitude que je remercie Birame Boye, Mélanie Deillon, Daniel Fischer, Jesus García-Gómez, Mathias Kügele, Alessandro Mangione, Carlos Martinez-Huitle, Simone Mori, Lassiné Ouattara, Gabriele Prosperi, David Weissbrodt et Daniel Zollinger pour leur travail et leur bonne humeur.

La théorie, c'est quand on sait tout et que rien ne fonctionne.

La pratique, c'est quand tout fonctionne et que personne ne sait pourquoi.

Ici, nous avons réuni théorie et pratique: Rien ne fonctionne... et personne ne sait pourquoi.

Albert Einstein

Abstract

Synthetic boron-doped diamond thin film is a new promising anode material. Because of its properties (high anodic stability under drastic conditions and wide potential window), it is widely investigated for numerous possible electrochemical applications such as electrosynthesis, preparation of powerful oxidants and electroincineration. In the first part of this work, simple charge transfer was investigated at boron-doped diamond electrode through the study of an *outer sphere* system in the potential region of water stability. In a second part of this work, the electrochemical oxygen transfer reaction (EOTR) was studied in more details. Hydroxyl radicals are one of the most important intermediates produced during EOTR. Their formation depends on the electrode material as well as the potential and implies different mechanisms and reactivities. At low potential, hydroxyl radicals are produced by the dissociative adsorption of water followed by the hydrogen discharge. This reaction is assumed to take place at electrocatalytic material like platinum. When the potential is higher than 1.23 V vs *SHE* (thermodynamic potential of water decomposition in acidic medium), the water discharge occurs, leading to the formation of hydroxyl radicals. From this, two classes of materials can be distinguished: *active* and *non active* electrodes. It is well established that at *active* electrodes, a strong interaction with hydroxyl radicals exists and the EOTR occurs via the formation of an higher oxide. In contrast, at *non active* electrodes, the substrate does not participate in the process and the oxidation is assisted by hydroxyl radicals that are weakly adsorbed at the electrode surface. Assuming that hydroxyl radicals are the main intermediates of the reaction, a model was developed to predict the organic compounds oxidation (*COD-ICE* model). Another part of this work deals with the validation of the theoretical models.

In addition to the *COD-ICE* model, another model describing the oxidation reaction in terms of flux of both hydroxyl radicals and organics (γ–ν model) was developed. Both models permitted on the one hand to predict and describe the evolution of the oxidation reaction, and on the other hand to confirm the role of hydroxyl radicals. Moreover, it was possible to perform, depending on the conditions of applied current, either a partial oxidation (into intermediates) or a total incineration (into CO_2) of the organic compound.

The models, developed for a one-compartment electrochemical flow cell, were also validated in both a two-compartments cell and a new electrochemical cell, called turbine cell. In addition, the development of this cell allowed us to work with well established hydrodynamic conditions.

The wide potential window that exists at boron-doped diamond electrode (BDD) theoretically allows the formation of free hydroxyl radicals, whose redox potential is estimated at about 2.6 V (vs *SHE*). The principal aim of this work was to highlight the presence of hydroxyl radicals at BDD electrode and to study their reactivity. First, we have investigated the production of hydrogen peroxide and the competitive reaction of carboxylic acids, both of which indicated the presence of hydroxyl radicals. Then, spin trapping was performed to detect hydroxyl radicals. This method consists in trapping the radical with an appropriate scavenger to produce a stable adduct, which can be analyzed by different techniques such as electron spin resonance (*ESR*), *UV*-visible and liquid chromatography (*HPLC*) measurements. The spin trapping at BDD electrode was performed through three experiments, *viz.*, the electrolysis of a solution of 5,5-dimethyl-1-pyrroline-N-oxide (DMPO) or 4-nitroso-N,N-dimethylaniline (*p*-nitrosoaniline or RNO) and the hydroxylation of salicylic acid using *ESR*, *UV* and *HPLC* analysis, respectively. These results have confirmed the presence and the key role of hydroxyl radicals during oxidative processes at BDD electrode. The hydroxylation of salicylic acid, whose oxidation mechanism is well established and yields to two dihydroxylated isomers (2,3- and 2,5-DHBA), was investigated in more details to study the reactivity of hydroxyl radicals. The results were compared to the reactivity of hydroxyl radicals chemically produced by Fenton reaction and *UV*-photolysis. The comparison was based on the investigation of the isomer distribution. On the basis of our results and by analogy with chemical and biological results, a mechanism for salicylic acid hydroxylation was proposed.

Version Abrégée

Les fines couches synthétiques de diamant dopé au bore représentent un nouveau matériau d'électrode prometteur. Grâce à ses propriétés (stabilité anodique élevée sous des conditions drastiques et grande fenêtre de potentiel), ce type d'électrode est largement étudié pour de nombreuses applications électrochimiques telles que l'électrosynthèse, la préparation d'oxydants puissants et l'électroincinération. La première partie de ce travail traite du transfert de charge sur les électrodes de diamant dopé au bore, illustré par l'étude d'un système *sphère externe* dans la région de potentiel de stabilité de l'eau. Dans la seconde partie de ce travail, les réactions de transfert d'oxygène (EOTR) ont été étudiées en détail. Les radicaux hydroxyles sont un des intermédiaires les plus importants formés lors de ces réactions. Leur formation dépend non seulement du matériel de l'électrode mais aussi du potentiel impliquant différents mécanismes et réactivités. A bas potentiel, les radicaux hydroxyles sont produits par l'adsorption dissociative de l'eau, suivie de la décharge de l'hydrogène. Ce type de réaction a lieu sur des matériaux électrocatalytiques comme le platine. Lorsque le potentiel dépasse 1.23 V vs *SHE* (potentiel thermodynamique de la décomposition de l'eau en milieu acide), la décharge de l'eau se produit, formant des radicaux hydroxyles. Ainsi, deux classes de matériau d'électrode peuvent être distinguées: les électrodes *actives* et *non actives*. Sur une électrode *active*, une forte interaction avec les radicaux hydroxyles existe et le processus d'oxydation a lieu par la formation d'un oxyde supérieur. Dans le cas d'une électrode *non active*, le substrat ne participe pas au processus et l'oxydation est assistée par les radicaux hydroxyles qui sont faiblement adsorbés à la surface de l'électrode. En considérant que les radicaux hydroxyles sont les principaux intermédiaires de la réaction, un modèle a été développé afin de prédire l'oxydation de composés organiques (modèle *COD-ICE*). Une autre partie de ce travail concerne la validation des modèles théoriques.

Un autre modèle (modèle γ–ν) a aussi été développé. Celui-ci décrit la réaction d'oxydation en termes de flux des radicaux hydroxyles et des composés organiques. Les deux modèles ont permis d'une part de prédire et de décrire l'évolution de la réaction d'oxydation et d'autre part de confirmer le rôle des radicaux hydroxyles. De plus, il a été possible d'obtenir, selon le courant appliqué, soit une oxydation partielle (produisant de

nombreux intermédiaires), soit l'incinération complète en CO_2. Les modèles, développés pour une cellule électrochimique à un compartiment, ont aussi été validés pour une cellule à double compartiment ainsi que pour une nouvelle cellule électrochimique, appelée «turbine cell». Le développement de cette cellule nous a permis de travailler avec des conditions hydrodynamiques très bien établies.

La grande fenêtre de potentiel, présente sur les électrodes en diamant dopé au bore (BDD), permet théoriquement la formation de radicaux hydroxyles libres, dont le potentiel redox est estimé à environ 2.6 V (vs *SHE*). Le but principal de ce travail a été de mettre en évidence la présence des radicaux hydroxyles sur les électrodes BDD ainsi que d'étudier leur réactivité. Dans un premier temps, nous avons étudié la production du peroxyde d'hydrogène ainsi que les réactions compétitives. Ces deux expériences ont indiqué la présence des radicaux hydroxyles. Ensuite, le spin trapping a été réalisé pour détecter les radicaux hydroxyles. Cette méthode consiste à piéger le radical afin de produire un adduit stable, qui peut ensuite être analysé par différentes techniques comme la résonance paramagnétique électronique, les mesures par *UV*-visible ou chromatographie liquide. Le spin trapping des radicaux hydroxyles a été réalisé sur les BDD électrodes au moyen de trois expériences: par l'électrolyse d'une solution de 5,5-dimethyl-1-pyrroline-N-oxyde (DMPO) ou de 4-nitroso-N,N-dimethylaniline (*p*-nitrosoaniline ou RNO) et aussi par la réaction d'hydroxylation de l'acide salicylique en utilisant respectivement la *RPE*, l'*UV* and l'*HPLC* comme méthodes d'analyse. Ces résultats ont confirmé la présence et le rôle clé des radicaux hydroxyles. L'hydroxylation de l'acide salicylique, dont le mécanisme d'oxydation est bien connu et conduit à la formation de deux isomères dihydroxylés (2,3 et 2,5-DHBA), a été étudié en détail afin de comprendre la réactivité des radicaux en la comparant à celle des radicaux hydroxyles produits chimiquement par la réaction de Fenton et par *UV*-photolyse. La comparaison a été faite en étudiant la distribution des deux isomères. Sur la base de nos résultats et par analogie avec des résultats chimiques et biologiques, un mécanisme d'hydroxylation de l'acide salicylique (et plus généralement de composés organiques) a été proposé.

Table of symbols

1. ROMAN SYMBOLS

A	Surface electrode	m^2
a_N, a_H	Hyperfine coupling	G
COD	Chemical oxygen demand	$mol\ (O_2)\ m^{-3}$
COD^0	Initial value of chemical oxygen demand	$mol\ (O_2)\ m^{-3}$
d_h	Hydraulic diameter	m
D	Diffusion coefficient	$cm^2\ s^{-1}$
E	Potential of an electrode vs a reference	V
E^0	Standard potential	V
$E^{0'}$	Apparent potential	V
E_{eq}	Equilibrium potential	V
E_p	Peak potential	V
$E_{p/2}$	Half peak potential	V
e	Thickness	m
e^-	Electron	none
f	Frequency	$rad\ s^{-1}$
F	Faraday's constant	$C\ mol^{-1}$
h	Width	m
$HO^{\bullet}$	Hydroxyl radicals	none
i	Current intensity	A

Symbol	Description	Unit
i_0	Exchange current	A
i_p	Peak current	A
$i_{p/2}$	Half peak current	A
ICE	Instantaneous current efficiency	none
J	Flux of species	$mol\ m^2\ s^{-1}$
j	Current density	$A\ m^{-2}$
j_0	Exchange current density	$A\ m^{-2}$
j_{lim}	Limiting current density	$A\ m^{-2}$
k	Chemical rate constant	$M^{-1}\ s^{-1}$
k^0	Standard rate constant	$m\ s^{-1}$
k_f	Rate constant	$m\ s^{-1}$
k_m	Mass transport coefficient	$m\ s^{-1}$
L	Length	m
n	Number of exchanged electrons	none
O	Oxidized species	none
Q	Specific charge	$A\ s\ m^{-3}$
r	Rate of reaction	$mol\ m^2\ s^{-1}$
R	Reduced species	none
R	Gas constant	$J\ mol^{-1}\ K^{-1}$
R_{CT}	Charge transfer resistance	Ω
Re	Reynolds number	none
S	Selectivity	none
Sc	Schmidt number	none
Sh	Sherwood number	none
SHE	Standard hydrogen electrode	none
T	Temperature	K
t	Time	s
TOC	Total organic carbon	$mol\ (C)\ m^{-3}$
v	Scan rate	$V\ s^{-1}$
V	Volume	m^3
$\dot{V}$	Flow rate	$m^3\ s^{-1}$
X	Conversion	none

2. GREEK SYMBOLS

α	Anodic transfer coefficient	none
α	Dimensionless current density	none
β	Cathodic transfer coefficient	none
γ	Kinetics parameter	none
δ	Diffusion boundary layer	none
δ_v	Viscosity boundary layer	none
ε	Molar extinction coefficient	$L\ mol^{-1}\ cm^{-1}$
η	Overpotential	V
λ	Wavelength	nm
Λ	Parameter in cyclic voltammetry	none
ν	Stoechiometric factor	none
ν	Kinematic viscosity	$m^2\ s^{-1}$
ρ	Resistivity	$\Omega\ cm$
Ψ	Rate parameter in cyclic voltammetry	none
ω	Angular velocity	s^{-1}

3. SUPERSCRIPT

0	Initial
s	Relative to the surface electrode
*	Relative to the bulk
®	Registered trade mark

4. SUBSCRIPT

lim	Limiting value
i	Initial
p	Relative to a peak
a	Relative to an anodic process
c	Relative to a cathodic process
app	Applied

Table of Contents

Chapter 1. Introduction

One of the main preoccupation of the research in electrochemistry is the continuous development of high-quality and wear resistant electrode materials. This type of materials must fulfill specific characteristics such as long-term chemical and electrochemical stability, good electric conductivity, resistance to electrode deactivation and fouling, sufficient mechanical stability, technical feasibility of fabrication and acceptable cost [1]. One of the essential components of the electrochemical oxygen transfer reaction (EOTR) process is the anode, whose efficiency is primordial and depends strongly on the material used. In the recent past, the electrochemical research focused a lot on anode development in order to improve the electrochemical efficiency of the process. At the beginning, electrocatalytic anodes made of platinum or palladium were developed [2-4]. This kind of material implies adsorption steps and has a high efficiency, but the poisoning of the surface and the wear of the electrode render them less efficient.

The dimensional stable anode (DSA$^{®}$) technology was developed later, originally for the chlorine/alkali process. These electrodes are made of metallic oxides deposited on a titanium substrate. The EOTR takes place via the formation of a higher oxide [5-7]. These

anodes have high anodic stability and have widely replaced the classical graphite electrode in some processes. Discoveries concerning the deposition and the electrochemical properties of synthetic thin film of diamond have open a new branch of electrochemistry. Using doped synthetic diamond films at high potentials, it is possible to perform oxidation processes with a high current efficiency without any loss of activity, thus leading to partial oxidation or complete combustion of organic compounds. Boron-doped diamond anodes are called *non active* electrodes because the electrode surface does not participate directly in the reaction. On the contrary of DSA® anodes, the oxidation process at BDD is not assisted by the formation of an higher oxide but occurs via the electrogenerated hydroxyl radicals.

The principal aim of this work was to confirm the key role of hydroxyl radicals at BDD electrode by detecting them and understanding their reactivity.

In the theoretical part (Chapter 3), three models were developed. The first one deals with the concept of *active* and *non active* electrodes, illustrating either the formation of higher oxide or the mediation of hydroxyl radicals without participation of the electrode surface. Then, the *COD-ICE* model will describe the oxidation process in terms of chemical oxygen demand and instantaneous current efficiency evolutions allowing the prediction of the combustion of organics at BDD electrode. Finally, the last model will focus on the reaction between hydroxyl radicals and organic compounds in the reaction cage (region very close to the electrode).

The electrochemical properties of BDD electrode (Chapter 5) compared to glassy carbon, a more classic material electrode, was studied with the concept of *outer sphere* system (violuric acid). The investigation by classical electrochemical techniques such as cyclic voltammetry, low field approximation and rotating disk electrode, whose basic concepts are different (transitory, stationary or mixed control), allowed the characterization of the system by determining key parameters such as the diffusion coefficient, the standard reaction rate constant and the anodic coefficient transfer.

Because hydroxyl radicals play a preponderant role during EOTR process at BDD anode, their presence was investigated (Chapter 6). Because of the difficulty to study radicals by a direct method, spin trapping represents a good alternative. Two spin traps

(5,5-dimethyl-1-pyrroline-N-oxide, DMPO and *N*-tert-butyl-α-phenylnitrone, PBN) were used to test by electron spin resonance the presence of electrogenerated OH radicals. Another spin trap experiment was performed with *p*-nitroso-dimethyl-aniline using *UV* measurement. To further prove the presence of OH radicals, the hydroxylation of salicylic acid, as the formation of H_2O_2 at BDD electrode and the investigation of competitive reactions (competition between hydroxyl radicals and organic compounds) were also performed.

In Chapter 7, the predicting models were validated with the oxidation at BDD electrode of a pesticide, 4-chlorophenoxyacetic acid (4-CPA).

Then, salicylic acid was used as a model for oxidation at BDD electrode. In order to validate the models in a two-compartments electrochemical flow cell and to investigate the reactivity of hydroxyl radicals during the oxidation process, the hydroxylation of salicylic acid was investigated (Chapter 8). This organic compound is often used as reference compound in biology, and is known to undergo a selective hydroxylation leading to the formation of two main dihydroxylated intermediates, 2,3- and 2,5-dihydroxylated benzoic acids (DHBA). The comparison between the electrochemical hydroxylation at BDD electrode and the chemical one (by Fenton reaction and *UV*-H_2O_2) led us to a possible mechanism for hydroxyl radicals attack at BDD electrode.

Finally, a new type of electrochemical cell (turbine cell) was developed (Chapter 9). This turbine cell allowed us to establish good hydrodynamic conditions (very useful for electrolysis) and study the oxidation of salicylic acid.

1. REFERENCES

[1] W. Haenni, P. Rychen, M. Fryda, and C. Comninellis, *Industrial Applications of Diamond Electrodes*, in *Thin film Diamond II*, Elsevier, Editor. 2004, Academic Press.

[2] C. Comninellis and C. Pulgarin, *J. Appl. Electrochem.*, **21** (1991) 703.

[3] C. Lamy, *Electrochim. Acta*, **29** (11) (1984) 1581.

[4] J.-M. Léger, *J. Appl. Electrochem.*, **31** (2001) 767.

[5]   S. Ardizzone, A. Carugati, and S. Trasatti, *J. Electroanal. Chem.*, **126** (1981) 287.

[6]   G. Fóti, D. Gandini, and C. Comninellis, *Curr. Top. Electrochem.*, **5** (1997) 71.

[7]   R. Kötz, H. Neff, and S. Stucki, *J. Electrochem. Soc.*, **131** (1984) 72.

Chapter 2. Bibliography

1. INTRODUCTION

The electrochemistry of diamond is a relatively new branch, which is widely studied because of its numerous possible applications. This bibliography will give the state of art of this field and develop some crucial points. The first point concerns the synthesis of boron-doped diamond electrode, where parameters such as the crystallographic structure, the surface functional groups, the boron doping level and the carbon hybridation (sp^2 and sp^3) at the surface influence the electrochemical behavior of BDD electrodes.

This chapter will then recapitulate the principal electrochemical properties of synthetic diamond and applications such as the production of strong oxidants and waste water treatment. Some basic electrochemical theories such as the classification of the electrochemical reactions and the most used electrochemical characterization techniques (voltammetry, steady-state polarization, rotating disk electrode) will be reminded in order to understand the behavior of synthetic diamond films.

Finally, this chapter will greatly emphasize on hydroxyl radicals, their production, their reactivity, their role and their detection.

2. SYNTHESIS OF THIN-FILM DIAMOND BY HF-CVD

Diamond is known as the hardest substance [1]. It is a metastable form of carbon at ambient temperature and pressure. Among the four polymorphisms of carbon, diamond is the most compact and strongly bonded structure. The interest for diamond arises from its wide range of extreme properties such as high mechanical hardness, high value of thermal conductivity ($2 \cdot 10^{-3}$ W m^{-1} K^{-1} at room temperature), broad optical transparency, biologically compatibility and low electron affinity. Diamond is also a good electrical insulator but becomes a semiconductor when doped (band gap of 5.4 eV). Finally, it is very resistive to chemical corrosion [2]. Two historical discoveries mark the start of diamond research. In the first one, Lavoisier showed in 1772 that diamond and charcoal have the same composition. The second observation was that the density of diamond is higher than charcoal. In 1797, Tennant concluded that «diamond is made up of charcoal and just the crystalline form changes». Late, the phase diagram of carbon was established by G. N. Lewis and M. Randall. The first article about the diamond synthesis at high pressure was published by General Electrics in 1955 (Figure 2.1). Since the beginning of the fifties, the research in the domain of diamond synthesis made progress in optimizing parameters such as the substrate, the seeding and the doping level.
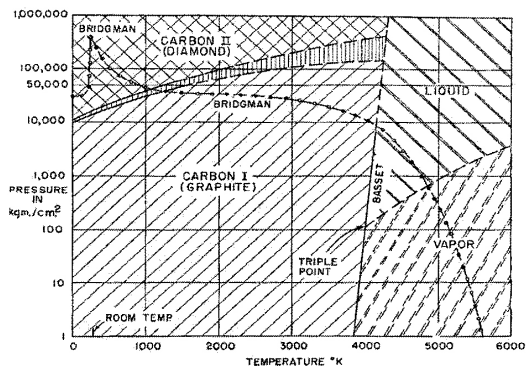
Figure 2.1 Phase diagram of carbon [3].

At the same period, researches were made to produce diamond in metastable conditions (Union Carbide). From then on, the importance of hydrogen was emphasized

and the synthesis was focused on the chemical vapor deposition of diamond (CVD). In 1974, Matsumoto *et al.* [4] adjusted the first depositions in vapor phase from a gas mixture of CH_4/H_2. The principle of the CVD method is to generate an important quantity of monoatomic hydrogen in a gas containing a low concentration of hydrocarbon. The diamond synthesis can be classified in accordance with the mode of gas activation:

- Thermic: hot filament, oxy-acetylene flame

- By plasma: DC arc, microwave

The boron-doped diamond electrodes used in this work are prepared by Hot Filament Chemical Vapor Deposition (HF-CVD) at the Swiss Center for Electronic and Microtechnology (CSEM). Therefore, only this method will be explained in detail. This method allows the deposition of diamond on a large surface and on tridimensional objects. The HF-CVD process has been improved considerably, with the substrate pretreatment, which increases the nucleation density and consequently yields to the formation of a continuous film. Diamond can also be deposited with increasing growth rates with methane concentrations in hydrogen and filament temperatures. The CVD technique is considered, compared to the other deposition types, as a «cheap» method that uses an inexpensive equipment. This deposition technique involves a gas-phase chemical reaction, which occurs above a solid surface. Basically, a large excess of hydrogen is mixed with a hydrocarbon precursor, typically methane. Then, the mixture is passed through a hot filament wire. The substrate temperature and the concentration of hydrogen atoms play an important role in the deposition of diamond.

2.1. Reactor

The reactor consists of a continuously pumped vacuum chamber (10-50 mbar) (Figure 2.2). In order to keep the substrate to the desired temperature (700-925 °C, measured by a thermocouple), the substrate is maintained at few millimeters below the filament, heated at 2200-2600°C (temperature measured by an optical pyrometer). The gas phase consists in a mixture of methane (0.5-2.5%) in hydrogen.

The principle of the HF-CVD technique is the thermal activation of the gas phase. The role of the filament is to produce gaseous species and its choice must fulfill some conditions. First, the melting point of the filament material has to be high (in order to provide the melting with carbon). From this point of view, tungsten and tantalum are commonly used. Moreover, compared to other suitable materials, its cost is relatively low.

The use of multifilament arrays allows to improve a large-area deposition.

The reactivity of the filament metal toward carbon is also important because the carburisation of the filament is a consequence of gaseous species activation and modifies the physical properties of the filament material. Nevertheless, the role of the filament material is not very clear. It can be concluded that the filament plays the role of either energy supplier or catalyst in the dissociation of H_2.
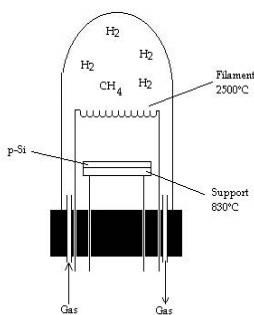
Figure 2.2 Scheme of the reactor for HF-CVD technique.

2.2. Substrate

The substrate is also an important parameter for the preparation of the electrode. Its preparation determine the porosity, the adhesion and the quality of the diamond layer.

The substrate must fulfill some conditions such as chemical, electrochemical and mechanical stability under the strong conditions of deposition, a low thermal expansion coefficient and a good electrical and thermal conductivity. Moreover, the substrate must be able to form a diffusion barrier (to avoid the hydrogen embrittlement) and a conductive layer at the substrate/diamond interface. At the interface, a good chemical bonding has to be created (covalent σ bonding) to give a good adhesion and ohmic contact. Actually, the real interface between the diamond and the substrate is the carbide layer, which is produced at the beginning of the synthesis. The candidate substrates can be classified in two categories:

- Metallic substrates: Ti, W, Zr, Nb, Ta and some of their alloys
- Ceramic conductive substrates: carbon allotropes, silicon, mosaic shape supports

The advantages of metallic substrates are, on the one hand, the low cost, the low thermal expansion and the large choice of forms (plates, disks, grids, rods...). On the other hand, the main problem of the metallic substrates is their tendency to undergo hydrogen embrittlement, especially titanium. The choice of the substrate also depends on the electrochemical application (as anode, cathode or bipolar electrode). Silicon remains the only anodic substrate for diamond electrodes. In our work, diamond electrodes were deposited on p-Si substrate.

2.3. Nucleation and diamond growth

The main question is how diamond is able to grow on non-diamond substrate. The carbon atoms have to nucleate onto the substrate surface to allow the initiation and the construction of a tetrahedrally coordinated sp^3 network. The nucleation seems to start on substrate surface defects. Therefore, it is necessary to pretreat the surface by abrasion, by mechanical polishing with a diamond powder or by ultrasonication in diamond powder suspensions. The nucleation can only start on saturated carbon surface. The precursor gases (usually hydrogen and methane) are dissociated by thermal energy from the hot filament, resulting in the formation and the diffusion of the reactive species (mainly methyl radical) toward the substrate surface. Then, a carbon film is formed by absorption and coalescence (Figure 2.3).
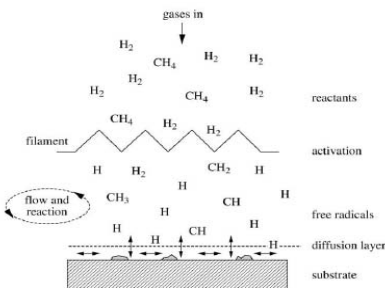
Figure 2.3 Growth processes during diamond deposition by CVD [2].
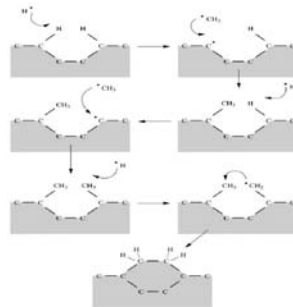
Figure 2.4 Mechanism of diamond growth [2].

The pathway for the growth of diamond is not well understood. One suggests that atomic hydrogen abstracts a hydrogen atom from the surface of diamond, leaving a

surface radical. Then, a methyl radical adds to the «dangling bond». These two steps are repeated until the formation of the lattice is completed (Figure 2.4). At the end, the surface is formed mainly by a tertiary carbon atom with just a single C-H bond [5, 6].

2.4. Doping of diamond

Intrinsically, diamond is an insulator. To make it conductor, it is necessary to dope it with boron, fluorine or nitrogen. With increased concentration of the doping, the insulator behavior of diamond changes into semi-conductor and finally into metallic behavior. For electrochemistry, the doping level has to be sufficient to generate a low ohmic drop within the diamond layer (quasi-metallic conduction) and sufficiently low not to disturb the crystalline structure and induce a graphitic phase during the synthesis. Two types of doping are possible: positive and negative. The positive doping consists of substituting some carbons by an atom having a similar size, a slightly higher energy level than the valence band of diamond, and where an electron is missing in the electronic layer compared to diamond (*e.g* boron). On the contrary, in the case of a negative doping, the atom will have an extra electron and a slightly lower energy level (*e.g* nitrogen). The diamond electrodes used in this work were doped with boron. Therefore, only this type of doping will be studied in detail. Energetically, the boron dopant atoms, which are electron acceptors, form a band located at about 0.35 eV above the valence band edge. At room temperature, some of the valence band electrons are thermally promoted to the boron acceptors, leaving free electrons in the dopant band and holes or vacancies, in the valence band to support the flow of current [7]. The morphology of boron-doped diamond is polycrystalline and rough with grain boundaries and small volume of non-diamond carbon impurities leading to the change of the electrical conductivity with the doping level. The electrical resistivity of BDD films also depends on the doping level in the diamond coating (Figure 2.5).

Typical boron concentrations range from 500 to 8000 ppm. For electrochemical applications, lower concentrations result in an excessive electrical resistivity and higher levels lead to the anodic consumption of the electrode, probably because of a secondary nucleation of diamond and the formation of sp^2 carbon species.
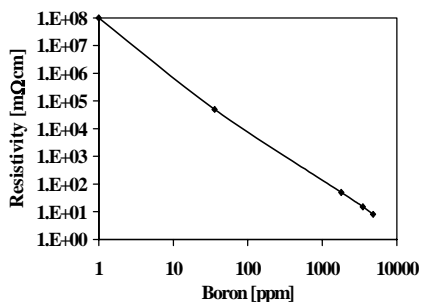
Figure 2.5 Resistivity of diamond films as function of the boron level in the diamond coating.

The synthesis of diamond by HF-CVD produces a columnar, randomly textured, polycrystalline film on a conductive substrate (Figure 2.6). A typical Raman spectrum is presented in Figure 2.7. The first broad peak (A) is attributed to the boron doping, the well defined peak B at 1330 cm^{-1} corresponds to diamond (sp^3 species), and the peak C, at about 1560 cm^{-1}, is assigned to the sp^2 impurities. When comparing the peak intensities of both sp^3 (diamond) and sp^2 (non diamond) carbon, it is necessary to consider that the magnitude of the Raman signal is 50 times more sensitive toward the non diamond carbon form than to the diamond one [8].
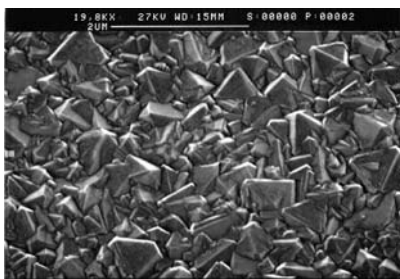
Figure 2.6 SEM image of a polycrystalline boron-doped diamond (as-grown).
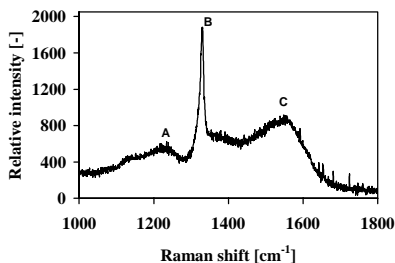
Figure 2.7 Raman spectrum of as-grown diamond electrode (0.5 ppm of boron in the gas phase).

3. ELECTROCHEMICAL PROPERTIES AND APPLICATIONS OF SYNTHETIC DIAMOND FILMS

3.1. Properties

Thin diamond films exhibit properties that are interesting for electrochemistry. These properties are currently investigated in many laboratories and many electrochemical applications are studied. The first studies were started fifteen years ago [9-11]. The behavior was then investigated extensively by different electrochemical techniques such as impedance [8, 12-14], cyclic voltammetry [15, 16] or steady state polarization [17, 18].

Compared to graphite or glassy carbon electrodes, the inertness of diamond yields to a very good resistance toward corrosive conditions, which is very useful in electrochemistry (molten salts, batteries, fuel cells). The electrochemical characterization of BDD electrodes is generally confirmed by surface analysis methods such as ESCA, Raman spectroscopy, diffraction or microscopy.

Diamond thin films exhibit a very large potential window with respect to hydrogen and oxygen evolution (Figure 2.8). It is established that a good quality film exhibits a window of about 4 V and a low voltammetric background current.
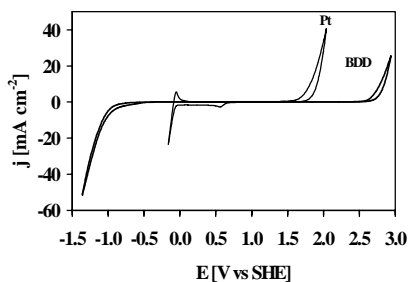
Figure 2.8 Cyclic voltammogram for BDD and platinum electrodes.

The low background current (and the low capacitance) was investigated by Xu *et al.* [7]. They proposed three factors; the first is the relative absence of electroactive carbon-oxygen functionalities on the hydrogen-terminated diamond electrode surface. The second parameter is the lower density of surface electronic states near the Fermi level

caused by the semi-conductor nature of BDD. Finally, the structure of diamond, which can be schematized as a series of microelectrodes, could explain the low background current. Indeed, one can assume that the diamond surface has electrochemically active sites separated by more insulating regions.

The wide potential window of diamond allows the study of electrochemical reactions that occur at high overpotentials. The redox couple $(Fe[CN]_6^{3-} / Fe[CN]_6^{4-})$, ferri-ferrocyanide, classified as an *outer sphere* system, was largely studied at BDD electrode. This redox system can also be used to determine the properties of the electrode material, and it has been shown that the presence of sp^2 impurities (non diamond) can have a strong influence on the electrochemical response of the electrode [19].

3.2. Applications

The properties of BDD such as high anodic stability in strongly acidic medium, high oxygen evolution overpotential and formation of hydroxyl radicals during water discharge allow to produce powerful oxidants with high redox potential for waste water treatment and electroorganic synthesis via EOTR.

Electroorganic synthesis

The feasibility of electroorganic synthesis was investigated in our laboratory with different organic compounds. The oxidation of 3-methylpyridine (3-MP) to nicotinic acid is a typical example [20, 21]. Bulk electrolysis of 3-MP in 0.5 M $HClO_4$ in a one-compartment DiaCell® cell at low current density (2.5 mA cm^{-2}) and for low 3-MP conversion have shown that partial oxidation of 3-MP to nicotinic acid can be achieved at BDD electrode.

In case of partial oxidation, experimental results have shown that the *TOC* (total organic carbon) of the electrolyte remains almost constant during electrolysis while the concentration of 3-MP decreases. Hydroxyl radicals formed by water discharge on BDD anode certainly participate in the oxidation of 3-MP to nicotinic acid as shown at Figure 2.9:
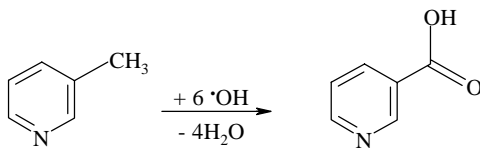
Figure 2.9 Scheme of 3-methylpyridine oxidation.

Furthermore there is no indication of electrode deactivation during 3-MP oxidation under these experimental conditions.

Preparation of powerful oxidants

The production of oxidants can be performed either by a fast and direct reaction involving one electron transfer or by an indirect mechanism assisted by electrogenerated intermediates (hydroxyl radicals). The first type of reaction can lead to the formation of powerful oxidants. Redox couples like Ag(II)/Ag(I), Ce(IV)/Ce(III) or Co(III)/Co(II) were used with a high current efficiency that is not observed with other electrodes such as Pt, Au or Sb-SnO$_2$. The oxidation of Ag(I) to Ag(II) at BDD anode was studied in our laboratory [22]. The electrogeneration of Ag(II) was performed in concentrated nitric acid and the formation of an anodic peak, whose intensity was proportional to concentration of Ag(I), was observed by cyclic voltammetry. Besides the high current efficiency, the high anodic stability of BDD in acidic medium represents an important advantage compared to Pt or Au electrodes.

The indirect process can be illustrated by the formation of peroxodisulfate, the strongest oxidizing agent known. The oxidation requires a high overpotential in order to minimize the reaction of oxygen evolution. Since the production of peroxodisulfate is usually performed at platinum anodes, this process encounters some problems because of the high corrosion rate, the cleaning of the corrosion products and additives (thiocyanates) on Pt surface. The reaction has been investigated in our laboratory [23]. The optimal conditions of temperature and sulfuric acid concentration were determined and the production of peroxodisulfate was performed with a high current efficiency. This reaction is assumed to be indirect, assisted by hydroxyl radicals (Equation 2.1):

$$2HSO_4^- + 2HO^\bullet \rightarrow S_2O_8^{2-} + 2H_2O \qquad\qquad 2.1$$
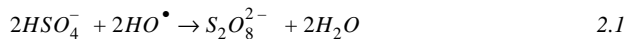
Waste water treatment

Although the biological treatment is the most economic process for waste water treatment, it is not applicable to refractory organic pollutants, and electrochemical oxidation becomes a very attractive alternative. The oxidation of some model organic pollutants has been investigated at boron-doped diamond electrode in our laboratory. The organic compounds can be classified in two main classes: simple carboxylic acids and phenolic compounds. The oxidation of carboxylic acids was performed in the region of water stability. No electrochemical activity was observed and the only difference caused by the presence of organics was a decrease in the starting potential of water discharge. This phenomenon can be explained by the presence and the mediation of electrogenerated hydroxyl radicals, confirming the indirect mechanism [24].

Concerning the oxidation of phenolic compounds in the region of water decomposition, the behavior was different. An anodic peak that corresponds to the formation of phenoxy radical was observed [25] but the polymerization resulted in the formation of a polymeric film and in the deactivation of the surface. Only an anodic polarization at high potential has permitted the reactivation of the diamond surface.

In summary, electrochemical oxidation of organics at BDD electrode in the region of water discharge has been performed with a large number of compounds (carboxylic acids, alcohols, ketones, phenolic compounds, aromatic acids and soluble polymer). All the oxidations can be achieved with high current efficiency.

4. CLASSIFICATION OF ELECTROCHEMICAL REACTIONS

A general electrochemical process can be summarized in five steps (Figure 2.10). Firstly, the mass transfer from the bulk solution to the electrode surface takes place. Then, homogeneous or heterogeneous chemical reactions occur in the electrode surface region associated to surface phenomena (adsorption, crystallization). These reactions are followed by the electronic transfer at the electrode surface. Finally, the mass transfer from the electrode surface to the bulk solution occurs.
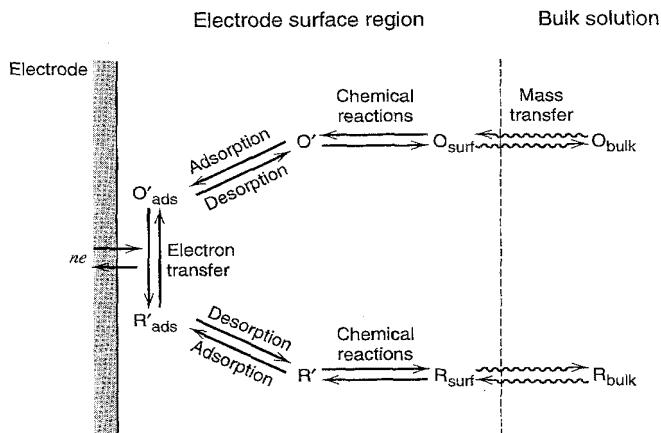
Figure 2.10 Pathway of a general electrode reaction [26].

The electron transfer reaction is influenced by the nature and the structure of the reacting species, the potential, the solvent, the electrode material and the adsorbed layers on the electrode. In order to understand these influences (interactions between reactant and electrode surface), microscopic theories have been developed based on two main concepts, which are known as *inner sphere* and *outer sphere* electron transfer reactions.

4.1. *Outer sphere* electron transfer reaction

The term *outer sphere* is used to describe a reaction, in which the activated complex maintains the coordination sphere originally present in the reactant species (Figure 2.11). During o*uter sphere* reactions, weak interactions between the electrode and the reactant take place. The interaction maintains a distance of at least one solvent layer between the reactant and the electrode surface. In this case, the kinetics of the reaction is not much dependent on the electrode material.

Nevertheless, the electrode material could influence the kinetics, even in the case of *outer sphere* charge transfer, by affecting the electrical double layer and the Helmotz layer structure. Since *outer sphere* reactions can be treated in a more general way than *inner sphere* processes, for which specific chemistry and interactions are important, the theory of *outer sphere* electron transfer is much more developed. Among the large *outer*

sphere systems, $Fe(CN)_6^{3-}/Fe(CN)_6^{4-}$ and $IrCl_6^{2-}/IrCl_6^{3-}$ reactions are the most frequently used.
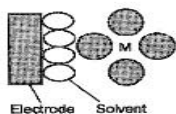
Figure 2.11 Outer sphere reaction. M represents the metal ion surrounded by ligands.
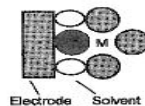
Figure 2.12 Inner sphere reaction. M represents the metal ion surrounded by ligands.

4.2. *Inner sphere* electron transfer reaction

A reaction is described in terms of *inner sphere* when the reactants share a ligand in the activated complex (Figure 2.12). Therefore, both the reactant and the product species, as well as the activated complex, are involved in very strong interactions with the electrode surface (specific adsorption). This kind of reaction implies multistep electron-transfer reactions [27]. Benzoquinone/hydroquinone reaction is known as a typical *inner sphere* reaction that involves complex electron and proton transfer mechanisms.

5. ELECTROCHEMICAL CHARACTERIZATION TECHNIQUES

The electrochemical behavior of a given electrode material as well as of a redox system can be studied by different electrochemical techniques.

5.1. Linear sweep voltammetry and cyclic voltammetry

The voltammetry techniques, including linear sweep voltammetry (LSV) and cyclic voltammetry (CV), are often used in electrochemistry [26]. The principle of these methods is the linear variation of the potential with time. In LSV, the potential is swept from an initial value E_i (Equation 2.2).

$$E(t) = E_i - vt \qquad\qquad 2.2$$

Cyclic voltammetry is known as a reversal technique, where the potential sweep

occurs between the limits E_i and E_λ (Equation and Equation 2.4).

$$\text{for the reduction sweep } E(t) \; = \; E_i{-}vt \qquad\qquad 2.3$$

$$\text{for the oxidation sweep } E(t) \; = \; E_\lambda + vt \qquad\qquad 2.4$$

where E_i and E_λ are the limits of potential (V), v the scan rate (V s^{-1}) and t the time (s).

   Three cases have to be considered. The first one concerns reversible or Nernstian systems, where the rate of electron transfer is high at the electrode surface so that the species immediately adjust to the ratio predicted by the Nernst equation. The second case is known as the irreversible systems, for which the rate of electron transfer is slow. However, an alternative system exists, where the control is made simultaneously by the electron transfer and the diffusion rate. This system is called quasi-irreversible, or mixed.

Reversible systems (Nernstian systems) [26]

   We consider the reaction $O + ne^- \rightarrow R$ and assume a semi-linear diffusion. The solution contains only species O and the electrode is initially at a potential of E_i, where no reaction takes place.

   At the electrode surface, the rate of electron transfer is rapid. Therefore, the concentrations of the species O and R are dependent on the time. From the resolution of the Fick's law and the Randles-Sevcik equation, the *peak current, i_p* can be obtained, and defined, at 25°C, as:

$$i_p \; = \; (2.69 \times 10^5)n^{3/2}AD_O^{1/2}C_O^{*}v^{1/2} \qquad\qquad 2.5$$

where i_p is the peak current (A), n the number of exchanged electrons, A the electrode surface (cm^2), D_O the diffusion coefficient (cm^2 s^{-1}), C_O^{*} the bulk concentration (mol cm^{-3}) and v the scan rate (V s^{-1}).

   The *peak potential*, E_p, is defined at 25°C as:

$$E_p \; = \; E_{1/2} - 1.109\frac{RT}{nF} \; = \; \frac{28.5}{n} \text{ mV} \qquad\qquad 2.6$$

where E_p is the peak potential (mV), n the number of electron exchanged, F the Faraday's

constant (96485 C mol^{-1}), R the gas constant (8.314 J mol^{-1} K^{-1}) and T the temperature (298.15 K).

Sometimes, the peak is difficult to well define and it is easier to consider the *half-peak potential* $E_{p/2}$ that is the potential corresponding to the half peak current, $i_{p/2}$.

$$E_{p/2} = E_{1/2} + 1.09\frac{RT}{nF} = E_{1/2} + \frac{28}{n} \text{ mV} \qquad 2.7$$

$E_{1/2}$ is located just about midway between E_p and $E_{p/2}$, and that a convenient diagnostic for Nernstian wave is:

$$\left| E_P - E_{P/2} \right| = 2.2\frac{RT}{nF} = \frac{56.5}{n} \text{ mV} \qquad 2.8$$

E_p is independent of the scan rate and i_p is proportional to $v^{1/2}$. All equations are valid for linear sweep voltammetry. Two parameters are important in cyclic voltammetry and give a lot of information about the system. These are the ratio of the peak currents (i_{pa}/i_{pc}) and the separation of the peak potentials ($E_{pa} - E_{pc}$). In case of a Nernstian behavior, the ratio i_{pa}/i_{pc} is equal to 1 and $E_{pa} - E_{pc}$ is always close to 59/n mV at 25°C.

Irreversible systems [26]

Considering the reaction $O + ne^- \rightarrow R$ for a one-step reaction, the *peak current*, i_p, is given by the following equation:

$$i_p = (2.99 \times 10^5)n\alpha^{1/2}AC_O^* D_O^{1/2} v^{1/2} \qquad 2.9$$

where α is the transfer coefficient and the other units are similar to that of Equation 2.5.

For the irreversible system, the *peak potential*, E_p, is defined as:

$$E_p = E^{0'} - \frac{RT}{\alpha F}\left[0.78 + \ln\left(\frac{D_O^{1/2}}{k^0}\right) + \ln\left(\frac{\alpha F v}{RT}\right)^{1/2} \right] \qquad 2.10$$

where E^0 is the apparent potential (V) and k^0 is the standard electrochemical rate constant (cm s^{-1}).

As shown in the reversible system, it is sometimes easier to consider the *half peak potential* $E_{p/2}$, the following relation is obtained:

$$\left| E_p - E_{p/2} \right| = 1.857 \frac{RT}{\alpha F} = \frac{47.7}{\alpha} \text{ mV at } 25°C \qquad\qquad 2.11$$

Quasi-irreversible system [26]

In this system, one can consider that the separation between the peak potential increases with the scan rate and is higher than 59/n mV. The peak current is no proportional to $v^{1/2}$ anymore. The shape of the peak and its parameters are function of the parameter Λ [26].

$$\Lambda = \frac{k^0}{\left[(D_O^{1-\alpha})(D_R^{\alpha}) \frac{nF}{RT} v \right]^{1/2}} \qquad\qquad 2.12$$

If the diffusion coefficients are equal, Equation 2.12 becomes:

$$\Lambda = \frac{k^0}{\left[(D_O) \frac{nF}{RT} v \right]^{1/2}} \qquad\qquad 2.13$$

The wave shape is function of k^0, v and E_λ. If E_λ is at least 90/n mV beyond the cathodic peak, the effect of E_λ is small, the shape wave depends on the parameter Ψ:

$$\Psi = \frac{(D_O/D_R)^{\alpha/2} k^0}{\left(\pi D_O \frac{nF}{RT} v \right)^{1/2}} \qquad\qquad 2.14$$

Considering that $(D_O/D_R)^{1/2} = \gamma$ and $a = \frac{nF}{RT} v$, Equation 2.14 becomes the Nicholson-Shain equation:

$$\Psi = \frac{\gamma^{\alpha} k^0}{(\pi a D_O)^{1/2}} \qquad\qquad 2.15$$

When $0.3 < \alpha < 0.7$, the separation of peak potential E_p is independent of α and depends only on Ψ. Nicholson and Shain [28] have calculated this dependence, whose results are summarized in the Table 2.1.

Ψ	ΔE_p
20	61
7	63
6	64
5	65
4	65
3	68
2	72
1	84
0.75	92
0.5	105
0.35	121
0.25	141
0.1	212

Table 2.1 Values of E_p as a function of Ψ. T = 25°C, α = 0.5, n = 1.

5.2. Steady-state polarization [26]

This technique consists to apply a potential difference between the reference electrode and the working electrode. The current response is recorded when the steady state is reached.

The kinetics of the process is strongly affected by the potential of the electrode. The relation between the reaction rate and the applied potential is expressed by the terms of standard rate constant k^0, the exchange current i_0 and the transfer coefficient α. The one-step process can be written as:

$$O + ne^- \underset{k_a}{\overset{k_c}{\rightleftarrows}} R \qquad\qquad 2.16$$
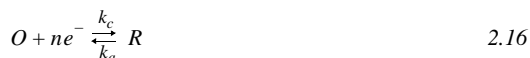
where k_c and k_a represent the heterogeneous rate constants of the reduction and oxidation reactions, respectively, and n is the number of exchanged electrons. When the rates are equal, the system is at equilibrium. The total current density j is composed of both

cathodic j_c and anodic j_a part:

$$-j_c = nFk_c C_O^s \qquad\qquad 2.17$$

$$j_a = nFk_a C_R^s \qquad\qquad 2.18$$

where C_O^s and C_R^s are the concentrations (mol m^{-3}) of the oxidized and the reduced forms at the electrode surface at time t, respectively and F the Faraday's constant (A s mol^{-1}).

The total current density j is the sum of the two components:

$$j = j_a + (-j_c) = nF[k_a C_R^s - k_c C_O^s] \qquad\qquad 2.19$$

A reaction can be represented in terms of progress along a reaction coordinate as shown in Figure 2.13.
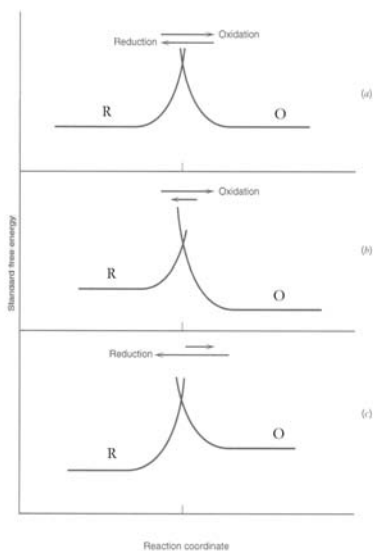
Figure 2.13 Simple representation of standard free energy changes during a faradaic process. (a) At a potential corresponding to the equilibrium, (b) At a potential higher than the equilibrium value, (c) at a potential lower than the equilibrium value. O/R = redox couple [26].

The configurations of the reactant and the product intersect at the transition state

(where the electron transfer occurs). The relative rates are represented by the height of the energy barriers. When the oxidation rate is equal to the reduction rate (Figure 2.13a), the potential is equal to E_{eq} and the system is at equilibrium. If the potential becomes more positive (Figure 2.13b), the energy of the reactant electron is lower. Therefore, the curve corresponding to O drops and the oxidation reaction is favored. On the contrary, at lower potential (Figure 2.13c), the oxidation barrier is raised and the reduction reaction is favored.

The influence of the potential on the rate of an electrode process is described by the following equations:

$$k_c = k_c^0 \exp\left[-(1-\alpha)\frac{nF}{RT}\right]E \qquad\qquad 2.20$$

$$k_a = k_a^0 \exp\left[\alpha\frac{nF}{RT}\right]E \qquad\qquad 2.21$$

where E is the potential (V) and $0 < \alpha < 1$.

Combining the two previous equations with Equation 2.19, we obtain:

$$j = nF\left[k_a^0 C_R^s \exp\left(\alpha\frac{nF}{RT}\right)E - k_c^0 C_O^s \exp\left(-(1-\alpha)\frac{nF}{RT}\right)E\right] \qquad\qquad 2.22$$

At the standard redox potential E^0, the reduction and oxidation rate constants k_c and k_a have the same value, equal to the standard rate constant k^0, which is defined by:

$$k^0 = k_a^0 \exp\left[\alpha\frac{nF}{RT}E^0\right] = k_c^0 \exp\left[-(1-\alpha)\frac{nF}{RT}E^0\right] \qquad\qquad 2.23$$

A large value of k^0 (in the range of 10^{-2} to 10^{-1} m s^{-1}) describes a system that can reach the equilibrium quickly, which is typical of *outer sphere* reactions. On the contrary, a small value means a very slow process.

Combination of Equation 2.22 and Equation 2.23 yields to:

$$j = nFk^0\left[C_R^s \exp\left(\alpha\frac{nF}{RT}(E-E^0)\right) - C_O^s \exp\left(-(1-\alpha)\frac{nF}{RT}(E-E^0)\right)\right] \qquad\qquad 2.24$$

From the definition of the overpotential (Equation 2.24):

$$\eta = E - E_{eq} \qquad\qquad 2.25$$

and the *Nernst* equation (Equation 2.26):

$$E_{eq} = E^0 + \frac{RT}{nF}\ln\frac{C_O^*}{C_R^*} \qquad\qquad 2.26$$

when $C_O^* = C_R^*$, j can be written as (Equation 2.27):

$$j = nFk^0\left[C_R^s\exp\left(\alpha\frac{nF}{RT}\eta\right) - C_O^s\exp\left(-(1-\alpha)\frac{nF}{RT}\eta\right)\right] \qquad\qquad 2.27$$

From Equation 2.24, Equation 2.25 and Equation 2.26, we obtain

$$j = j_0\left[\frac{C_R^s}{C_R^*}\exp\left(\alpha\frac{nF}{RT}\eta\right) - \frac{C_O^s}{C_O^*}\exp\left(-(1-\alpha)\frac{nF}{RT}\eta\right)\right] \qquad\qquad 2.28$$

where j_0 is the exchange current density, defined by:

$$j_0 = nFk^0[C_O^*]^{1-\alpha}[C_R^*]^{\alpha} \qquad\qquad 2.29$$

When $C_O^* = C_R^* = C^*$,

$$j_0 = nFk^0C^* \qquad\qquad 2.30$$

If the solution is well stirred or the current very low, the surface concentration is almost the same than the bulk value. Therefore, Equation 2.28 becomes the *Butler-Volmer* equation:

$$j = j_0\left[\exp\left(\alpha\frac{nF}{RT}\eta\right) - \exp\left(-(1-\alpha)\frac{nF}{RT}\eta\right)\right] \qquad\qquad 2.31$$
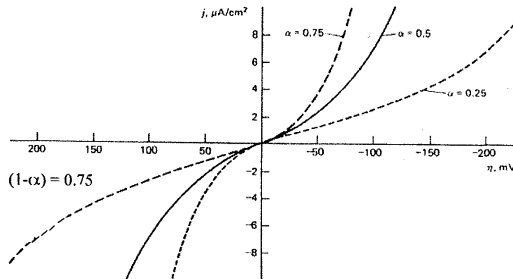
Figure 2.14 Representation of the Butler Volmer equation as a function of α.

Two different limit cases can be distinguished:

Low overpotential ($\eta < 10\ mV$)

In this case, $\frac{nF}{RT}\eta < 1$ and the Butler-Volmer equation can be simplified:

$$j = j_0 \frac{nF}{RT}\eta \qquad\qquad 2.32$$

The graphical representation of j as a function of overpotential allows to define the the exchange current j_0 (Figure 2.15).

The charge transfer resistance R_{ct}, is equal to the ratio η/j and can be written as:

$$R_{ct} = \frac{RT}{nFj_0} \qquad\qquad 2.33$$
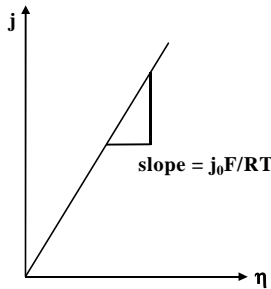
Figure 2.15 j-η relation for low overpotential, n = 1.

Large overpotential ($\eta > 120\ mV$)

This represents an important limiting case of the Butler-Volmer equation. In this case, high potentials are encountered, the reaction becomes irreversible, and one of the exponential term becomes negligible.

For a high anodic overpotential:

$$j = j_0 \exp\left(\alpha \frac{nF}{RT}\eta_a\right) \qquad\qquad 2.34$$

and

$$\eta_a = \frac{RT}{nF}\ln j - \frac{RT}{nF}\ln j_0 \qquad\qquad 2.35$$

The i-η relation is called *Tafel relation* and is useful to determine kinetic parameters. Two branches are defined corresponding to both anodic and cathodic slopes.

The slope of the Tafel line gives the transfer coefficient α and the intercept determines the exchange current density j_0 (Figure 2.16).
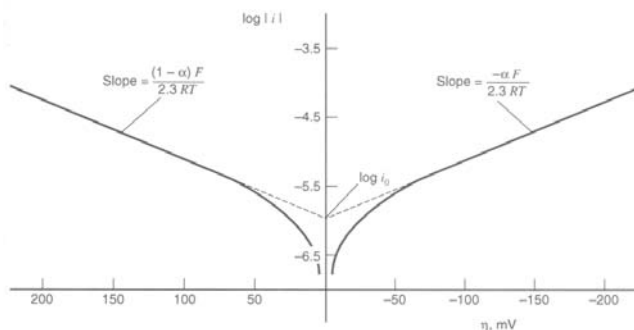
Figure 2.16 Tafel plot for anodic and cathodic parts of the current-overpotential curve. $\alpha = 0.5$, T = 25°C, $j_0 = 10^{-6}$ A cm^{-2}.

5.3. Rotating disk electrode [26]

The term of hydrodynamic method concerns the methods involving convective mass transport of reactants and products. The main advantage is that a steady state is quickly reached, resulting in a high precision of the measurements. The method to obtain well-defined diffusion conditions was developed by Levich, who first introduced and described the rotating-disk electrode (RDE). A further development by Frumkin and Levich is the rotating ring disk electrode (RRDE).

The rotating disk electrode (RDE) consists of a disk of the electrode material embedded in a rod of insulating material, typically made of Teflon, epoxy resin or another plastic. The rod is attached to a motor directly by a chuck or by a flexible rotating shaft and rotates at a certain angular velocity ω (s^{-1}), where $\omega = 2\pi f$ (f is the frequency in rad s^{-1}). The electrical connection is made by a brush contact. The motion of the electroactive species is due to the rotation of the electrode (Figure 2.17 and Figure 2.18).
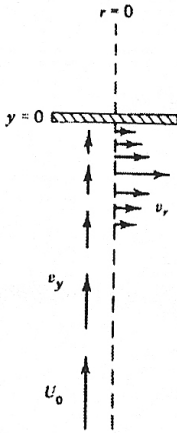
Figure 2.17 Vector representation of fluid velocities near a RDE.
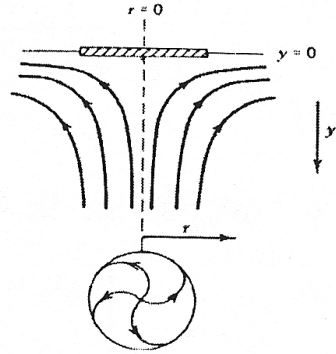
Figure 2.18 Schematic resultant streamlines.

From the solution of the convective-diffusion equation, the steady-state limiting current density can be written as:

$$j_{lim} = 0.62 n F D_O^{2/3} \omega^{1/2} v^{-1/6} C_O^*$$

<div align="right">*2.36*</div>

where j_{lim} is the limiting current density (A cm^{-2}), n the number of exchanged electrons, D the diffusion coefficient (cm^2 s^{-1}), ω the angular velocity (s^{-1}), v the scan rate (V s^{-1}) and C_O^* the bulk concentration (mol cm^{-3}).

This equation is called the Levich relation. From the Nernst diffusion layer model and the first Fick's law, one can define δ, the distance from the electrode at which the convection maintains the concentrations of all species uniform and equal to the bulk values (Equation 2.37). Below this value, no solution movement takes place and the mass transfer occurs by diffusion.

$$\delta = 1.61 D_O^{1/3} \omega^{-1/2} v^{1/6}$$

<div align="right">*2.37*</div>

Considering a nernstian reaction and coupling the Nernst equation with the equation for a voltammetric wave, one obtains:

$$E = E_{1/2} + \frac{RT}{nF}\ln\frac{(i_{lim,\,c} - i)}{(i - i_{lim,\,a})} \qquad \qquad 2.38$$

where

$$E_{1/2} = E^{0\prime} + \frac{RT}{nF}\ln\left(\frac{D_R}{D_O}\right)^{2/3} \qquad \qquad 2.39$$

For a irreversible one-step reaction, the current is:

$$i = nFAk^0\exp\left[-\alpha\frac{F}{RT}(E - E^{0\prime})\right]C_O^s \qquad \qquad 2.40$$

From the Fick's law, one obtains:

$$i = nFAk^0\exp\left[-\alpha\frac{F}{RT}(E - E^{0\prime})\right]C_O^*\left(1 - \frac{i}{i_{lim,\,c}}\right) \qquad \qquad 2.41$$

Defining i_K as the current in absence of any mass-transfer effects (when the concentration at the electrode surface is equal to the one in the bulk):

$$i_K = nFAk^0\exp\left[-\alpha\frac{F}{RT}(E - E^{0\prime})\right]C_O^* \qquad \qquad 2.42$$

one obtains the *Koutecky-Levich* equation:

$$\frac{1}{i} = \frac{1}{i_K} + \frac{1}{i_{lim,\,c}} = \frac{1}{i_K} + \frac{1}{0.62nFAD_O^{2/3}\omega^{1/2}v^{-1/6}C_O^*} \qquad \qquad 2.43$$

6. HYDROXYL RADICALS

In biology and medicine, free radicals are now of intense interest because they are involved in many different aspects of metabolism, ranging from oxygen consumption to xenobiotic metabolism. Basically, free radicals are molecules containing an odd electron that is associated with the molecular system. Hydroxyl radicals are known to be highly reactive, chemically aggressive and, therefore, short-lived species.

In a first place, we will list several pathways that lead to the formation of hydroxyl radicals. Then, the methods of hydroxyl radicals detection will be explained.

6.1. Production of hydroxyl radicals

6.1.1. Electrochemical production and reactivity

The electrochemical production of hydroxyl radicals and their role in electrochemical oxygen transfer reactions depend on the electrode material used. The mechanism of hydroxyl radicals formation depends also on the potential. These radicals are then more or less strongly adsorbed at the surface. The aim of this part is to recapitulate the behavior of platinum and boron-doped diamond electrodes toward OH radicals.

The mechanism of the water activation reaction implies to deal with two different mechanisms depending on the potential; via either the dissociative adsorption of water or the electrochemical water discharge.

Formation of OH radicals via the dissociative adsorption of water

Platinum is a typical electrocatalytic material. This type of material implies the formation and the breaking of bonds between species and adsorption sites. On this electrode material, the electrochemical oxygen transfer reaction occurs as follow (Equation 2.44):

$$RH + H_2O \rightarrow RO + 3H^+ + 3e^-$$ *2.44*
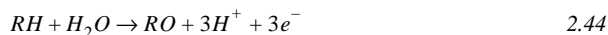
At a potential lower than the thermodynamic one for water discharge to O_2, the water activation is described by the Equation 2.45, followed by Equation 2.46. These reactions take place at a low potential (about 0.4 V vs *SHE)* and lead to the strong adsorption of hydroxyl radicals on the platinum surface.

- dissociative adsorption of water:

$$(H_2O)_{ads} \rightarrow (H^\bullet)_{ads} + (HO^\bullet)_{ads}$$ *2.45*

- hydrogen discharge:

$$(H^\bullet)_{ads} \rightarrow H^+ + e^-$$ *2.46*
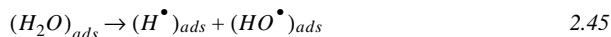
Once the hydroxyl radicals are produced, the reaction with an organic compound RH can occur via two possible mechanisms: Eley-Rideal (Equation 2.47) or Langmuir-

Hinshelwood (Equation 2.48):

$$RH + (HO^{\bullet})_{ads} \rightarrow RO + 2H^+ + 2e^- \qquad\qquad 2.47$$

$$(RH)_{ads} + (HO^{\bullet})_{ads} \rightarrow RO + 2H^+ + 2e^- \qquad\qquad 2.48$$

In the first mechanism (Eley-Rideal), only hydroxyl radicals are strongly adsorbed, while for Langmuir-Hinshelwood, both hydroxyl radicals and organic compounds are strongly adsorbed at the electrode surface. The adsorption of the organic compound is performed by the first step of the *inner sphere* electron transfer anodic reaction (RH $\rightarrow$(RH)$_{ads}$).

As example, we will illustrate the mechanistic aspects of methanol oxidation on platinum-based electrode with the study of different steps (adsorption steps and involved intermediates). This mechanism is not well known but is fully investigated because of the importance of methanol in fuel cells applications. The determination of the electrocatalytic reaction steps requires information not only on the activity of the electrode, but also on the nature of the different species involved, including adsorbed species, intermediates and final products.
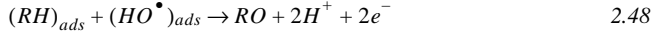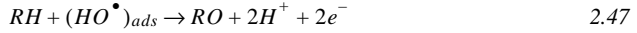
From a thermodynamic point of view, methanol can be oxidized at a very low potential (0.046 V vs *SHE*). However, it is well known that methanol can only be oxidized at potentials greater than 0.5 V, in acidic medium on a platinum electrode. This behavior can be explained by the slow electrooxidation kinetics, which leads to high overpotentials.

The first step of the reaction is the adsorption of methanol, immediately followed by its dissociation into several adsorbed species [29].

$$Pt + (CH_3OH)_{sol} \rightarrow Pt - (CH_3OH)_{ads} \qquad\qquad 2.49$$

$$Pt - (CH_3OH)_{ads} \rightarrow Pt - (^{\bullet}CH_2OH)_{ads} + H^+_{aq} + e^- \qquad\qquad 2.50$$

$$\text{or} \quad Pt - (CH_3OH)_{ads} \rightarrow Pt - (CH_3O^{\bullet})_{ads} + H^+_{aq} + e^- \qquad\qquad 2.51$$

$$Pt - (^{\bullet}CH_2OH)_{ads} \rightarrow Pt - (^{\bullet}CHOH)_{ads} + H^+_{aq} + e^- \qquad\qquad 2.52$$

$$\text{or } Pt-(CH_3O^{\bullet})_{ads} \rightarrow Pt - (CH_2O^{\bullet})_{ads} + H^+_{aq} + e^- \qquad\qquad 2.53$$

$$Pt-(^{\bullet}CHOH)_{ads} \rightarrow Pt - (^{\bullet}CHO)_{ads} + H^+_{aq} + e^- \qquad\qquad 2.54$$

$$\text{or} \quad Pt - (CH_2O^\bullet)_{ads} \rightarrow Pt - (^\bullet CHO)_{ads} + H^+_{aq} + e^- \qquad \qquad 2.55$$
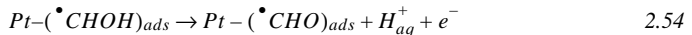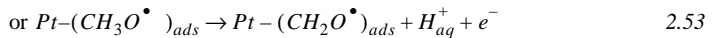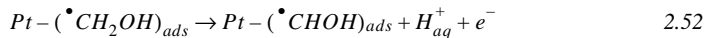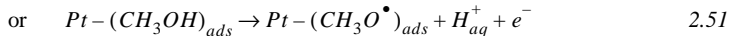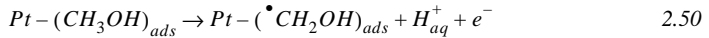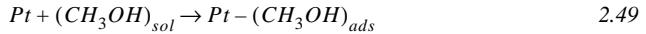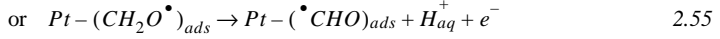
Reactions 2.54 and 2.55 lead to the formation of formyl-like species ($^\bullet CHO)_{ads}$, which are spontaneously dissociated on pure platinum:

$$Pt - (^\bullet CHO)_{ads} \rightarrow Pt - (^\bullet CO)_{ads} + H^+_{aq} + e^- \qquad \qquad 2.56$$
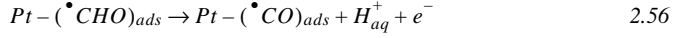
The strongly adsorbed CO species are responsible for the poisoning of the electrode active sites. ($^\bullet CHO)_{ads}$ intermediates can be considered either as active intermediates that lead to the final oxidation product or precursors of the poisoning species. The oxidation of these species requires the presence of OH species, which are formed by the dissociative adsorption and the hydrogen discharge (Equation 2.45 and Equation 2.46) arising from the dissociation of water according to the global reaction:

$$Pt + H_2O \rightarrow Pt - (OH)_{ads} + H^+_{aq} + e^- \qquad \qquad 2.57$$
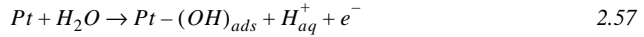
Pt-(OH)$_{ads}$ reacts then with Pt-($^\bullet CHO)_{ads}$ to form CO$_2$ either directly (2.58) or via Pt-($^\bullet COOH)_{ads}$ (2.59, 2.60):

$$Pt - (OH)_{ads} + Pt - (^\bullet CHO)_{ads} \rightarrow 2Pt + CO_2 + 2H^+_{aq} + 2e^- \qquad \qquad 2.58$$

$$Pt - (OH)_{ads} + Pt - (^\bullet CHO)_{ads} \rightarrow Pt + Pt - (^\bullet COOH)_{ads} + H^+_{aq} + e^- \qquad \qquad 2.59$$

$$Pt - (^\bullet COOH)_{ads} \rightarrow Pt + CO_2 + H^+_{aq} + e^- \qquad \qquad 2.60$$
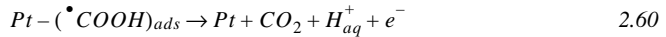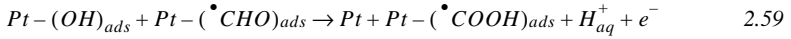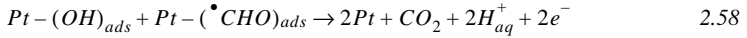
At higher potential, the poisoning $^\bullet$CO can be oxidized:

$$Pt - (^\bullet CO)_{ads} + Pt - (OH)_{ads} \rightarrow 2Pt + CO_2 + H^+_{aq} + e^- \qquad \qquad 2.61$$

$$\text{or } Pt - (^\bullet CO)_{ads} + Pt - (OH)_{ads} \rightarrow Pt + Pt - (^\bullet COOH)_{ads} \qquad \qquad 2.62$$
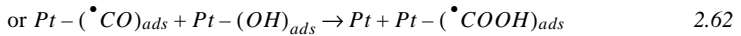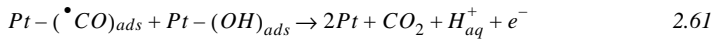
The previous reaction (2.62) is followed by reaction 2.60. The rapidity of reaction 2.56 is the main reason for the fast poisoning phenomenon observed on pure platinum. To improve the kinetics of the overall reaction, the adsorption properties of Pt have to be modified. One alternative is to increase the adsorbed OH coverage at low potentials by adding a second metal, on which water is more easily dissociated at lower potential.

Ruthenium is known to be an efficient second component to enhance the electrooxidation of methanol at platinum. Indeed, its presence increases the number of adsorbed OH species on the electrode surface at low potentials. Moreover, Ru minimizes the formation of CO poisoning species. The mechanism described above is thus modified by the promoting effect of Ru and becomes bifunctional. In this case, adsorbed OH are produced according to reaction 2.57 at platinum but also at ruthenium according to the following reaction:

$$Ru + H_2O \rightarrow Ru - (OH)_{ads} + H^+_{aq} + e^- \qquad 2.63$$
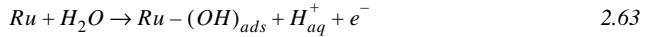
The oxidation of formyl (Equation 2.58) is also performed by Ru:

$$Pt - (^{\bullet}CHO)_{ads} + Ru - (OH)_{ads} \rightarrow Pt + Ru + CO_2 + 2H^+_{aq} + 2e^- \qquad 2.64$$
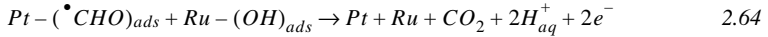
The removal of adsorbed $^{\bullet}$CO by oxidation with adsorbed OH may occur at platinum sites (reaction 2.61 or reaction 2.62 followed by 2.60) or at Ru sites:

$$Pt - (^{\bullet}CO)_{ads} + Ru - (OH)_{ads} \rightarrow Pt + Ru + CO_2 + H^+_{aq} + e^- \qquad 2.65$$

$$or \ Pt - (^{\bullet}CO)_{ads} + Ru - (OH)_{ads} \rightarrow Ru + Pt - (^{\bullet}COOH)_{ads} \qquad 2.66$$
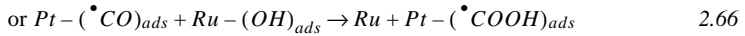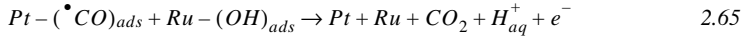
The reaction 2.66 is followed by the reaction 2.60. Some CO species migrate from platinum sites and are adsorbed at ruthenium sites. Therefore, it is also possible to consider the similar reactions between Ru-($^{\bullet}$CO)$_{ads}$ and Ru-(OH)$_{ads}$.

In summary, in the case of methanol oxidation, three points have to be fulfilled: the dissociation of MeOH, the production of a sufficient concentration of adsorbed oxygenated species at low potential, and the easy removal of the poisoning species (or their limitation). Platinum and ruthenium fulfill the two first conditions but the third could be further improved by a third metal (e.g. molybdenum).

The oxidation of methanol at Pt electrode and Pt-Ru electrode can be illustrated by Figure 2.19 and Figure 2.20 [30].
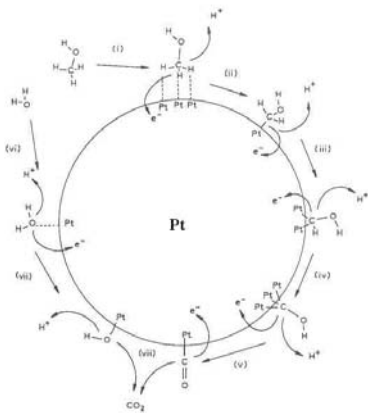
Figure 2.19 Reaction scheme of the possible methanol electrooxidation process at Pt electrode.
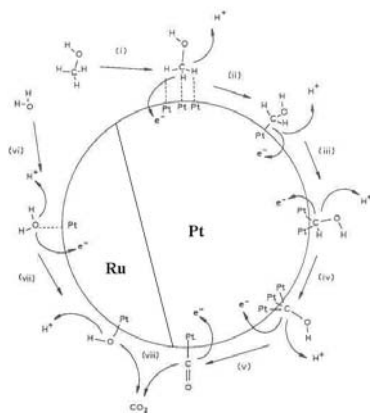
Figure 2.20 Reaction scheme of the possible methanol electrooxidation process at Pt-Ru electrode.

Electrochemical formation of OH radicals via water discharge

When the potential is higher than the thermodynamic one for water decomposition, the formation of hydroxyl radicals is performed in one step via the electrochemical water discharge.

$$H_2O \rightarrow HO^\bullet + H^+ + e^- \qquad\qquad 2.67$$

The strength of the electrode - $^\bullet$OH interaction depends on the nature of the electrode material. The relation between the electrode - $^\bullet$OH interaction and the reactivity of these hydroxyl radicals will be discussed in detail in Chapter 3.

Redox potential of OH radicals

The formation of free hydroxyl radicals in aqueous solution necessitates a high anodic potential. Even if the measure of this potential is difficult because of the high reactivity of OH radicals, some calculated values were determined. The values are based on gas-phase measurements of standard Gibbs energy, and assumptions about the free energy in solution. Schwarz *et al.* [31, 32] have investigated the generation of free radicals

by radiolysis of aqueous solutions. Free energies and heats of solution have been estimated from the gas phase values to determine the half-cell potentials. OH radicals appear as the strongest oxidant with a potential of 2.65 V vs *SHE* in acidic medium [33, 34]. Other references estimated the $^\bullet$OH redox potential between 2.6 and 2.8 V [34-37].

OH radicals are highly oxidizing and widely used for water treatment. Table 2.2 summarizes the redox potential of some chemical systems known to treat water.

Oxidant	Redox potential (V vs *SHE*)
F_2	3.03
$HO^\bullet$	2.80
$O^\bullet$	2.42
O_3	2.07
H_2O_2	1.78
Cl_2	1.36

Table 2.2 Redox potential of some chemical systems used for water treatment [38].

In neutral solution, its potential was found to be equal to 1.8 V. The high overvoltage for oxygen evolution on BDD electrode allows this reaction. The crucial point in this work is to define if, in the case of BDD electrodes, hydroxyl radicals can be considered as free hydroxyl radicals. In that case, their reactivity should be similar to the hydroxyl radicals produced chemically.

Electrochemical Fenton process [39]

The Fenton reaction, which is well known to chemically produce hydroxyl radicals will be explained in detail in the next paragraph. This reaction involving both ferrous iron and hydrogen peroxide can be used electrochemically according to two processes: cathodic and anodic Fenton processes. In cathodic process, Fe(II) can be directly added or produced by the reduction of Fe(III) at the cathode:

$$Fe^{3+} + e^- \rightarrow Fe^{2+} \qquad\qquad 2.68$$

H_2O_2 may be also either added or formed by the reduction of O_2 at the cathode:

$$O_2 + 2H^+ + 2e^- \rightarrow H_2O_2 \qquad\qquad 2.69$$

The cathodic process takes place at neutral pH. The main advantage of this technique is the continuous production of Fe(II) and hydrogen peroxide.

In the anodic Fenton process, an iron electrode is used as anode and plays the role of source of ferrous ions. The reaction occurs under acidic pH conditions and with a high current efficiency.

6.1.2. Chemical production [40]

Fenton reaction

This method is probably the oldest and the most used technique to produce hydroxyl radicals. In 1894, H. J. H. Fenton [41] reported that ferrous ions strongly promote the oxidation of malic acid by hydrogen peroxide. Subsequent works have shown that the combination of ferrous salt and H_2O_2 produces an effective oxidant of a wide variety of organic substances such as phenols and herbicides. This mixture was called «Fenton's reagent». The Fenton reaction is, compared to other methods, inexpensive and requires no special devices. However, this method has some disadvantages such as the addition and the consumption of ferrous salts and the requirement of an aqueous medium, in which the solubility of most organics is not satisfactory. Hydrogen peroxide is not a strong oxygen transfer agent, but the oxidation of organics is improved in the presence of Fe^{2+} ions because the reaction leads to the formation of highly oxidizing OH radicals according to Fenton's mechanism [42]. The first step is the initiation reaction, in which the ferrous ions are oxidized by H_2O_2:

$$Fe^{2+} + H_2O_2 \rightarrow Fe^{3+} + OH^- + HO^\bullet \qquad\qquad 2.70$$
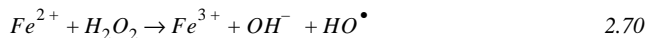
The radical chain reactions lead to the oxidation of the organic compounds, either by hydrogen abstraction reaction, redox reaction or electrophilic addition. The parameters of the reaction are optimized in order to favor the addition of OH group and the abstraction of hydrogen. An excess of H_2O_2 or Fe^{2+} might be detrimental because theses species can react with some of the intermediates like OH radicals:

$$Fe^{2+} + HO^{\bullet} \rightarrow Fe^{3+} + OH^{-} \qquad\qquad 2.71$$

$$H_2O_2 + HO^{\bullet} \rightarrow H_2O + HOO^{\bullet} \qquad\qquad 2.72$$
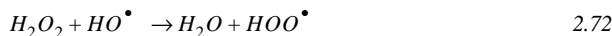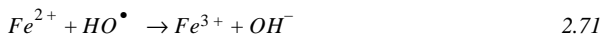
Therefore, it is necessary to optimize the ratios [H_2O_2]/[Fe(II)] and [Fe(II)]/[R] in order to minimize these reactions. The pH is also a very important parameter. Generally, the pH of the solution is adjusted to a value between 3 and 5, where the degree of oxidation of organics with Fenton is maximum [43]. When the pH is too high, the iron precipitates in $Fe(OH)_3$ and decomposes the hydrogen peroxide in oxygen. It has been found that the addition of some organic ligands (biodegradable and generally partially consumed in the process) enables the process to be carried out at higher pH by complexing ferric ions [39]. The mechanism of Fenton process includes a lot of reactions. Among the numerous intermediates, ferryl ion ($Fe^{IV}O^{2+}$) was found and is supposed to defavor the formation of hydroxyl radical [39].

H_2O_2 photolysis

UV-oxidation processes generally involve the generation of OH radicals through *UV*-photolysis of hydrogen peroxide [44]. The reaction between hydrogen peroxide and *UV* light leads to the formation of two hydroxyl radicals by homolytic cleavage of H_2O_2 (Equation 2.73)

$$H_2O_2 + h\nu \rightarrow 2HO^{\bullet} \qquad\qquad 2.73$$

Practically, this technique consists in illuminating an hydrogen peroxide solution with a light source in presence of an organic compound. The reaction yield depends on the wavelength that has to be lower than 280 nm. It is assumed that the yield is equal to two radicals formed *per* photon absorbed by 254 nm. The rate of H_2O_2 photolysis increases with pH. Hydroxyl radicals are very unstable and tend to react with the neighboring chemical species (especially hydrogen peroxide), making the process less effective.

The production of hydroxyl radicals can be also performed by both photolysis and Fenton reaction in a process called photoassisted Fenton. In this case, the wavelength (λ

> 300 nm) is adapted to carry out the transformation of Fe(III) complexes to Fe(II) rather than direct dissociation of H_2O_2:

$$Fe(OH)^{2+} + h\nu \rightarrow Fe^{2+} + HO^{\bullet} \qquad\qquad 2.74$$
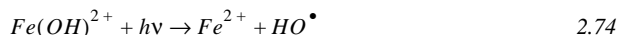
The system can also be improved by addition of ferrioxalate. The irradiation of ferrioxalate in acidic medium produces carbon dioxide and ferrous ions (free or complexed) that provide a source of Fe^{2+} to continue the Fenton reaction. This method is very efficient for the treatment of compounds difficult to oxidize such as pesticide, chlorophenols and nitrophenols [45].

Photocatalysis

In this process, a catalyst (generally TiO_2) produces electron-hole pairs by irradiation:

$$TiO_2 + h\nu \rightarrow e^- + h^+ \qquad\qquad 2.75$$

Since electrons are able to produce a superoxide radical ion, the holes oxidize adsorbed water or adsorbed hydroxyl ions to produce OH radicals (Equation 2.76, Equation 2.77):

$$TiO_2(h^+) + H_2O_{ads} \rightarrow TiO_2 + HO^{\bullet}_{ads} + H^+ \qquad\qquad 2.76$$

$$TiO_2(h^+) + HO^-_{ads} \rightarrow TiO_2 + HO^{\bullet}_{ads} \qquad\qquad 2.77$$
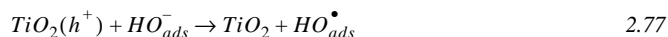
Water radiolysis

The water radiolysis consists in irradiating an air-saturated aqueous solution. Generally, the most used source is $^{60}Co(\gamma)$ but electron beam can be also used. The irradiation results in the formation of electronically excited states and free radicals. Hydroxyl radicals are produced during the first 30 seconds. After this time, other intermediates are produced and may interfere with OH radicals.

Ozone water system

Ozone is firstly produced by electric discharge of water and is decomposed in basic medium according to a chain reaction:

$$HO^- + O_3 \rightarrow O_2 + HO_2^- \qquad\qquad 2.78$$

$$HO_2^- + O_3 \rightarrow HO_2^\bullet + O_3^{-\bullet} \qquad\qquad 2.79$$

$$HO_2^\bullet \; \rightleftharpoons \; H^+ + O_2^{-\bullet} \qquad\qquad 2.80$$

$$O_2^{-\bullet} + O_3 \rightarrow O_2 + O_3^{-\bullet} \qquad\qquad 2.81$$

$$O_3^{-\bullet} + H^+ \rightarrow HO_3^\bullet \qquad\qquad 2.82$$

$$HO_3^\bullet \rightarrow HO^\bullet + O_2 \qquad\qquad 2.83$$

$$HO^\bullet + O_3 \rightarrow HO_2^\bullet + O_2 \qquad\qquad 2.84$$

Sonolysis [46]

Ultrasound is known to produce cavitation in liquid media. Cavitation bubbles are generated during the rarefaction cycle of the acoustic wave. The sonolytical cleavage of water molecules produces very reactive OH radicals [47]:

$$H_2O \rightarrow HO^\bullet + H^\bullet \qquad\qquad 2.85$$

The direct confirmation of the production of radicals was reported for the first time in 1983 by Makino *et al.* using electron spin resonance and DMPO as spin trap [48]. The free radicals may further proceed some secondary reactions to produce hydrogen peroxide or water.

6.2. Detection of hydroxyl radicals

Hydroxyl radicals are considered as a one of the numerous reactive oxygen species (ROS). OH radicals are quite reactive and readily damage biological molecules, including DNA. Therefore, their presence in biological systems is widely investigated. Several

methods have been developed to detect them, including *ESR* methods, which measure the electron paramagnetic resonance spectrum of a spin adduct derivative after spin trapping, or chromatographic methods, which determine the trapping products after the reaction with specific scavengers. Chromatographic methods are more used because of their ease of use. The specific markers currently used are all based on the ability of hydroxyl radicals to react with aromatic compounds (*e.g* salicylic acid) to produce hydroxylated compounds.

6.2.1. Direct detection

The direct detection and identification of short-lived free radicals by electron spin resonance (*ESR*) is theoretically possible. However, this technique is valid only if the radicals are produced in relatively high concentrations. The *ESR* technique is considered as the grade method for detection of free radicals. The *ESR*, also known as Electron Paramagnetic Resonance (*EPR*), is a technique used for the detection and the identification of compounds containing an odd number of electrons (transition metal species, radicals...). The sensitivity of this method allows the detection of concentrations as low as 10^{-8} M. Basically, the *ESR* measurement is based on the adsorption of the radiation of frequency, v, by paramagnetic species contained in a magnetic field H. This field creates a splitting of the unpaired electron energy levels equal to $g\mu_B H$, where g is the spectroscopic splitting (also known as g factor) and μ_B is the Bohr magneton $(5.788 \cdot 10^{-5}$ eV T$^{-1})$. The transitions are observed by adsorption of the incident radiation when the following relation is satisfied:

$$\Delta E \ = \ hv \ = \ g\mu_B H \qquad\qquad 2.86$$

The *ESR* spectrum is recorded by measuring the adsorption as a function of H while the magnetic field strength is scanned. The additional splitting of the energy levels by neighboring protons and other nuclei having magnetic moments and interacting with the unpaired electron leads to the hyperfine structure of the *ESR* spectrum.
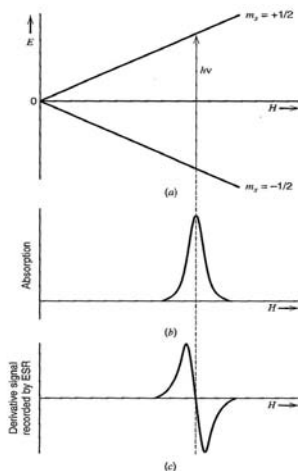
Figure 2.21 Principles of the *ESR* analysis. (a) Energy-level diagram of a free electron in a magnetic field, (b) *ESR* adsorption vs magnetic field, (c) Derivative *ESR* signal obtained after phase-sensitive detection [26].

The hyperfine splitting contains the information about the radical. These values are strongly influenced by the solvent. Buettner [49] has reviewed some spin adduct parameters for different solvents and different methods of radical production. In addition to the detection limit, some radicals, even if present at «high» concentrations, are not observable at room temperature as their spin relaxation times are very short, making their line width too broad to be observed by this technique. Spin trapping method allows to overcome these problems.

6.2.2. Indirect detection by spin trapping

Spin trapping is the most used method to detect hydroxyl radicals. This method was firstly investigated by Janzen [50] with the reaction of dehydrogenation of hydroaromatics with hot-benzene and thermal decomposition of nitro aromatics. Spin trapping consists in adding a spin trap to the short-lived radical, leading to the formation of a detectable radical called «spin adduct»:

$$R^{\bullet} + spin\ trap \rightarrow spin\ adduct \qquad\qquad 2.87$$
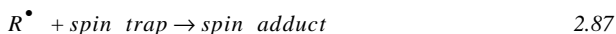
Spin traps are considered as specific markers and they are all based on the ability of hydroxyl radical to attack an aromatic compound.

The choice of the spin trap is dictated by the method of analysis of the spin adduct (electron spin resonance, *UV*-visible, chromatography) and its sensibility. Spin traps commonly used are nitrones or nitroso compounds that can form conjugates with some highly reactive free radicals to give rise nitroxide radicals (spin adduct). Nitroxides are relatively stable because the unpaired electron is stabilized by resonance. In this work, three spin traps were used:

5,5-dimethyl-1-pyrroline-N-oxide

5,5-dimethyl-1-pyrroline-N-oxide, called DMPO, is a diamagnetic nitroso compound, able to form long-lived nitroxide radicals that are detectable by *ESR* at room temperature. DMPO is thus widely used and some examples can be found in the literature [51, 52].
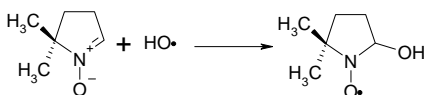

Figure 2.22 Reaction scheme of spin trapping between hydroxyl radicals and DMPO.

N-tert-butyl-α-phenylnitrone

N-tert-butyl-α-phenylnitrone (PBN) is also a common spin trap that presents some advantages. It is a stable compound, not so sensitive to light or oxygen. It is also soluble in a large number of solvents [50]. Its reaction with hydroxyl radicals is given below:
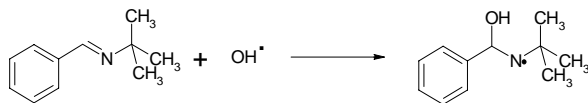
Figure 2.23 Reaction scheme of spin trapping between hydroxyl radicals and PBN.

p-nitrosodimethylaniline

Some works have been made with *p*-nitrosoaniline (RNO) as spin trap. Nitroso compounds undergo radicalar addition reactions, where the electrophilic radical (e.g OH radical) attacks the nitroso group by electron transfer to form a -$^{\bullet}$NOOH radical group.
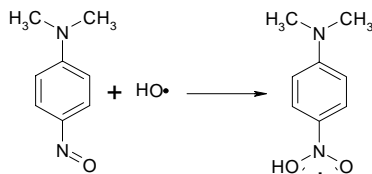
Figure 2.24 Reaction scheme of spin trapping between hydroxyl radicals and RNO.

The resulting adduct is very stable and incolore (while the RNO solution is yellow). RNO is often used as a standard substance in competition kinetics studies to determine the rate constant for the reaction of OH radicals with RNO. Neta *et al.* have firstly determined the rate constant between ethanol and OH radical, and concluded that $k = 1.25 \cdot 10^{10} \, \text{M}^{-1} \, \text{s}^{-1}$ for the reaction of OH radicals and RNO [53]. For spin trapping studies, it is necessary to be sure that only the concerning radical reacts with the spin trap. Kraljic *et al.* [54] have demonstrated that, in alkaline medium, RNO can not be attacked by peroxo intermediates or peroxide anion. Therefore, RNO seems to be a good candidate to investigate spin trapping.

Because of the high dipolar moment of its chromophore group, RNO can absorb in the visible with a maximum of 440 nm in neutral or basic medium and the analysis is generally done by *UV*-Visible measurements.

7. HYDROXYLATION OF AROMATIC COMPOUNDS

Firstly, we will deal with the hydroxylation of phenol. This reaction is well investigated, and can serve as a model to understand the hydroxylation of salicylic acid (because of the structure similarities).

7.1. Hydroxylation of phenol

Hydroxyl radicals can react via hydrogen abstraction or electrophilic attack. The mechanism of $^\bullet$OH addition on aromatic compounds is complex.

7.1.1. Chemical hydroxylation

As seen previously, hydroxyl radicals can be produced by several methods such as Fenton reaction, *UV*-photolysis, sonolysis... Various ortho:meta:para isomer ratios of hydroxyphenol have been reported by hydroxylation of phenol with hydroxyl radicals produced by chemical methods.

The first step of this reaction is a very fast electrophilic attack of the hydroxyl radical on the aromatic ring, which leads to the formation of a hydroxycyclohexadienyl radical as intermediate. Afterwards, the radical undergoes different reactions, depending on the conditions. In absence of an oxidizing reagent, dimerization and/or dismutation occurs. In the presence of oxidizing agents, the radical is oxidized in hydroxylated compounds. In the case of phenol, the first step could produced four dihydroxycyclohexadienyl radicals (in ipso, ortho, meta and para positions). The OH radical exhibits a strong preference for the addition at the positions activated by the OH group (electron rich ortho and para sites).

The complex addition of hydroxyl radical on aromatic compounds has been widely investigated on several derivatives (phenol, benzoic acid, salicylic acid, benzene, toluene...). In all experiments of phenol hydroxylation, the major product is catechol, meaning a preferential attack in ortho position [55-58]. Several investigations were focused on the possible explanation of this preferential attack.

Raghavan *et al.* [56] studied in detail the hydroxylation reaction of phenol (Figure 2.25). They considered that, theoretically, the reaction between $^\bullet$OH and phenol may produce three hydroxylated isomers (ortho, meta and para isomers) (the ipso-isomer was not considered because its oxidation reaction does not form a dihydroxylated compound). They assumed that each oxidation is performed with a rate constant $k(ox)_o$, $k(ox)_m$ and

$k(ox)_p$, respectively. These oxidation reactions are in competition with reactions that produce a phenoxyl radical (Figure 2.25).

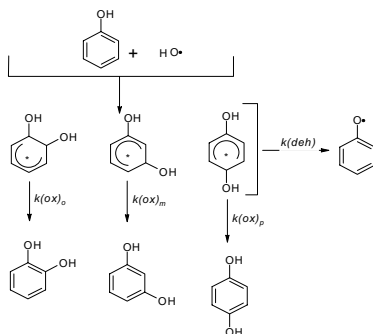**Figure 2.25** Hydroxylation and dehydratation reactions of phenol [56].

The hydroxylation products depend on at least two factors:

i) the nature of the directing group

ii) the nature of oxidant

The rate constants depend on the nature of oxidant and also on the isomer structure of the dihydroxycyclohexadienyl radical. The yields of catechol (ortho isomer), resorcinol (meta isomer) and hydroquinone (para isomer) were investigated and the rate constants were determined at pH 6. The following relation was established: $k(ox)_m/k(deh)_m < k(ox)_p/k(deh)_p < k(ox)_o/k(deh)_o$. On the basis of their investigations, the fractions of $^\bullet$OH attacks at the ortho, meta and para positions of phenol are 0.48, 0.08 and 0.36, respectively, corresponding to a majority of catechol. These results show the strong preference of the electrophilic OH radical for the ring position activated by the phenolic OH group.

Santos *et al.* have reported the catalytic oxidation of phenol in aqueous phase [57] and have compared the oxidation mechanism of several experiments, with or without catalysts. Irrespective of the assay, the first reaction is the hydroxylation in ortho or para positions leading to the formation of catechol or hydroquinone, respectively. Scheck *et al.* [58] have studied the degradation of phenol by *UV* radiation and obtained a majority of 1,2-dihydroxybenzene (catechol) as well as 1,4-dihydroxybenzene (hydroquinone), as expected by the various mechanisms.

Liu *et al.* [59] have investigated the influence of pH (from 2 to 12), the solvent effect (acetone, acetonitrile and water) and the molar ratio (phenol/H_2O_2) effect on the phenol hydroxylation by iron(II) phenanthroline. In all conditions, catechol was the major product (the ratio hydroquinone/catechol was equal to about 0.45).

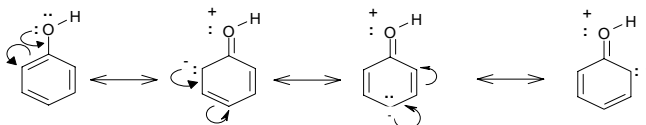The preferential attack in ortho position can be explained by the resonance forms of phenol:

Figure 2.26 Resonance forms of phenol.

Indeed, as regards on the resonance forms of phenol (Figure 2.26), an electrophilic attack is more likely to occur at ortho and para positions. However, there are two ortho positions for one para position, explaining the majority of catechol compared to hydroquinone.

7.1.2. Electrochemical hydroxylation

The oxidation of phenol using different electrode materials has been widely investigated in the last two decades. The interesting feature of this product is that it is considered to be an intermediate product in the oxidation pathway of higher molecular weight aromatic hydrocarbons. Thus, it is usually taken as a model compound for advanced waste water treatment.

In our laboratory, the electrochemical oxidation of phenol at boron-doped diamond has been investigated [60, 61]. The detected intermediates were hydroquinone (and benzoquinone) and catechol. In this case, the ortho- and para- selectivity is reversed. Indeed, on the contrary of the chemical hydroxylation (as shown before), the attack of hydroxyl radicals leads to a majority of the para-isomer.

Comninellis *et al.* [60] have compared the electrochemical oxidation of phenol with the chemical oxidation performed by H_2O_2 with acid catalyzed ($HClO_4$, H_3PO_4), Fenton reaction (Fe^{2+}) and the zeolite catalyst TS-1 [62]. In terms of ratio between hydroquinone and catechol, the following results were found:

	Acid catalyzed	Fenton reaction	Zeolite catalyst TS-1	Electrochemical Ti/IrO$_2$ anode
Hydroquinone *Catechol*	0.71	0.4	1	5

Table 2.3 Comparison between electrochemical and three types of phenol chemical oxidation.

According to the previous results, the product distribution for acid catalyzed and Fenton reaction is a majority of catechol compared to the concentration of hydroquinone. The third case, with the zeolite catalyst TS-1, gives a ratio of 1.

In a similar system (TS-1/H$_2$O$_2$), the para-selectivity (forming hydroquinone and benzoquinone) was enhanced with the coexistence of benzene or cyclohexane [63]. The ratio varies, in this case, between 2 and 5. This behavior is attributed to the coexistent bulky molecules imposing significant steric restriction on the transition state. The restriction is enhanced by the presence of phenol and benzene within the medium pores of TS-1. However, Chen *et al.* [64] have shown that a reversal of selectivity (between catechol and hydroquinone) occurs depending on whether the medium is acidic or basic.

Concerning the phenol oxidation carried out on Ti/IrO$_2$ anode, the ratio *R* (as defined in the chemical oxidation part) was 5, meaning a higher selectivity for hydroquinone than for catechol, as found with diamond electrode [60].

7.2. Hydroxylation of salicylic acid

Due to the ability of hydroxyl radicals to attack the benzene rings of aromatic molecules, the oxidation of salicylic acid (SA) is also a good method to investigate the presence of hydroxyl radicals. Salicylic acid is often used in biology because of its lack of toxicity. Indeed, SA can be safely administered to humans in doses that are sufficient to scavenge OH radicals. Moreover, the analysis of SA and its hydroxylation intermediates are very easy using chromatography techniques. Figure 2.27 represents the mechanism of SA hydroxylation. The attack of hydroxyl radicals on aromatic compounds leads to the formation of dihydroxylated products [65]. In the case of salicylic acid, the chemical hydroxylation results in the formation of 2,3- and 2,5-dihydroxylated benzoic acid (2,3- and 2,5-DHBA), with a higher amount of 2,3-DHBA.
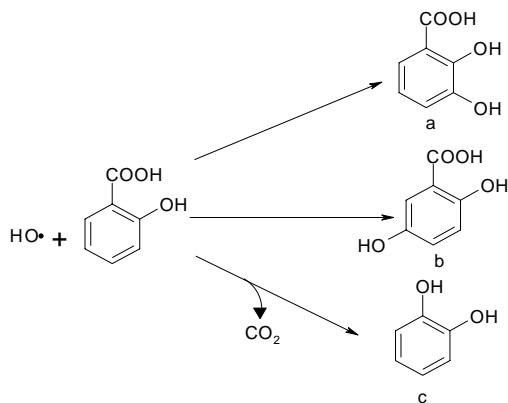
Figure 2.27 Mechanism of salicylic acid hydroxylation (a) 2,3-DHBA, (b) 2,5-DHBA, (c) Catechol.

When the reaction of decarboxylation occurs, the production of catechol is also observed. Salicylic acid contains both carboxyl and hydroxyl functional groups. From a structural point of view, we have to consider the activation effect of both groups. In both cases, resonance effects are more important than induction effects. Therefore, the hydroxyl group (normally decreasing the electronic density by induction) is a strong activator by resonance and increases the electronic density. The carboxyl group is a strong deactivator and has a tendency to decrease the electronic density of the aromatic ring [66]. Since the influence of the activator substituent is dominating, the hydroxylation of salicylic acid takes place in ortho and para positions compared with the hydroxyl group. The concerted effect of the reaction of OH radicals with aromatics was investigated by Schuler *et al.* [67] with the specific case of the radiolytic oxidation of salicylic acid. They proposed that the electron population at the ortho position compared to that of para position is enhanced as a result of the hydrogen bonding in SA. Therefore, considering the strong electrophilic character of hydroxyl radical, the addition in ortho position is favored over addition in para position.

The primary step is considered to be an electrophilic attack of the hydroxyl radical on the ring to form a dihydroxycyclohexadienyl radical. After, depending on the nature of the radical and the solution radicals or the presence of oxidants, it may decay by elimination of water, dimerize or disproportionate or be oxidized, thus fixing the hydroxyl

moiety on the ring to give the stable hydroxylated product.

Maskos *et al.* [68] pointed out that the presence of redox active compounds can influence the distribution of salicylate hydroxylation. The reaction was investigated using γ-radiation and Fenton reaction as source of hydroxyl radicals. Using irradiation, the ratio of 2,3- to 2,5-DHBA is 5:1. This ratio increased with the irradiation time. Compared with the γ-radiation, the Fenton reaction enhanced the formation of 2,5-DHBA. The ratio could vary from 5 to 1.2 depending on the added oxidants, their concentrations and the pH used. Anyway, the formation of 2,3-DHBA is always higher than the one of 2,5-DHBA.

Since the nature of the oxidant seems to influence the isomer ratio (even if the trend does not change), we introduce in the following part, according to the literature, some concepts that can influence the isomer distribution during the reaction of salicylic acid hydroxylation.

7.2.1. Intramolecular hydrogen bonding (IMBH) in SA

An hydrogen bond is a strong electrostatic attraction occurring between two atoms, in which hydrogen is in covalent bond with highly electronegative elements (e.g F, O, N, Cl). Hydrogen bonding plays a role in the properties of compounds (solubility, boiling point) and also determines the shape of the molecule. The IMHB can sometimes be responsible for the molecular geometry as well as the stability of a certain predominant conformation. Because of the carboxyl and hydroxyl functional groups, salicylic acid (SA) and its anions (SA^{-1}) provide a good example to investigate the hydrogen bonding. Three types of IMBH were found in SA and its anions: the 6S six-membered ring type interfunctional groups, the weak 6W six-membered ring type interfunctional groups and the 4M intra-COOH (Table 2.4).
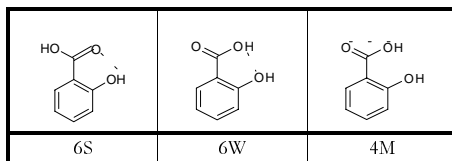

6S	6W	4M

Table 2.4 Three types of IMBHs in conformers/isomers of SA.

The three types of hydrogen bondings could force the related structures into a planar conformation. The computations performed by Chen *et al.* [69] conclude that salicylate

may possess very strong IMHB. The 6S configuration, where the intramolecular hydrogen bond is between the OH directly bonded to the benzene ring and the carbonyl (C=O) group on the carboxyl group, locks the OH group into the plane of the molecule, a geometry quite different from that of phenol.

7.2.2. Influence of pH

Jen *et al.* [70] investigated the influence of the pH on the formation of derivatives of salicylate in the trapping of OH radicals. They investigated the reaction of Fenton in water at different pH adjusted with sulfuric acid (2, 2.5, 3, 3.5, 4, 4.5 and 5). They concluded that the ratio of 2,3/2,5 decreases when pH increases, even if the concentration of 2,3-DHBA is always higher than 2,5-DHBA.

pH	2,5-/2,3-DHBA
2	0.11
2.5	0.18
3	0.42
3.5	0.48
4	0.71
4.5	0.83
5	0.69

Table 2.5 2,3/2,5-DHBA ratio at various pH values [70].

7.2.3. Enzymatic mechanism (cytochrome P450)

Some biological experiments [71] have compared the mechanisms of 2,3-DHBA or 2,5-DHBA formation. They all reported that the formation of 2,3-DHBA from salicylic acid is a mean to monitor free OH radical production, while the formation of 2,5-DHBA probably does not.

2,5-DHBA has been reported to be an enzyme-produced metabolite of salicylate in humans [72-74]. Ingelman-Sundberg *et al.* [75] have investigated the oxidation of SA with liver microsomal mixed-function oxidase systems in order to monitor which isomer is produced. Their results showed that the formation of 2,3-DHBA from salicylate may represent a product of free radical attack while the production of 2,5-DHBA may arise by enzymatic metabolism of salicylate.

Cytochrome P450 is a prosthetic group (cofactor covalently linked to an enzyme). It

is found in all tissues (expect muscle, bones and red blood cells) in the endoplasmic reticulum and the mitochondria. This kind of enzyme is implicated in several metabolisms of oxidation.

The general equation of the hydroxylation by cytochrome P450 is given below:

$$RH + O_2 + H^+ + NADPH \rightarrow ROH + H_2O + NADP^+ \qquad 2.88$$
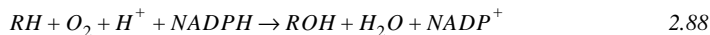
This reaction is assisted by ferric ions. The hydroxylation reaction catalyzed by the cytochrome P450 leads to the insertion of an oxygen atom in the substrate. The general mechanism can be summarized as follow:

• Fixation of the substrate on the active site of the enzyme.

• Reduction of ferric ions in ferrous ions by electron transfer.

• Adsorption of oxygen.

• Proton transfer from the substrate to oxygen and formation of radical intermediates.

• Addition of hydroxyl radical on $R^\bullet$ and formation of the hydroxylated product.

• Regeneration of the enzyme

It is now possible to establish a correlation between the behavior of cytochrome P450 and the electrochemical hydroxylation of salicylic acid. Indeed, the reactions present numerous similarities.

7.2.4. Singlet oxygen ($^1O_2$) reaction

Feix *et al.* [76] have investigated the reaction of salicylic acid with singlet oxygen $^1O_2$. They have found that 2,5-DHBA was the only intermediate. In another work [77], they tried to determine the stoechiometry between $^1O_2$ consumption and 2,5-DHBA production. They irradiated a solution of rose bengal and salicylic acid with visible light under aerobic conditions. The chromatographic detection showed that 2,5-DHBA was the major product of the reaction. When the same solution was irradiated under N_2 atmosphere, 2,5-DHBA was still the major product, although its concentration was smaller. In order to verify that the selective formation of 2,5-DHBA was not due to the selective decomposition of 2,3-DHBA, its stability was studied under the same conditions

in the presence or not of salicylic acid. They observed that the destruction of 2,3-DHBA was minimal and could not explain the previous results.

If it seems well established that the hydroxyl radical addition to SA is mediated by a cyclohexadienyl radical, the reaction between singlet oxygen and SA is presumably mediated via an endoperoxide intermediate. They proposed a mechanism of chemical quenching by $^1O_2$:
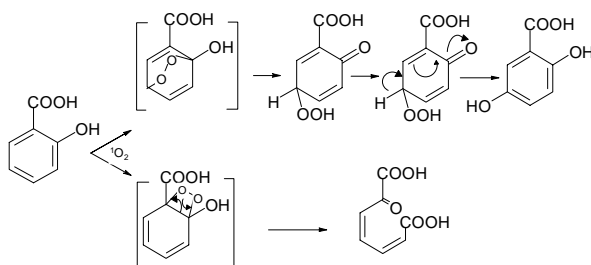

Figure 2.28 Mechanism of chemical quenching of salicylic acid [77].

If the formation of 2,5-DHBA is a proof of $^1O_2$ involvement, it is interesting to note that the reaction is enhanced in D_2O (slower consumption of SA and similar chemical yields [78]).

As shown by the previous figure, the 1,2-endoperoxide is very unstable and probably undergoes a ring-cleavage reaction that leads to the formation of an open chain aldehyde. According to these results, the reaction of singlet oxygen with salicylic acid leads to the selective formation of 2,5-dihydroxylated benzoic acid.

8. REFERENCES

[1]   H. Holden, *The Encyclopedia of Gemstones and Minerals*, 1991, M. Friedman Publishing Group, Inc., New York.

[2]   S. Ferro, *J. Mat. Chem.*, **12** (2002) 2843.

[3]   F.P. Bundy, H.T. Hall, H.M. Strong, and R.H. Wentorf, *Nature*, **176** (1955) 51.

[4]   S. Matsumoto, Y. Sato, T. Tsutsunumi, and N. Setaka, *J. Mat. Sci.*, **17** (1982) 3106.

[5]   M. Frenklach and S. Skokov, *J. Phys. Chem. B*, **101** (1997) 3025.

[6]   J.A. Smith, E. Cameron, M.N.R. Ashfold, Y.A. Mankelevich, and N.V. Suetin, *Diam. Relat. Mat.*, **10** (2001) 358.

[7]   J. Xu, M.C. Granger, Q. Chen, J.W. Strojek, T.E. Lister, and G.M. Swain, *Anal. Chem. News Features*, **1** (1997) 591 A.

[8]   Y.V. Pleskov, *Russ. Chem. Rev.*, **68** (5) (1999) 381.

[9]   K. Hashimoto, Y. Muraki, R. Baba, and A. Fujishima, *J. Electroanal. Chem.*, **397** (1995) 339.

[10]   Y.V. Pleskov, A. Sakharova, M.D. Krotova, L.L. Bouilov, and B.V. Spitsyn, *J. Electroanal. Chem.*, **228** (1987) 19.

[11]   R. Tenne, K. Patel, K. Hashimoto, and A. Fujishima, *J. Electroanal. Chem.*, **347** (1993) 409.

[12]   Y.E. Evstefeeva, Y.V. Pleskov, V.P. Varnin, and I.G. Teremetskaya, *Russ. J. Electrochem.*, **34** (2) (1998) 234.

[13]   A.D. Modestov, Y.E. Evstefeeva, Y.V. Pleskov, V.M. Mazin, V.P. Varnin, and I.G. Teremetskaya, *J. Electroanal. Chem.*, **431** (1997) 211.

[14]   Y.V. Pleskov, Y.E. Evstefeeva, M.D. Krotova, V.V. Elkin, V.M. Mazin, V.Y. Mishuk, V.P. Varnin, and I.G. Teremetskaya, *J. Electroanal. Chem.*, **455** (1998) 139.

[15]   L. Codognoto, S.A.S. Machado, and L.A. Avaca, *Diam. Relat. Mat.*, **11** (2002) 1670.

[16]   R. Ramesham and M.F. Rose, *Thin Solid Films*, **300** (1997) 144.

[17]   S. Ferro and A. De Battisti, *Electrochim. Acta*, **47** (2002) 1641.

[18]   M.N. Latto, D.J. Riley, and P.W. May, *Diam. Relat. Mat.*, **9** (2000) 1181.

[19]   I. Duo, *Control of electron transfer kinetics at boron-doped diamond electrodes by specific surface modification, Thesis N° 2732*. 2003, EPFL, Lausanne.

[20]   W. Haenni, P. Rychen, M. Fryda, and Ch. Comninellis, *Industrial applications of diamond electrodes*, in *Thin film Diamond Part B*, N. Ristein, Editor. 2004, Academic Press.

[21]   J. Iniesta, P.-A. Michaud, M. Panizza, and Ch. Comninellis, *Electrochem. Commun.*, **3** (2001) 346.

[22]   M. Panizza, I. Duo, P.-A. Michaud, G. Cerisola, and Ch. Comninellis, *Electrochem. Solid-State Lett.*, **3** (12) (2000) 550.

[23]   P.-A. Michaud, E. Mahe, W. Haenni, A. Perret, and Ch. Comninellis, *Electrochem. Solid-State Lett.*, **3** (2) (2000) 77.

[24]   D. Gandini, E. Mahé, P.-A. Michaud, W. Haenni, A. Perret, and Ch. Comninellis, *J. Appl. Electrochem.*, **30** (2000) 1345.

[25]   L. Gherardini, P.-A. Michaud, M. Panizza, Ch. Comninellis, and N. Vatistas, *J. Electrochem. Soc.*, **148** (2001) D78.

[26]   A.J. Bard and L.R. Faulkner, *Electrochemical methods - fundamentals and applications*, 2001, John Wiley & Sons, Inc, New York, 791.

[27]   R. Tenne and C. Levy Clément, *Isr. J. Chem.*, **38** (1998) 57.

[28]   R. Nicholson, *Anal. Chem.*, **37** (1965) 1351.

[29]   J.-M. Léger, *J. Appl. Electrochem.*, **31** (2001) 767.

[30]   M.P. Hogarth and T.R. Ralph, *Platinum Met. Rev.*, **46** (4) (2002) 146.

[31]   H.A. Schwarz, *J. Chem. Edu.*, **58** (2) (1981) 101.

[32]   H.A. Schwarz and R.W. Dodson, *J. Phys. Chem.*, **88** (1984) 3643.

[33]   P. Delahay, M. Pourbaix, and P. Van Rysselberghe. *Comportement électrochimique de l'oxygène, de l'eau oxygénée et des radicaux OH et HO$_2$*. in *2ème Réunion du Comité International de Thermodynamique et de Cinétique*. 1950. Milan: CR. CITCE, 2 (1950) 42.

[34]   W.H. Koppenol and J.F. Liebman, *J. Phys. Chem.*, **88** (1984) 99.

[35]   G.V. Buxton, C.L. Greenstock, W.P. Helman, and A.B. Ross, *J. Phys. Chem.*, **17** (2) (1988) 513.

[36]   U.K. Kläning, K. Sehested, and J. Holcman, *J. Phys. Chem.*, **89** (1985) 760-763.

[37]   G. Milazzo and S. Caroli, *Tables of standard electrode potentials*, ed. Wiley-Interscience, 1978, New York.

[38]   T.A. Egerton and P.A. Christensen, *Photoelectrocatalysis processes*, in *Advanced Oxidation Processes for Water and Wasterwater treatment*, S. Parsons, Editor. 2004, IWA: London.

[39]   S. Wadley and T.D. Waite, *Fenton processes*, in *Advanced Oxidation Processes for Water and Wastewater treatment*, S. Parsons, Editor. 2004, IWA: London.

[40]   R. Andreozzi, V. Caprio, A. Insola, and R. Marotta, *Catalysis Today*, **53** (1999) 51.

[41]   H.J.H. Fenton, *J. Chem. Soc.*, **65** (1894) 899.

[42]   M. Panizza and G. Cerisola, *Wat. Res.*, **35** (16) (2001) 3987.

[43]   S.H. Lin and C.C. Lo, *Wat. Res.*, **31** (8) (1997) 2050.

[44]   T.A. Tuhkanen, *UV/H$_2$O$_2$ processes*, in *Advanced Oxidation Processes for Water and Wastewater treatment*, S. Parsons, Editor. 2004, IWA: London.

[45]   C. Pulgarin, P. Péringer, P. Albers, and J. Kiwi, *J. Mol. Cat. A.: Chem.*, **95** (1995) 61.

[46]   T.J. Mason and C. Pétrier, *Ultrasound processes*, in *Advances Oxidation Processes for Water and Wastewater Treatment*, S. Parsons, Editor. 2004, IWA: London.

[47]   R.H. de Lima Leite, P. Cognet, A.-M. Wilhelm, and H. Delmas, *Chem. Eng. Sci.*, **57** (2002) 767.

[48]   K. Makino, M. Magdl, and P. Riese, *J. Phys. Chem.*, **87** (1983) 1369.

[49]   G.R. Buettner, *Free Rad. Biol. Med.*, **3** (1987) 259.

[50]   E.G. Janzen, *Acc. Chem. Res.*, **4** (1971) 31.

[51]   G. Liu, J. Zhao, and H. Hidaka, *J. Photochem. Photobiol. A: Chem.*, **133** (2000) 83.

[52]   E. Takahashi, T. Kurosu, K. Suga, Y. Nishiki, S. Wakita, M. Tanaka, and S. Nakamatsu. 2000, Tokyo.

[53]   P. Neta and L.M. Dorfman, *Adv. Chem. Ser.*, **81** (1968) 22.

[54]   I. Kraljic and C.N. Trumbore, *J. Am. Chem. Soc.*, **87** (12) (1965) 2547.

[55]   U. Jingjit, C. Bouchoule, M. Blanchard, and P. Canesson, *Cat. Today*, **1** (1987) 81.

[56]   N.V. Raghavan and S. Steenken, *J. Am. Chem. Soc.*, **102** (10) (1980) 3495.

[57]   A. Santos, P. Yustos, A. Quintanilla, S. Rodriguez, and F. Garcia-Ochoa, *Appl. Cat. B: Env.*, **39** (2002) 97.

[58]   C.K. Scheck and F.H. Frimmel, *Wat. Res.*, **29** (10) (1995) 2346.

[59]   C. Liu, X. Ye, R. Zhan, and Y. Wu, *J. Mol. Cat. A: Chem.*, **112** (1996) 15.

[60]   Ch. Comninellis and A. De Battisti, *J. Chim. Phys.*, **93** (4) (1996) 673.

[61]   J. Iniesta, P.-A. Michaud, M. Panizza, G. Cerisola, A. Aldaz, and Ch. Comninellis, *Electrochim. Acta*, **46** (2001) 3573.

[62]   C.B. Dartt and M.E. Davis, *Ind. Eng. Chem. Res.*, **33** (1994) 2887.

[63]   T. Yokoi, P. Wu, and T. Tatsumi, *Catal. Commun.*, **4** (2003) 11.

[64]   J. Chen, L. Eberlein, and C.H. Langford, *J. Photochem. and Photobiol. A : Chem.*, **148** (2002) 183.

[65]   B. Halliwell and M. Grootveld, *FEBS Lett.*, **213** (1987) 9.

[66]   G.W. Klein, K. Bhatia, V. Madhavan, and R.H. Schuler, *J. Phys. Chem.*, **79** (17)

(1975) 1767.

[67]   G. Albarran and R.H. Schuler, *Rad. Phys. Chem.*, **67** (2003) 279.

[68]   Z. Maskos, J.D. Rush, and W.H. Koppenol, *Free Rad. Biol. Med.*, **8** (1990) 153.

[69]   C. Chen and S.-F. Shyu, *J. Mol. Struct.*, **536** (2001) 25.

[70]   J.-F. Jen, M.-F. Leu, and T.C. Yang, *J. Chromato. A.*, **796** (1998) 283.

[71]   C. Coudray and A. Favier, *Free Rad. Biol. Med.*, **29** (11) (2000) 1064.

[72]   C. Coudray, M. Talla, S. Martin, M. Fatôme, and M. Favier, *Anal. Biochem.*, **227** (1995) 101.

[73]   M. Grootveld and B. Halliwell, *Biochem. J.*, **237** (1986) 499.

[74]   D.R. McCabe, T.J. Maher, and I.N. Acworth, *J. Chromato. B.*, **691** (1997) 23.

[75]   M. Ingelman-Sundberg, H. Kaur, Y. Terelius, J.-O. Persson, and B. Halliwell, *Biochem. J.*, **276** (1991) 753.

[76]   J.B. Feix and B. Kalyanamaran, *Archives of Biochem. and Biophys.*, **291** (1) (1991) 43.

[77]   B. Kalyanamaran, S. Ramanujan, R.J. Singh, J. Joseph, and J.B. Feix, *J. Am. Chem. Soc.*, **115** (1993) 4007.

[78]   C. Richard and P. Boule, *J. Photobiol. A.: Chem*, **84** (1994) 151.

Chapter 3. Theoretical Part

1. INTRODUCTION

In this chapter, we will present theoretical models that allow us to predict the evolution of the electrochemical oxgen transfer reaction (EOTR) at boron-doped diamond electrode. Firstly, it is necessary to properly define what are *active* and *non active* electrodes. The knowledge of these two concepts permits to understand better the electrochemical behavior of diamond (which is considered as a *non active* material). This model highlights the role of hydroxyl radicals during oxidation processes at BDD anode.

The *COD-ICE* model allows the prediction of the evolution of two global parameters, namely, the chemical oxygen demand (*COD*) and the instantaneous current efficiency (*ICE*). From these evolutions, it is possible to construct a model for the oxidation reaction of any organic compound at BDD electrode. Depending on the conditions of the oxidative process (current density, concentration of organics), it is possible to observe either the evolution of the partial oxidation of the organic or its total combustion into CO_2.

Finally, the γ–ν model takes into consideration the rates of both hydroxyl radicals production and organics transport at the electrode as well as their stoechiometry. This

model is based on the fact that the oxidation reaction occurs close to the electrode, in a reaction cage. The percentage of aromatic intermediates compared to carbon dioxide indicates what reaction occurs (partial oxidation or combustion).

2. *ACTIVE* AND *NON ACTIVE* ELECTRODES IN EOTR

EOTR promising versatility, environmental compatibility and cost effectiveness have a continuously growing importance both in selective organic synthesis and in the electrochemical incineration (*ECI*) of organic pollutants in aqueous media. For organic electrosynthesis, the selectivity has to be enhanced. For *ECI* processes, the aim is the mineralization of the toxic and non-biocompatible pollutants with high current efficiency [1-10].

One can differentiate between direct and indirect oxidation. As seen in Chapter 2, in direct electrochemical oxidation, electron exchange takes place between the organic species and the electrocatalytic electrode surface. In indirect electrochemical oxidation, the organic compounds exchange with the surface through intermediation of electroactive species. The mediation may be performed by homogeneous mediators such as Ag^+, Ce^{3+}, Mn^{3+}, which are dissolved in the electrolyte and regenerated at the electrode surface after chemical reaction with the organics or by heterogeneous mediators fixed at the electrode surface. An indirect mechanism for the electrochemical oxidation of organics based on intermediates of oxygen evolution reaction in aqueous media has been proposed by D. C. Johnson [11-16].

In our laboratory, we have frequently found that the electrochemical oxidation of some organics in aqueous media took place, without any loss in electrode activity, only at high potentials with concomitant evolution of oxygen [1, 4-6, 9]. Furthermore, it has been found that the nature of the electrode material influences strongly both the selectivity and the efficiency of the process [2, 4, 17, 18]. To interpret these observations, a comprehensive model for anodic oxidation of organics in acid medium, including the competition with oxygen evolution has been proposed.

The model (Figure 3.1) permits to illustrate the difference between two limiting cases, *active* and *non active* anodes.
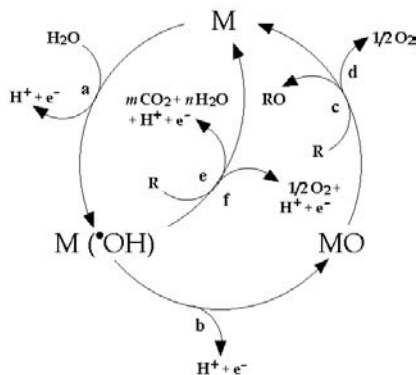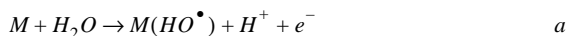
Figure 3.1 Scheme of the electrochemical oxidation of organic compounds on *active* anodes (reactions a, b, c, d) and *non active* anodes (reactions a, e, f). M designates an active site at the anode surface.

In both cases, the first reaction (Equation a) is the discharge of water molecules leading to the formation of adsorbed hydroxyl radicals:

$$M + H_2O \rightarrow M(HO^\bullet) + H^+ + e^- \qquad\qquad a$$

The electrochemical and chemical reactivity of the adsorbed hydroxyl radicals depends strongly on the nature of the electrode material used.

(i) At *active* electrode, there is a strong interaction between the electrode (M) and the hydroxyl radicals $(HO^\bullet)$. In this case, the adsorbed hydroxyl radicals may interact with the anode with possible transition of the oxygen from the hydroxyl radical to the electrode surface, forming a so-called higher oxide MO (Equation b). This may be the case when higher oxidation states on the surface electrode are available above the thermodynamic potential for oxygen evolution (1.23 V vs SHE).

$$M(HO^\bullet) \rightarrow MO + H^+ + e^- \qquad\qquad b$$

We speculate that at *active* electrodes, the surface redox couple MO/M can act as a mediator in the oxidation of organics (Equation c). This reaction is in competition with the side reaction of oxygen evolution due to the chemical decomposition of the higher

oxide (Equation d):

$$MO + R \rightarrow M + RO \qquad\qquad c$$

$$MO \rightarrow M + \frac{1}{2}O_2 \qquad\qquad d$$

The oxidation reaction via the surface redox couple MO/M (Equation c) may be much more selective than the reaction involving hydroxyl radicals (Equation e).

(ii) At *non active* electrode, there is a weak interaction between the hydroxyl radicals and the electrode surface. In this case, the oxidation of organics is mediated by hydroxyl radicals (Equation e) and may result in fully oxidized reaction products such as CO_2.

$$M(HO^\bullet) + R \rightarrow M + mCO_2 + nH_2O + H^+ + e^- \qquad\qquad e$$
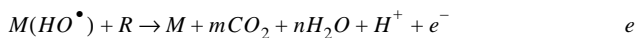
In this schematic equation, R is the fraction of an organic compound containing no heteroatom, which needs one oxygen atom to be transformed to fully oxidized compounds. This reaction is in competition with the side reaction of hydroxyl radicals discharge (direct or indirect through the formation of hydrogen peroxide as intermediates) to oxygen (Equation f) without any participation of the anode surface:

$$M(HO^\bullet) \rightarrow M + \frac{1}{2}O_2 + H^+ + e^- \qquad\qquad f$$
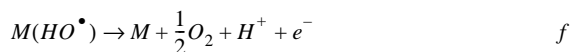
A *non active* electrode does not participate in the anodic reaction and does not provide any catalytic active site for adsorption of reactants and/or products in aqueous medium. In this case, the anode serves only as an inert substrate, which can act as a sink for the removal of electrons. In principle, only *outer sphere* reactions and water discharge are possible on this type of anode. The intermediates produced by the water decomposition are involved in the oxidation of organics in aqueous medium, resulting in the electrochemical incineration.

The electrochemical activity (overpotential for oxygen evolution) and chemical reactivity (rate of organics oxidation with electrogenerated hydroxyl radicals) of adsorbed $HO^\bullet$ are strongly linked to the strength of the $M - HO^\bullet$ interaction. As general rule, the weaker the interaction, the lower the anode reactivity toward oxygen evolution (high overvoltage anodes) and the higher the anode reactivity for organics oxidation (fast chemical reaction). Boron-doped diamond based anode (BDD) is a typical *non active* electrode with high anodic stability and acceptable conductivity.

This model assumes that the electrochemical oxidation is mediated by hydroxyl radicals, either adsorbed at the surface in the case of *active* surfaces or free in the case of *non active* ones.

This model was used in some papers for the electrochemical oxidation of organic compounds at different electrodes. According to the model, Bock *et al.* [19] proposed that the removal rate of organics (p-benzoquinone) depends on the nature of the anode material. Saracco *et al.* studied the oxidation of coumaric acid at Pt-Ti electrode [20] and identified two intermediates, namely, p-benzoquinone and spiro-lactone. They have postulated that the benzoquinone is formed through reactions mostly occurring over the electrode surface, whereas, spiro-lactone formation takes place principally in the bulk of the solution.

3. MODELING OF OXIDATION

3.1. *COD-ICE* model

The model of EOTR on BDD anodes was developed for a batch recirculation reactor system under galvanostatic conditions, with the following assumptions [21]:

• the reaction is fast, under diffusion control,

• the oxidation of organics in the bulk with electrogenerated oxidants like hydrogen peroxide or persulfate is not considered,

• the reservoir volume is much greater than that of the electrochemical reactor and considered as perfectly mixed,

• the adsorption of the organics at the electrode surface is negligible.

Bulk oxidation reactions are often characterized through the study of global parameters. These parameters allow following the evolution of the electrochemical reaction and give a general idea of the advance of the oxidation (especially when all by-products are not known). The first one is the Chemical Oxygen Demand (*COD*), which represents a measure of the oxygen equivalent of the organic matter susceptible to be oxidized by a strong chemical oxidant. The value of the *COD* is calculated from the

following equation:

$$C_xH_yO_z + \left(x + \frac{y}{4} - \frac{z}{2}\right)O_2 \rightarrow xCO_2 + \left(\frac{y}{2}\right)H_2O \qquad \qquad 3.1$$
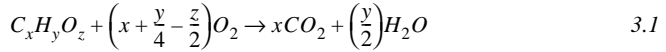
The *COD* value is given in concentration of oxygen ($molO_2$ m^{-3} or gO_2 m^{-3}).

The instantaneous current efficiency (*ICE*) is an other parameter that can be defined as the part of the current directly used for the oxidation reaction. The calculation can be performed from the decrease of *COD*:

$$ICE = \frac{4FV(\Delta COD)}{I\Delta t} \qquad \qquad 3.2$$

where F is the Faraday's constant (96485 C mol^{-1}), V the volume of the solution (m^{-3}), $\Delta(COD)$ ($molO_2$ m^{-3}) the decrease of *COD* during Δt and I the current (A).

A kinetic model has been developed for the electrochemical oxidation of organics in acidic medium, including the competition with oxygen evolution [21]. The limiting current density of the electrochemical oxidation is defined by Equation 3.3:

$$j_{lim} = nFk_mC \qquad \qquad 3.3$$

where j_{lim} is the limiting current density for the incineration of organic compounds (A m^{-2}), n is the number of exchanged electrons, F is the Faraday's constant (A s mol^{-1}), k_m is the mass transport coefficient (m s^{-1}) and C is the concentration of organics (mol m^{-3}).

For a given organic compound, the number of electrons involved in the incineration reaction can be calculated from the electrochemical reaction (Equation 3.4):
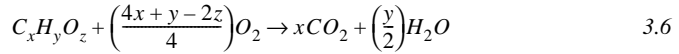
$$C_xH_yO_z + (2x - z)H_2O \rightarrow xCO_2 + (4x + y - 2z)H^+ + (4x + y - 2z)e^- \qquad 3.4$$
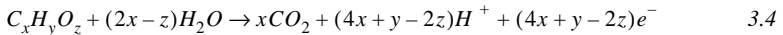
Replacement of the value of n by (4x + y - 2z) in Equation 3.3 turns the limiting current density into:

$$j_{lim} = (4x + y - 2z)Fk_mC \qquad \qquad 3.5$$

The relation (Equation 3.7) between the concentration C and the chemical oxygen demand *COD* can be obtained from the equation of the chemical incineration (Equation

3.6):

$$C_x H_y O_z + \left(\frac{4x+y-2z}{4}\right)O_2 \rightarrow xCO_2 + \left(\frac{y}{2}\right)H_2O \qquad\qquad 3.6$$

$$C = \frac{4}{(4x+y-2z)}COD \qquad\qquad 3.7$$

From Equation 3.5 and Equation 3.7, we can define the limiting current density for the electrochemical incineration of organic compounds, at a given time t, from the chemical oxygen demand (Equation 3.8):

$$j_{lim} = 4Fk_m COD_{(t)} \qquad\qquad 3.8$$

At time $t = 0$, (at the beginning of the electrolysis), the initial limiting current density is given by the following equation:

$$j_{lim}^0 = 4Fk_m COD^0 \qquad\qquad 3.9$$

where COD^0 is the initial chemical oxygen demand ($molO_2$ m^{-3}).

Under galvanostatic conditions, two different operating regimes are defined: at $j_{app} < j_{lim}$, the electrolysis is controlled by the charge transfer and at $j_{app} > j_{lim}$, it is controlled by the mass transport.

Electrolysis under charge transfer control ($j_{app} < j_{lim}$)

Under this condition, the current efficiency is 100%. The rate r ($molO_2$ m^{-2} s^{-1}) of *COD* removal is constant and is described by the following equation:

$$r = \frac{\alpha j_{lim}^0}{4F} \qquad\qquad 3.10$$

where α is the dimensionless current density defined as:

$$\alpha = \frac{j_{app}}{j_{lim}^0} \text{ with } 0 < \alpha < 1 \qquad\qquad 3.11$$

Using Equation 3.9, the rate constant r can be written as:

$$r = \alpha k_m COD^0 \qquad\qquad 3.12$$

In order to describe the temporal evolution of COD in a batch recirculated reactor system, the mass-balances over the electrochemical cell and the reservoir must be considered.

Since the volume of the electrochemical reactor (V_E) is much smaller than the reservoir volume (V_R), the mass-balance on COD for the electrochemical cell is obtained with the following relation:

$$\dot{V}COD_{out} = \dot{V}COD_{in} - \alpha A k_m COD^0 \qquad\qquad 3.13$$

where $\dot{V}$ is the flow rate (m^3 s^{-1}) through the electrochemical cell, COD_{in} and COD_{out} are the chemical oxygen demands (molO$_2$ m^{-3}) at the inlet and the outlet of the electrochemical cell, respectively and A is the anode area (m^2).

For the well-mixed reservoir, the mass-balance on COD can be expressed as:

$$\dot{V}(COD_{out} - COD_{in}) = V_R \frac{dCOD_{in}}{dt} \qquad\qquad 3.14$$

Combining Equation 3.13 and Equation 3.14 and replacing COD_{in} by the temporal evolution of COD, one obtains:

$$\frac{dCOD}{dt} = -\frac{\alpha A k_m COD^0}{V_R} \qquad\qquad 3.15$$

Considering the initial condition $COD = COD^0$ at $t = 0$, the temporal evolution of COD(t) is given by:

$$COD(t) = COD^0\left(1 - \frac{\alpha A k_m}{V_R}t\right) \qquad\qquad 3.16$$

This behavior persists until a critical time (t_{cr}), corresponding to the time at which the applied current density is equal to the limiting current density ($j_{app} = j_{lim}$). At the critical time, a critical value of COD can be calculated as follows:

$$COD_{cr} = \alpha COD^0 \qquad\qquad 3.17$$

From Equation 3.16 and Equation 3.17, the critical time t_{cr} is defined as:

$$t_{cr} = \frac{(1-\alpha)}{\alpha} \frac{V_R}{Ak_m} \qquad 3.18$$

Electrolysis under mass transport control ($j > j_{lim}$)

When the applied current density is higher than the limiting current density, side reactions occur. This results in the decrease of the instantaneous current efficiency *ICE*, which is defined by:

$$ICE = \frac{j_{lim}}{j_{app}} = \frac{COD(t)}{\alpha COD^0} \qquad 3.19$$

This case corresponds to $j_{app} > j_{lim}$ ($\alpha > 1$), when the applied current density is higher than the initial limiting current density. The *COD* mass-balances on the electrochemical cell and on the reservoir can be expressed as follows:

$$\frac{dCOD}{dt} = -\frac{Ak_m COD}{V_R} \qquad 3.20$$

By integration of Equation 3.20 with the initial conditions ($COD = COD^0$ at time t = 0), we obtain:

$$COD(t) = COD^0 \exp\left(-\frac{Ak_m}{V_R}t\right) \qquad 3.21$$

From Equation 3.19 and Equation 3.21, the instantaneous current efficiency *ICE* is defined by:

$$ICE = \frac{1}{\alpha}\exp\left(-\frac{Ak_m}{V_R}t\right) \qquad 3.22$$

Electrolysis under mixed control

The mixed control implies that the initial current is lower than the limiting current and that the final current is higher than the limiting one. The first domain (A in Figure 3.2) is the similar to the charge transfer control. After, the critical time (Equation 3.18), the system is controlled by the mass transfer (B in Figure 3.2).
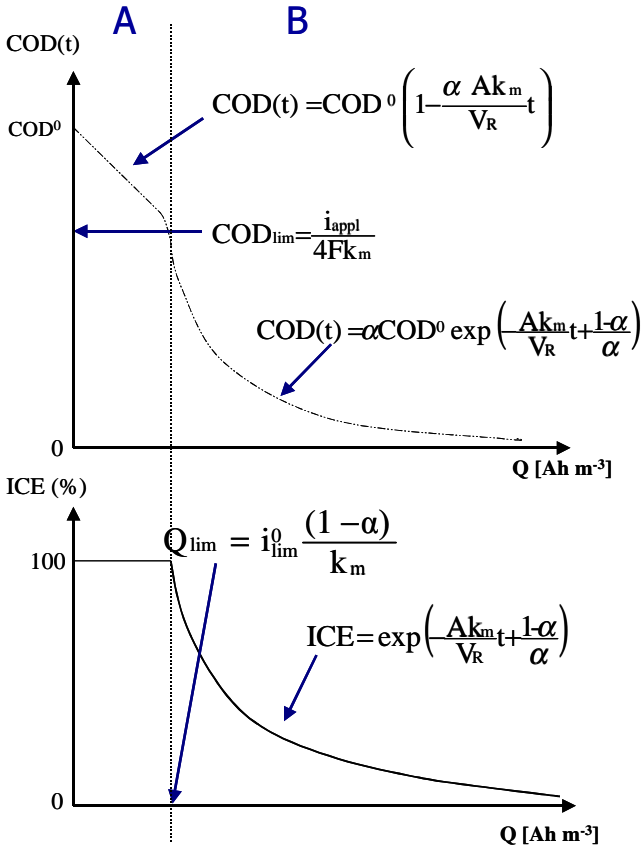
A   B

COD(t)

COD^0

$$COD(t) = COD^0\left(1 - \frac{\alpha\ Ak_m}{V_R}t\right)$$

$$COD_{lim} = \frac{i_{appl}}{4Fk_m}$$

$$COD(t) = \alpha COD^0 \exp\left(-\frac{Ak_m}{V_R}t + \frac{1-\alpha}{\alpha}\right)$$

0

$Q\ [Ah\ m^{-3}]$

ICE (%)

100

$$Q_{lim} = i_{lim}^0\frac{(1-\alpha)}{k_m}$$

$$ICE = \exp\left(-\frac{Ak_m}{V_R}t + \frac{1-\alpha}{\alpha}\right)$$

0

$Q\ [Ah\ m^{-3}]$

Figure 3.2 Evolution of COD and ICE. A represents the charge transfer control, B represents the mass transfer control.

By integration of Equation 3.20 with the initial conditions of $COD = \alpha COD^0$ at time $t = t_{cr}$, we obtain:

$$COD(t) = \alpha COD^0 \exp\left(-\frac{Ak_m}{V_R}t + \frac{1-\alpha}{\alpha}\right) \qquad 3.23$$

And the *ICE* is defined as:

$$ICE = \exp\left(-\frac{Ak_m}{V_R}t + \frac{1-\alpha}{\alpha}\right) \qquad 3.24$$

The Figure 3.2 illustrates graphically the evolution of the *COD* and *ICE* with the passed charge. A and B domains correspond to the charge and mass transfer control, respectively. The A domain shows a linear decrease of the chemical oxygen demand while the corresponding instantaneous current efficiency remains constant at 100%. Under these conditions, a partial oxidation occurs, leading to the formation of intermediates. In the B domain, both *COD* and *ICE* decrease exponentially. This behavior corresponds to a complete combustion of the organic compound into carbon dioxide.

This model gives predictions for *ICE* and *COD* as a function of time or charge during oxidation processes. These predictions were confirmed experimentally with numerous compounds classes such as carboxylic acids (acetic, formic, oxalic acid...), alcohols and ketones (methanol, ethanol, isopropanol...), phenolic compounds (phenol, 4-chlorophenol...) [22-24], aromatic acids (benzoic, salicylic, nicotinic acid...) [25] and soluble polymers such as polyacrylic acid [26].

3.2. γ-ν model

This model allows to describe EOTR in terms of flux. The oxidation process of an organic compound R is assisted by hydroxyl radicals produced by the water discharge and takes place in a reaction cage (RC) as shown in Figure 3.3. The RC corresponds to a reaction layer close to the electrode. Under galvanostatic conditions, the production rate of hydroxyl radicals generated at the BDD electrode is expressed by:

$$r_{HO^\bullet} = \frac{j_{app}}{F} \qquad 3.25$$

where $r_{HO^\bullet}$ is the production rate of $HO^\bullet$ (mol m^{-2} s^{-1}), j_{app} is the applied current density (A m^{-2}) and F is the Faraday's constant (A s mol^{-1}).

The flux of organic from the bulk to the anode surface is given by:

$$r_R = k_m[R] \qquad 3.26$$

where r_R is the flux of organics (mol m^{-2} s^{-1}), k_m is the mass transport coefficient in the electrochemical reactor (m s^{-1}) and [R] is the concentrations of organics in the bulk (mol m^{-3}).
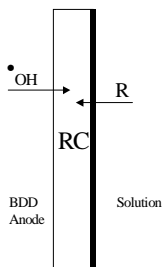
Figure 3.3 Scheme of the reaction cage (RC) for organics oxidation.

The parameter γ is defined as the ratio between the production rate of hydroxyl radicals and the flux of organics. Combining Equation 3.25 and Equation 3.26, one obtains the equation for γ:
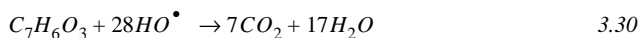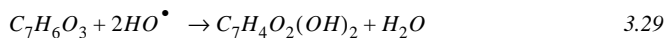
$$\gamma = \frac{r_{HO^\bullet}}{r_R} = \frac{j_{app}}{F k_m [R]} \qquad 3.27$$

The stoechiometric factor ν is defined as the ratio between the number of moles of hydroxyl radicals (equal to the number of electrons exchanged) involved in the reaction and the number of moles R (Equation 3.28):

$$\nu = \frac{\text{mol } HO^\bullet}{\text{mol } R} \qquad 3.28$$

Depending on the values of ν and γ, it is possible to obtain either the partial oxidation in aromatic compounds or the complete incineration into carbon dioxide.

For example, in the case of salicylic acid oxidation both partial oxidation (where ν equals 2, Equation 3.29) or complete incineration into CO_2 (ν is equal to the total number of electrons in the oxidation reaction, 28, Equation 3.30) can be considered:

$$C_7H_6O_3 + 2HO^\bullet \rightarrow C_7H_4O_2(OH)_2 + H_2O \qquad 3.29$$

$$C_7H_6O_3 + 28HO^\bullet \rightarrow 7CO_2 + 17H_2O \qquad 3.30$$

When the ratio γ is lower than the parameter ν, meaning that the flux of organics is

higher than the production of hydroxyl radicals, one can consider the reaction to be under the control of charge transfer. Therefore, the partial oxidation of the organics takes place. On the contrary, when γ becomes higher than ν, the reaction is under diffusion control leading to the total combustion of R. In the latter case, because of the high production rate of OH radicals, the intermediates can easily be oxidized in CO_2.

Partial oxidation

The rate of organic conversion, as well as the one of intermediates production is constant and defined by:

$$r = \frac{j_{app}}{2F} \qquad\qquad 3.31$$

From the mass-balance of the organic R and intermediates R' over the electrochemical reactor and the reservoir, one obtains:

$$\frac{d[R]}{dt} = -\frac{d[R']}{dt} = -\frac{j_{app}A}{2FV} \qquad\qquad 3.32$$

where *[R]* and *[R']* are the concentrations of the organic and the intermediates (mol m^{-3}), respectively, j_{app} is the applied current density (A m^{-2}), *A* is the electrode surface (m^2) and *V* is the reservoir volume (m^3).

Considering the initial conditions, at *t* = 0, *[R] = [R]$_0$* and *[R'] = 0*, the integration of Equation 3.32 gives:

$$[R] = [R]_0 - \frac{j_{app}A}{2FV}t \qquad\qquad 3.33$$

$$[R'] = \frac{j_{app}A}{2FV}t \qquad\qquad 3.34$$

Incineration of organics R into CO_2

During the electrolysis, the limiting current at a given time *t* is described in terms of *COD* by Equation 3.35:

$$j_{lim}(t) = 4Fk_m COD \qquad\qquad 3.35$$

where j_{lim} is the limiting current density (A m^{-2}), 4 is the number of exchanged electrons, *F* is the Faraday's constant (A s mol^{-1}), k_m is the average mass transport coefficient in the

electrochemical cell (m s^{-1}) and COD is the chemical oxygen demand (mol m^{-3}). Under these conditions of high current density, only a fraction of the applied current is used for the combustion, which is equal to the limiting current and the rest is used for the side reaction (oxygen evolution). Consequently, the rate of R removal (mol m^{-2} s^{-1}) is written as follows:

$$r = \frac{j_{lim}}{4F} = k_m COD \qquad\qquad 3.36$$

From the mass-balance of R over the electrochemical reactor and the reservoir, one obtains:

$$\frac{dCOD}{dt} = -\frac{A}{V}r = -\frac{Ak_m COD}{V} \qquad\qquad 3.37$$

where A is the electrode surface (m^2) and V the volume of the electrolyte (m^3).

By integration at the initial conditions ([R] = [R]$_0$ at $t = 0$), we obtain the temporal evolution of the COD (Equation 3.38):

$$COD = COD_0 \exp\left(-\frac{Ak_m}{V}t\right) \qquad\qquad 3.38$$

Another alternative to represent the partial oxidation or the combustion is to calculate percentages of carbon dioxide and aromatics (corresponding to the intermediates of the reaction). Indeed, we expect the total organic carbon (TOC) to remain constant during the selective oxidation while it should decrease during the combustion as a consequence of CO_2 formation. Similarly, the concentration of aromatics is low during the combustion.

The percentage of the organic R converted into carbon dioxide is given by the following relation:

$$\% CO_2 = \frac{([TOC]_0 - [TOC]_t)/x}{[R]_0 - [R]_t} \times 100 \qquad\qquad 3.39$$

where $[TOC]_0$ and $[TOC]_t$ are the total organic carbon at times 0 and t (mol m^{-3}), x is the mole number of CO_2 formed (see Equation 3.1), $[R]_0$ and $[R]_t$ are the organic concentrations at times 0 and t (mol m^{-3}), respectively.

The percentage of produced aromatics is defined by:

$$\% Aromatics = \frac{[Aromatics]}{[R]_0 - [R]_t} \times 100 \qquad\qquad 3.40$$

where $[Aromatics]$ are the concentrations (mol m^{-3}) of the aromatic intermediates.

4. CONCLUSIONS

The definition of *non active* electrode material permits to emphasize the preponderant role of hydroxyl radicals during EOTR at boron-doped diamond electrode. The first model permits to distinguish between *active* substrates like IrO_2, which are completely involved in the reaction by the formation of a higher oxide and *non active* materials like BDD that do not participate in the oxidation process.

The *COD-ICE* model highlights the importance of global parameters, especially the chemical oxygen demand, and the limiting current density for the prediction of the anodic reaction. It has been showed that a good optimization of the experimental conditions allows the prediction of either a partial oxidation or the incineration of organic pollutants.

It is also possible to describe the anodic reaction in terms of flux. The reaction is assumed to take place in the reaction cage, a layer very close to the electrode. Depending on the ratio between the rate of hydroxyl radicals production and the rate of organic transport, and depending on the stoechiometric ratio between the number of OH and organic moles, either partial oxidation or incineration take place. Therefore, the reaction is controlled by either charge transfer or diffusion, respectively.

These models will be applied in following chapters for 4-chlorophenoxyacetic acid and salicylic acid.

5. REFERENCES

[1]   N. Belhadj Tahar and A. Savall, *J. Electrochem. Soc.*, **145** (1998) 3427.

[2]   Ch. Comninellis, *Electrochim. Acta*, **39** (11-12) (1994) 1857.

[3]   Ch. Comninellis, *Gaz-Eaux-Eaux usées*, **11** (1992) 792.

[4]   Ch. Comninellis and A. De Battisti, *J. Chim. Phys.*, **93** (4) (1996) 673.

[5]   Ch. Comninellis and A. Nerini, *J. Appl. Electrochem.*, **25** (1) (1995) 23.

[6]   Ch. Comninellis and E. Plattner, *Chimia*, **42** (1988) 250.

[7]   Ch. Comninellis, E. Plattner, C. Seignez, C. Pulgarin, and P. Péringer, *Swiss Chem.*, **14** (1992) 25.

[8]   C. Pulgarin, N. Adler, P. Peringer, and Ch. Comninellis, *Wat. Res.*, **28** (4) (1994) 887.

[9]   K. Rajeshwar and J.G. Ibanez, *Environmental Electrochemistry, Fundamentals and Applications in Pollution Abattement*, 1997, Academic Press, London.

[10]   S. Stucki, R. Kötz, B. Carcer, and W. Suter, *J. Appl. Electrochem.*, **21** (1991) 99.

[11]   H. Chang and D.C. Johnson, *J. Electrochem. Soc.*, **137** (1990) 2452.

[12]   H. Chang and D.C. Johnson, *J. Electrochem. Soc.*, **137** (1990) 3108.

[13]   J. Feng and D.C. Johnson, *J. Electrochem. Soc.*, **137** (1990) 507.

[14]   J. Feng, D.C. Johnson, S.N. Lowery, and J.J. Carey, *J. Electrochem. Soc.*, **141** (10) (1994) 2708.

[15]   S.E. Treimer, J. Feng, M.D. Scholten, D.C. Johnson, and A.J. Davenport, *J. Electrochem. Soc.*, **148** (2001) E459.

[16]   J.E. Vitt and D.C. Johnson, *J. Electrochem. Soc.*, **139** (3) (1992) 774.

[17]   G. Fóti, D. Gandini, and Ch. Comninellis, *Curr. Top. Electrochem.*, **5** (1997) 71.

[18]   O. Simond, V. Schaller, and Ch. Comninellis, *Electrochim. Acta*, **42** (13-14) (1997) 2009.

[19]   C. Bock and B. MacDougall, *J. Electroanal. Chem.*, **491** (1-2) (2000) 48.

[20]   G. Saracco, L. Solarino, R. Aigotti, V. Specchia, and M. Maja, *Electrochim. Acta*, **46** (2-3) (2000) 373.

[21]   P.-A. Michaud, *Comportement anodique du diamant synthétique dopé au bore*, *Thesis N°2595*. 2002, EPFL, Lausanne.

[22]   L. Gherardini, P.-A. Michaud, M. Panizza, Ch. Comninellis, and N. Vatistas, *J. Electrochem. Soc.*, **148** (2001) D78.

[23]   J. Iniesta, P.-A. Michaud, M. Panizza, G. Cerisola, A. Aldaz, and Ch. Comninellis, *Electrochim. Acta*, **46** (2001) 3573.

[24]   M.A. Rodrigo, P.-A. Michaud, I. Duo, M. Panizza, G. Cerisola, and Ch. Comninellis, *J. Electrochem. Soc.*, **148** (5) (2001) 60.

[25]   F. Montilla, P.-A. Michaud, E. Morallón, J.L. Vásquez, and Ch. Comninellis, *Electrochim. Acta*, **47** (2002) 3509.

[26]   R. Bellagamba, P.-A. Michaud, Ch. Comninellis, and N. Vatistas, *Electrochem. Commun.*, **4** (2002) 171.

Chapter 4. Experimental Part

1. INTRODUCTION

This chapter deals with the description of the material used during this work (electrode, electrochemical cells) as well as analytical methods. First, we will give informations concerning the preparation of boron-doped diamond electrodes (performed by CSEM). Then, electrochemical cells will be described (electrochemical characterization cell, both one and two-compartments, and turbine cell). Finally, definitions of global parameters (*COD, TOC, ICE*) will be given as well as the details that concern their measurements.

2. PREPARATION OF BDD FILM

Boron-doped diamond films were synthesized by hot-filament chemical vapor deposition technique (HF-CVD, Chapter 2) on a conductive *p*-Si substrate (Siltronix). Electrodes were prepared at CSEM (Swiss Center for Electronics and Microtechnology, Neuchâtel). The distance between the filament and the silicon substrate was adjusted at

20 mm. The temperature of the filament ranged from 2440 to 2560°C and that of the substrate was kept at 830°C.

The reactive gas was composed of 1% methane in hydrogen containing 1 ppm of trimethylboron. The gas mixture was supplied in the reaction chamber at a flow rate of 5 L min^{-1} to obtain a growth rate of 0.24 μm h^{-1} for the diamond layer. The diamond film thickness was about 1 μm (with grain size from 200 to 800 nm) and the resistivity of 10-30 mΩ cm. The polycrystalline films were columnar, randomly textured. The boron/carbon ratio in the diamond films was between 4500 and 5500 ppm.

In this work, the diamond surface electrode was anodically pretreated in acidic medium (1M H$_2$SO$_4$) at 10 mA cm^{-2} for 30 minutes in order to eliminate the sp^2 carbon from the electrode surface.

3. ELECTROCHEMICAL CELL

3.1. Electrochemical characterization cell

The electrochemical characterization (used for cyclic voltammetry (CV), steady state polarization and rotating disk measurement) was carried out in a conventional three-electrode cell (Figure 4.1) using a computer-controlled Autolab PGstat30. Diamond or glassy carbon are used as working electrodes and are supported by a titanium plate, which is put in a Teflon cage (Figure 4.2). This set-up provided a geometric area of 1 cm^2. Hg/Hg$_2$SO$_4$,K$_2$SO$_4$ (sat) electrode was used as a reference and the counter-electrode was made of a Pt wire. The temperature was kept at 25°C.
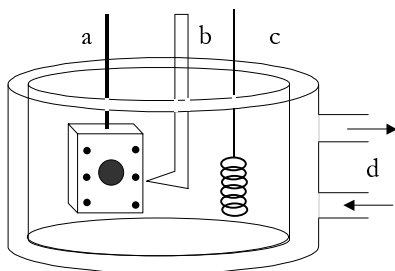
Figure 4.1 Schematic description of the three-electrodes electrochemical cell: (a) working electrode (BDD), (b) reference electrode (Hg/Hg$_2$SO$_4$), (c) counter electrode (Pt), (d) thermostat system [1].
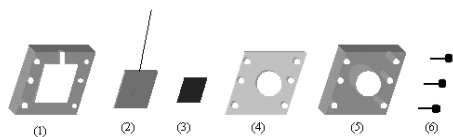
Figure 4.2 System for housing and mounting the working electrodes (3), cage made of teflon (1 and 5), gaskets of silicon material (4), screws (6) and metal support (2) of titanium [1].

3.2. One-compartment cell

The one-compartment electrochemical flow cell is shown in Figure 4.3 and Figure 4.4.
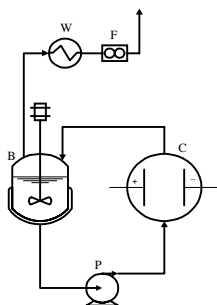
Figure 4.3 Schematic description of the one-compartment electrochemical flow cell. B: tank, C: electrochemical cell, P: pump, W: heat exchanger, F: gas flow controller [2].
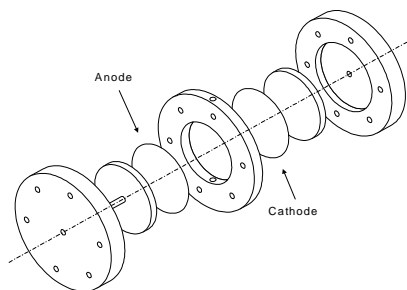
Figure 4.4 Tridimensional schematic description of the one-compartment electrochemical flow cell [2].

The anode and the cathode are disks made of BDD and zirconium, respectively. Both electrodes have a geometric area of 50 cm^2 with an inter-electrode gap of 10 mm. The electrodes are put on an aluminium support (AlMgSi1, Metallica, Crissier, CH). The electric contact is provided by a silver paste (EPO-TEK 410E, Polyscience AG, Cham, CH). Silicon resin (Elastosil E41, Wachker-Chemie, Munich, Ge) is used to render the cell watertight. The electrolyte is stored in a 500 mL thermo-regulated glass tank (B in Figure 4.3) and circulated through the electrolytic cell by a centrifugal pump (P in Figure 4.3) with a flow rate of 200 dm^3 h^{-1}. The electrolyte comes into the electrochemical cell through 5 mm orifices at both the inlet and outlet.

3.3. Two-compartments cell

In the two-compartments electrochemical flow cell, the anode and the cathode are separated by a Nafion$^{®}$ membrane N117/H^{+} (DuPont Polymers, Fayetteville, North Carolina). The schematic description is similar to that of the one-compartment cell. BDD was used as the anode and zirconium as the cathode. Both electrodes were disks with a geometric area of 63.6 cm^2. The volume of both anolyte and catholyte was 500 mL. They were stored in two thermoregulated tanks (T = 25°C) and circulated through the electrolytic cell by centrifugal pumps (Figure 4.5, Figure 4.6).
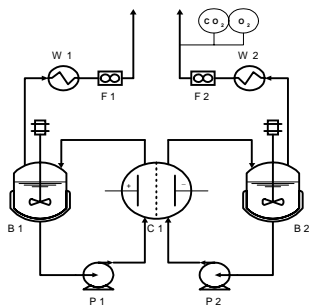
Figure 4.5 Schematic description of the two-compartments electrochemical flow cell. B1, B2: tanks, P1, P2: pumps, C1: electrochemical cell with membrane, W1, W2: heat exchangers, F1, F2: gas flow controllers.
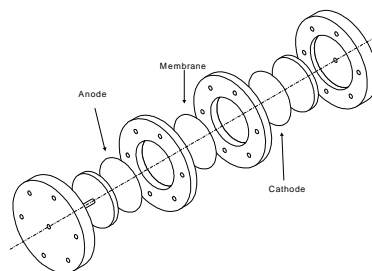
Figure 4.6 Tridimensional schematic description of the two-compartments electrochemical cell.

The membrane is pretreated by heating for 2 hours at 80°C in HNO$_3$ 2 M. Then it is rinsed 3 times with demineralized water.

3.4. Turbine cell

The turbine cell operates with a rotating electrolyte. On the contrary of the classical rotating electrode, the working electrode is fixed and the solution is kept in motion by a turbine. The turbine cell is constituted of a copper conductor base and a titanium slab, on which the diamond electrode is laid. The contact is provided by a silver paste (EPO-TEK 410E, Polyscience AG, Cham, CH). The geometric area is 0.8 cm^2. This system can be

used with two electrodes (counter and working electrodes) or three electrodes (counter, reference and working electrodes). The cell volume is 50 mL. The agitation of the electrolyte is provided by a turbine as shown in Figure 4.8. For the characterization of the cell, the working electrode was a platinum foil. For the oxidation of salicylic acid, a boron-doped diamond electrode was used as working electrode. In both cases, the counter-electrode was a platinum wire.
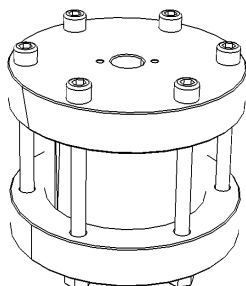
Figure 4.7 Schematic description of the turbine electrochemical cell.
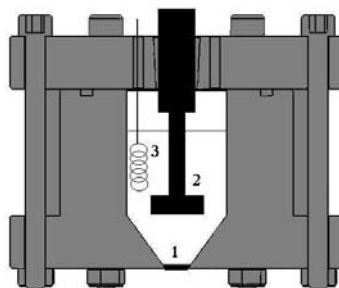
Figure 4.8 Cross section of the turbine electrochemical cell. (1) working electrode, (2) turbine, (3) counter-electrode. V_R = 50 mL.

4. GLOBAL PARAMETERS

4.1. Total organic carbon (*TOC*)

The total organic carbon (*TOC*) is the amount of organic carbon in the sample, expressed in concentration of carbon (molC L^{-1} or gC L^{-1}). The *TOC* test uses heat to oxidize organic compounds to carbon dioxide and water. Then, the amount of CO_2 is determined using infrared spectroscopy. The total organic carbon is measured on a TOC-5050 Shimadzu (Shimadzu Corporation, Tokyo, Japan). After acidification to eliminate inorganic carbon, the organic compound is oxidized with a pure flux of oxygen in a furnace at 680 °C containing Pt particles on Al_2O_3 catalyst. The resulting CO_2 is measured by infrared spectrometry. The obtained value is the average of three measurements and is given directly in mg of carbon per liter. The calibration is made with solutions of potassium hydrogenophtalate with different concentrations (20 up to 400 ppm). The precision of the analysis is 2%.

4.2. Chemical oxygen demand (*COD*)

The chemical oxygen demand (*COD*) represents the measure of the oxygen equivalent of organic matter contained in a sample susceptible to be oxidized by a strong chemical oxidant. The *COD* value is given in concentration of oxygen ($molO_2$ m^{-3} or gO_2 m^{-3}). The chemical oxygen demand is measured by the dichromate method *COD* Hach (Hach company, Loveland, Colorado). The oxidation takes place in a vial containing both silver compound as catalyst to oxidize resistant organics and mercuric sulfate to reduce interference from the oxidation of chloride ions by dichromate. 2 mL of solution are added in the vial and the mixture is allowed to react for 2 hours at 150°C at closed reflux. After cooling at room temperature, *COD* is measured with a spectrophotometer DR 2010 (Hach company). The value is directly given in ppm up to 1500 ppm. The precision of the measurement is about 2% but depends on the nature of the compound. The calibration is made with a potassium hydrogen phtalate solution.

4.3. Instantaneous current efficiency (*ICE*)

The instantaneous current efficiency (*ICE*) can be defined as the part of the current directly used for the oxidation reaction. The instantaneous current density is calculated from the variation of *COD*:

$$ICE = 4FV\frac{(COD)_t - (COD)_{t+\Delta t}}{I\Delta t} \qquad\qquad 4.1$$

where *(COD)$_t$* and *(COD)$_{t+Dt}$* are the *CODs* (in mol O_2 m^{-3}), *I* is the current (in A), *F* is the Faraday's constant (in A s mol^{-1}), and *V* is the volume of electrolyte (in m^{-3}).

5. REFERENCES

[1]   I. Duo, *Control of electron transfer kinetics at boron-doped diamond electrodes by specific surface modification*, *Thesis N° 2732*. 2003, EPFL, Lausanne.

[2]   P.-A. Michaud, *Comportement anodique du diamant synthétique dopé au bore*, *Thesis N°2595*. 2002, EPFL, Lausanne.

Chapter 5. Electrochemical characterization of BDD electrodes

1. INTRODUCTION

The knowledge of the electrochemical behavior of boron-doped diamond electrodes is essential for a better understanding and interpretation of the results observed in the oxidation process. The properties of diamond electrodes can be influenced by several parameters that depend essentially of the fabrication steps such as the doping level, the morphological structure (grain boundary, point defects), the crystallographic orientation, or the surface groups (H, O, F and sp^2 impurities) [1, 2].

As shown in the bibliographic part (Chapter 2), two kinds of charge transfer reactions can be considered: *outer sphere* and *inner sphere* reactions. The redox couple VOH/VO˙ (Figure 5.1) can be considered as an *outer sphere* system, which means that the kinetics is little influenced by the electrode material.
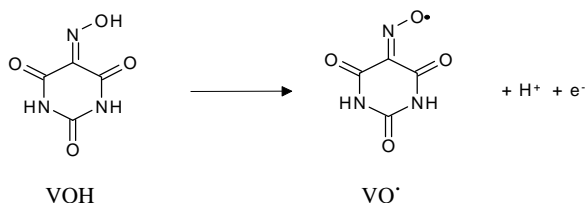
Figure 5.1 Scheme of the redox reaction of violuric acid.

Violuric acid (2,4,5,6(1H,3H)-pyrimidine-tetrone 5-oxime, VOH) is often employed as analytical reagent for chromatographic separation and for cation oxidation. It is widely used in the pulp bleaching techniques because the process is not very sensitive to temperature and pH variations [3]. VOH can be also used as an efficient electron transfer mediator in oxidation processes allowing the increase of the global rate of electron transfer. The main advantage of using violuric acid is its non toxic properties and its biodegradability. The oxidation of VOH leads to the formation of a radical (VOH/VO· couple). As shown in Figure 5.1, the reaction of violuric acid implies one electron and can be investigated in the potential region of water stability.

Electrochemical techniques allow to characterize a redox couple at a given electrode material. In this chapter, we have used three different techniques: cyclic voltammetry, steady-state polarization and rotating disk electrode. The aim of this investigation is to compare the key parameters measured by these methods. Indeed, while cyclic voltammetry is a transitory method, steady-state polarization is a stationary technique for which one can assume that only the charge transfer is considered. The use of rotating disk electrode allows to deal with a mixed control (both mass and charge transfer).

All the experimental results were compared with those obtained with a glassy carbon electrode (GC). It is well known that the main difference between boron-doped diamond and glassy carbon electrodes is the carbon hybridation present at the surface. The diamond surface contains mostly sp^3 carbon and some sp^2 impurities. On the contrary, glassy carbon is fully composed of sp^2 carbon. A lot of parameters can influence the properties of BDD electrode. Indeed, it has been shown that the level and the doping type, as well as the parameters previously quoted can play a role on the electrochemical behavior. The latter point seems to be particularly interesting and was investigated by Duo *et al.* [18, 67].

It has been proposed that sp^2 (non-diamond) states act as charge transfer mediators on BDD; explaining why the electrochemical activity of as-grown diamond (meaning no pretreatment) is higher than that of treated diamond (*e.g.* anodic polarization at 10 mA cm^{-2} for 30 minutes). The polarization of BDD electrodes induces the stripping of sp^2 states, which are oxidized to CO_2. The comparison of graphite electrode (sp^2 carbon) with BDD anode (sp^3 carbon) permits to confirm this model.

Some work has already been made with other *outer sphere* systems (one of which is the VOH/VO· on glassy carbon [3, 4]) allowing a comparison of our results at BDD and GC electrodes. This study allowed us to determine key parameters such as the diffusion coefficient, D, the anodic transfer coefficient, α, and the standard electrochemical rate constant of the reaction investigated, k^0.

Violuric acid was also tested as a mediator for the indirect oxidation of 2-methoxyphenol, a recurrent function of lignin [5, 6].

2. EXPERIMENTAL

All the electrochemical measurements were performed in a 100 mL cell using different VOH concentrations in 0.1M acetate buffer (CH_3COONa/CH_3COOH, pH 4.65). Violuric and sulfuric acids were purchased in analytical grade from Fluka and the buffer was purchased from Riedel-de Haën. MilliQwater was used for the preparation of solutions.

Cyclic voltammetry, steady state polarization and rotating disk measurements were carried out in the conventional three-electrode cell described in Chapter 2.

Diamond and glassy carbon were used as working electrodes, $Hg/Hg_2SO_4,K_2SO_4$ (sat) electrode as the reference and a Pt wire as the counter-electrode. The exposed apparent area of both BDD and GC electrodes was 1 cm^2. The temperature was kept at 25°C.

The glassy carbon electrode was pretreated for some experiments. The pretreatment consisted in a polishing on a Grinder Polisher (Buehler Ltd, Coventry, UK) with emery paper (3M 734) followed by a polishing with alumina paste (Acryglas paste, Burnus, Ge).

3. RESULTS AND DISCUSSION

3.1. Electrochemical measurements for the redox couple VOH/VO·

The electrochemical behavior of the redox couple VOH/VO· was investigated by three electrochemical techniques using both boron-doped diamond (BDD) and glassy carbon (GC) electrodes.

3.1.1. Cyclic voltammetry

The first method used is the cyclic voltammetry (CV). CV is known as a transitory technique where potential is swept with time. By means of this technique and considering a quasi-reversible reaction (Equation 5.1), it is possible to investigate the dependence of the peak current with both the concentration and the scan rate, and to calculate the diffusion coefficient D_{VOH}. In that case, one can consider that the reaction is solely governed by the mass diffusion. From the same measurements, it is also possible to consider the irreversible system case (Equation 5.2 and Equation 5.3) to determine the anodic transfer coefficient α and the standard electrochemical rate constant k^0.

Boron doped diamond electrode

Figure 5.2 shows cyclic voltammograms recorded for five VOH concentrations (from 5 to 15 mM) at BDD electrode. The peak current increased with the violuric acid concentration. The dependence between the current peak and the concentration is linear as shown by the Figure 5.3.

Supposing a quasi-reversible system, the value of $2.8 \cdot 10^{-6}\, \mathrm{cm^2\, s^{-1}}$ was calculated for the diffusion coefficient D_{VOH} using the Equation 5.1 (Chapter 2):

$$i_p \ = \ (2.69 \times 10^{-5}) n^{3/2} A C_{VOH} D_{VOH}^{1/2} v^{1/2} \qquad \qquad 5.1$$

where i_p is the current peak (A), n is the number of electrons ($n = 1$), A is the electrode surface (m^2), C_{VOH} is the VOH concentration (mol m^{-3}), D_{VOH} is the diffusion coefficient of VOH (m^2 s^{-1}) and v is the scan rate (0.05 V s^{-1}).
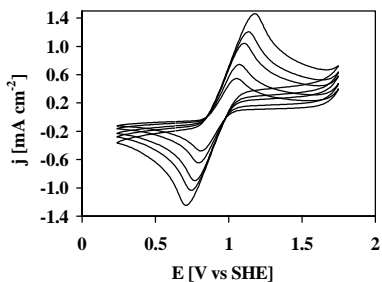
Figure 5.2 Cyclic voltammogram of redox couple VOH/VO· in 0.1 M acetate buffer (pH 4.65) at BDD electrode for different VOH concentrations: 5, 7, 10, 12, 15 mM. $v = 50$ mV s^{-1}, T = 25°C.
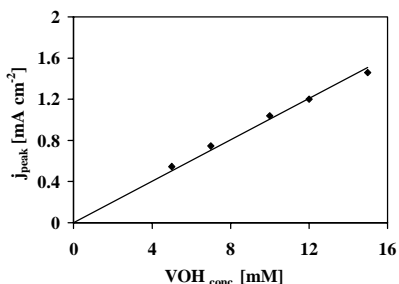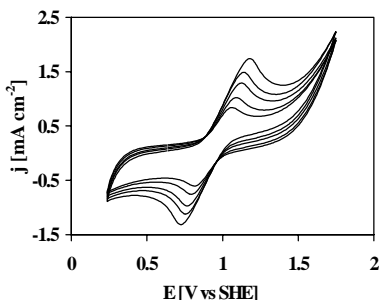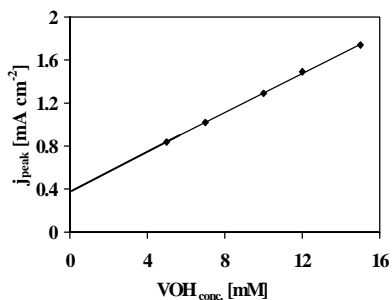
Figure 5.3 Dependence of the peak current density with the VOH concentration: 5, 7, 10, 12, 15 mM. $v = 50$ mV s^{-1}, T = 25°C.

The dependence between the current peak and the scan rate was also investigated at a fixed VOH concentration of 10 mM. Figure 5.4 represents the evolution of the cyclic voltammogram as a function of the scan rate. Figure 5.5 shows the linear relation found between the peak current and the square root of scan rate.

The value of $2.7 \cdot 10^{-6}$ cm^2 s^{-1} was calculated for the diffusion coefficient D_{VOH} using Equation 5.1.
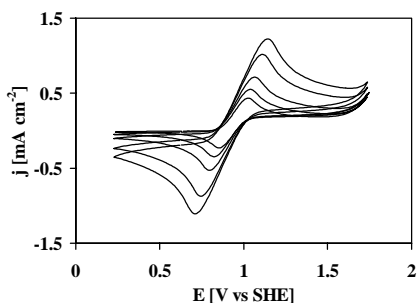
Figure 5.4 Cyclic voltammogram of a 10 mM solution of the redox couple VOH/VO· in 0.1 M acetate buffer (pH 4.65) at BDD electrode for different scan rate. $v = 5, 10, 20, 50, 80, 100, 150$ mV s^{-1}. T = 25°C.
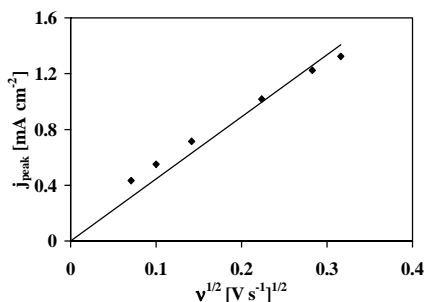
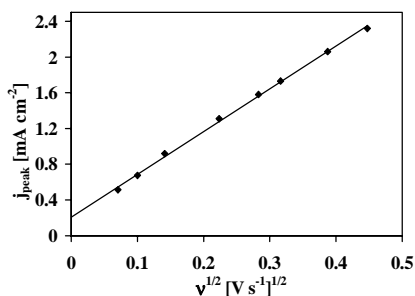**Figure 5.5** Dependence of current density with scan rate. $v = 5, 10, 20, 50, 80, 100, 150$ mV s^{-1}. T = 25°C.

The transfer coefficient α for the anodic reaction (Equation 5.2) and the reaction rate constant k^0 (Equation 5.3) were calculated with the following relations (Chapter 2):

$$\left|E_p - E_{p/2}\right| \;=\; 1.857\frac{RT}{\alpha F} \;=\; 47.7/\alpha \qquad\qquad 5.2$$

$$E_p \;=\; E^0 + \frac{RT}{\alpha nF}\left(0.78 - \ln k^0 + \ln\sqrt{D_O\frac{\alpha nF}{RT}}\right) - \frac{RT}{2\alpha F}\ln v \qquad 5.3$$

where E_p is the potential peak (V), $E_{p/2}$ is the half-peak potential (V), R is the gas constant (8.314 J mol^{-1} K^{-1}), T is the temperature (298.15 K), α is the anodic coefficient transfer, F is the Faraday's constant (96485 C mol^{-1}), n is the number of electron exchanged and k^0 is the standard electrochemical rate constant (m s^{-1}).

A value of 0.26 was found for the anodic transfer coefficient α and a standard electrochemical rate constant k^0 of $2 \cdot 10^{-7}$ m s^{-1} was calculated.

Glassy carbon electrode

For comparison, the same experiments were performed at GC electrode (dependence of j with both concentration and scan rate).

Figure 5.6 shows the cyclic voltammograms recorded at different VOH concentrations (from 5 to 15 mM) at GC electrode.

Figure 5.6 Cyclic voltammogram of redox couple VOH/VO$^{\bullet}$ in 0.1 M acetate buffer (pH 4.65) at GC electrode for different VOH concentrations: 5, 7, 10, 12, 15 mM. $v = 50$ mV s^{-1}, T = 25°C.

Figure 5.7 Dependence of current density with the VOH concentration: 5, 7, 10, 12, 15 mM. $v = 50$ mV s^{-1}, T = 25°C.

The peak current increased with the violuric acid concentration. Since the dependence of the current peak with the concentration is linear, j is not directly proportional with the concentration (meaning that the straight line does not pass through the origin), as expected for a quasi-reversible system (Figure 5.7).

The dependence between the current peak and the scan rate was also investigated at a fixed VOH concentration of 10 mM (Figure 5.8). As seen in the previous experiment, a linear relation exists between the peak current and the square root of scan rate (Figure 5.9). However, the peak current is not directly dependent on the square root of the scan rate. Indeed, the trendline does not come through the origin.
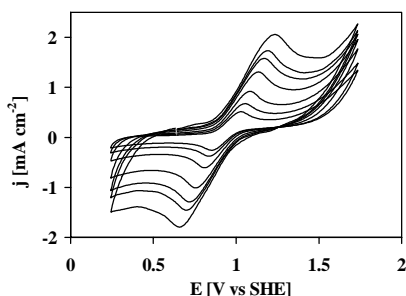
Figure 5.8 Cyclic voltammogram of 10 mM redox couple VOH/VO· in 0.1 M acetate buffer (pH 4.65) at GC electrode for different scan rate. ν = 5, 10, 20, 50, 80, 100, 150 mV s^{-1}. T = 25°C.

Figure 5.9 Dependence of current density with the scan rate. ν = 5, 10, 20, 50, 80, 100, 150 mV s^{-1}. T = 25°C.

As regards to these surprising results, a pretreatment of the glassy carbon electrode was performed in order to check if the surface had any influence on the reaction. The problem of removal of impurities at GC surface is often encountered in the literature [7, 8]. We have chosen a mechanical treatment consisting in polishing the GC surface with emery paper and alumina. Cyclic voltammograms were again recorded and the dependence between the peak current and the scan rate was investigated.

Figure 5.10 exhibits an expected pattern for the VOH/VO· redox couple at GC electrode (similar to the BDD response), meaning that the surface state has an important influence on the oxidation process. The mathematical treatment with Equation 5.1 was applied and a value of $1.91 \cdot 10^{-6}$ cm^2 s^{-1} was found for D_{VOH}.

From this experiment, the transfer coefficient α for the anodic reaction was calculated with Equation 5.2 ($\alpha = 0.4$) and the standard electrochemical rate constant k^0 was calculated with Equation 5.3 ($7.28 \cdot 10^{-7}$ m s^{-1}).
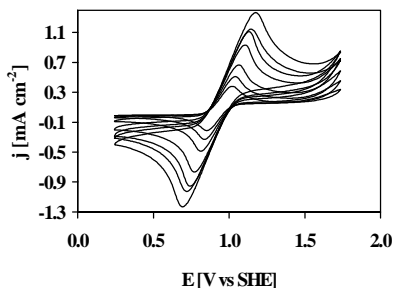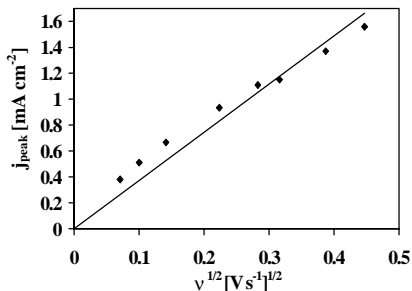

Figure 5.10 Cyclic voltammogram of 10 mM redox couple VOH/VO· in 0.1 M acetate buffer (pH 4.65) at polished GC electrode for different scan rate. $v = 5, 10, 20, 50, 80, 100, 150$ mV s^{-1}, T = 25°C.

Figure 5.11 Dependence of current density with the scan rate. $v = 5, 10, 20, 50, 80, 100, 150$ mV s^{-1}, T = 25°C.

Comparison and discussion

Table 5.1 summarizes the values obtained for the anodic transfer coefficient, the reaction rate constant and the diffusion coefficient determined by cyclic voltammetry.

	α	k^0 [m s^{-1}]	D_{VOH} [cm^2 s^{-1}]*	D_{VOH} [cm^2 s^{-1}]**
BDD	0.26	$1.45 \cdot 10^{-7}$	$2.7 \cdot 10^{-6}$	$2.8 \cdot 10^{-6}$
GC	0.4	$7.28 \cdot 10^{-7}$	$1.91 \cdot 10^{-6}$	-

Table 5.1 *Diffusion and kinetics parameters of BDD and GC electrodes.*

* calculated from the scan rate-peak current dependence

** calculated from the concentration-peak current dependence

Concerning the diffusion coefficient of VOH, the literature gives a value of $2 \cdot 10^{-6}$ cm^2 s^{-1} [4]. The values determined for GC and BDD electrodes, as well by the variation

of the concentration as that of the scan rate, are in agreement with this reference.

The transfer coefficient α is higher for BDD than for GC electrode. Generally, one can consider that for a metal, α is theoretically equal to 0.5 ($\alpha + \beta =1$) [9]. Consequently, the value of 0.4 for glassy carbon is expected, since this material exhibits a metallic character. The lower value for BDD ($\alpha = 0.26$) can be explained if we consider the semi-conductor character of diamond.

The results concerning the reaction rate constants will be discussed in the following paragraph by comparison with the values calculated by steady state polarization.

3.1.2. Steady-state polarization curves

The second method used is the steady state polarization (low field approximation), which is a stationary technique. The polarization at low overvoltage permits to eliminate the mass transfer contribution.

The kinetic parameter k^0 of the electrochemical reaction was calculated by recording the steady-state polarization curves at four concentrations of VOH (from 5 to 15 mM) at 0.1 mV s^{-1}.

The same experiments were performed at both diamond and glassy carbon electrode.
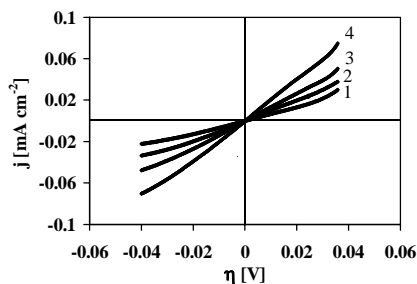
Boron doped diamond electrode
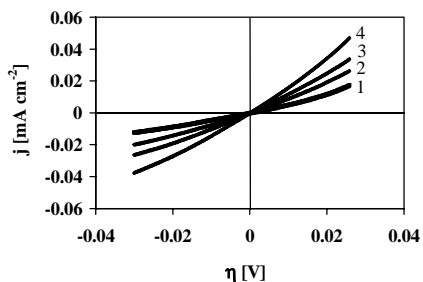
Figure 5.12 Polarization curves of the redox couple VOH/VO⋅ in acetate buffer (pH 4.65) at BDD electrode for different VOH concentrations: 1) 5, 2) 7, 3) 12, 4) 15 mM. $\nu = 0.1$ mV s^{-1}, T = 25°C.

The steady-state curves were fitted to straight lines, whose slopes increased with the

violuric acid concentration. The standard reaction rate constant k^0 was calculated from the following relations (Equation 5.4 and Equation 5.5), corresponding to the low overpotential approximation ($\eta < 10mV$) of the Butler-Volmer equation:

$$j = j_0 \frac{F}{RT}\eta \qquad\qquad 5.4$$

$$k^0 = \frac{j_0}{FC} \qquad\qquad 5.5$$

As explained in Chapter 2, equations are valid only if we consider that the sum of both anodic (α) and cathodic (β) transfer coefficient $\alpha+\beta$ is equal to 1 and that the concentrations of both reduced and oxidized species are equal. In the case of violuric acid, only VOH is present in the solution and $\alpha+\beta$ is not equal to one.

Still, these relations were used to estimate the standard electrochemical rate constant and a value of $2.07 \cdot 10^{-7}$ m s^{-1} was calculated for k^0 at BDD electrode.

Glassy carbon electrode

The same measurements were also carried out for GC electrode as shown in Figure 5.13:

Figure 5.13 Polarization curves of the redox couple VOH/VO$^\cdot$ in acetate buffer (pH 4.65) at GC electrode for different VOH concentrations: 1) 5, 2) 7, 3) 12, 4) 15 mM. $v = 0.1$ mV s^{-1}, T = 25°C.

The steady-state curves were fitted to straight lines. As shown previously, the slopes increased with the violuric acid concentration. A standard electrochemical rate constant

k^0 of $3.61 \cdot 10^{-7}$ m s^{-1} was calculated from Equation 5.4 and Equation 5.5, corresponding to the low field approximation ($\eta < 10$ mV) of the Butler-Volmer equation.

Comparison and discussion

Standard electrochemical rate constants have in both cases (diamond and glassy carbon) the same order of magnitude (10^{-7} m s^{-1}). Similar values for other *outer sphere* redox couples using BDD were found [10], confirming the validity of the measurement. A much higher value was expected for GC because of the increase of sp^2 carbon at the surface electrode. Our results can be explained by a different quality surface state leading to a slow electron transfer process. Indeed, we have observed for cyclic voltammetry that the surface can strongly influence the electrode process.

3.1.3. Rotating disk electrode

The last electrochemical technique is an hydrodynamic one. This method deals with both the mass transfer and the charge transfer (mixed kinetics). Rotating disk electrode method (RDE) allows to reach quickly the stationary state and permits to determine the diffusion coefficient of VOH (D_{VOH}) using the Levich equation. By extrapolation, it is also possible to calculate the standard reaction rate constant k^0. The RDE theory was developed in Chapter 2.

Boron doped diamond electrode

Figure 5.14 represents the polarization curves obtained for different rotation rates (from 100 to 1000 rpm). From these measurements, it is possible to study the dependence between the limiting current density (j_{lim}) and the rotation rate (ω). The relation between j_{lim} and the square root of the rotation rate is linear as expected (Figure 5.15). A value for the diffusion coefficient D_{VOH} of $5.47 \cdot 10^{-6}$ cm^2 s^{-1} was calculated using the Levich equation (Equation 5.6).

$$j_{lim} = 0.62 nF D_{VOH}^{2/3} \omega^{1/2} \nu^{-1/6} C_{VOH}^{*} \qquad\qquad 5.6$$

where ω is the rotation rate (s^{-1}) and the other units are the same as for Equation 5.1.

Considering the equilibrium potential, by extrapolation, it is possible to calculate k^0 using Equation 5.7:

$$\frac{1}{j} = \frac{1}{j_K} + \frac{1}{j_{lim}} = \frac{1}{j_K} + \frac{1}{0.62nFD^{2/3}\omega^{1/2}v^{-1/6}C_o^{*}} \qquad 5.7$$
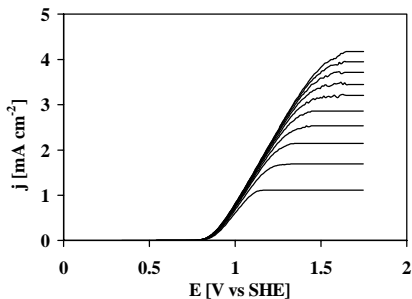

Figure 5.14 Scans using BDD rotating disk electrode at different rotation rates (from 100 to 1000 rpm) for a 10 mM VOH solution in acetate buffer (pH 4.65). $v = 1$ mV s^{-1}, T = 25°C.
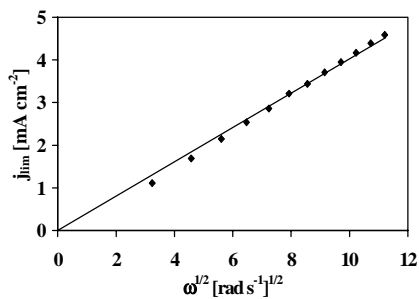
Figure 5.15 Dependence of the limiting current density with the square root of the rotation rate (100 to 1000 rpm) for a 10 mM VOH solution in acetate buffer (pH 4.65). $v = 1$ mV s^{-1}, T = 25°C.
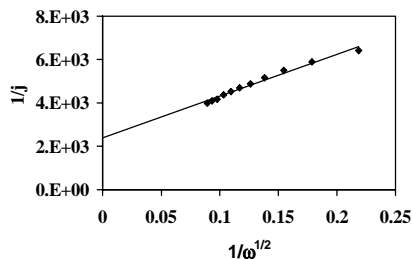
**Figure 5.16** Graphical representation of Equation 5.7 at BDD electrode for the determination of $1/j_k$ at 0.9 V vs SHE.

According to Equation 5.7, the intercept of the trend line allows to calculate j_k, which is equal to $4.2 \cdot 10^{-4}$ A cm^{-2}. j_k represents the current in absence of mass transfer. From this

value, it is possible to calculate the reaction rate constant for the charge transfer k_f according to the following relation:

$$j_k = nFAk_f C_{VOH}^{*}$$ 5.8

where k_f is the heterogeneous rate constant (m s^{-1}) at a given potential.

This calculation was made at different potential (close to the equilibrium one): 0.95, 1.05 and 1.1 V vs SHE.

According to Equation 5.9:

$$k_f = k^0 \exp\left(\frac{-\alpha nF(E - E^{0'})}{RT}\right)$$ 5.9

where $E^{0'}$ is defined as the potential where reduction and oxidation rate constants are equal and considering the graphical representation of $ln\ k_f$ as a function of $(E - E^{0'})$, it is possible to calculate k^0 (Figure 5.17).
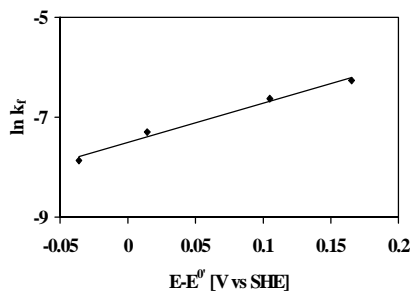
Figure 5.17 Graphical representation of Equation 5.9 at BDD electrode for the determination of k^0.

The value of $5.5 \cdot 10^{-6}$ m s^{-1} was found for k^0 at BDD electrode.

Glassy carbon electrode

Figure 5.18 represents the scans obtained for different rotation rates (from 100 to 1000 rpm) for glassy carbon electrode.

.
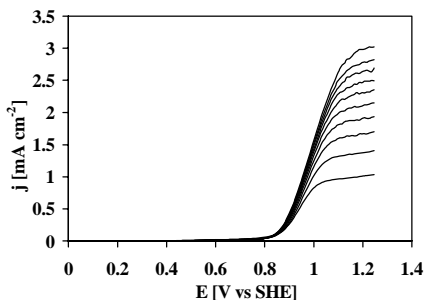
Figure 5.18 Scans using GC rotating disk electrode at different rotation rates (from 100 to 1000 rpm) for a 10 mM VOH solution in acetate buffer (pH 4.65). $v = 1$ mV s^{-1}, T = 25°C.
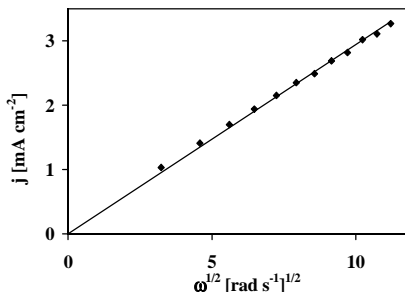
Figure 5.19 Dependence of the limiting current density with the square root of the rotation rate (100 to 1000 rpm) for a 10 mM VOH solution in acetate buffer (pH 4.65). $v = 1$ mV s^{-1}, T = 25°C.

The dependence of the limiting current density with the square root of the rotation rate is linear (Figure 5.19). A diffusion coefficient D_{VOH} of $3.55 \cdot 10^{-6}$ cm^2 s^{-1} was calculated using the Levich equation (Equation 5.6).

As seen previously, it is possible to calculate k_f using Equation 5.7.
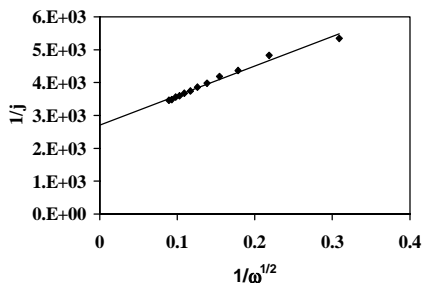
Figure 5.20 Graphical representation of Equation 5.7 at GC electrode for the determination of $1/j_k$ at 0.9 V vs SHE.

According to the intercept of the straight line of Figure 5.20 and Equation 5.7, j_k is calculated. According to Equation 5.8, k_f was calculated at different potentials (0.87, 0.93 and 0.96 V vs SHE). According to Equation 5.9 and Figure 5.21, the calculation of k^0 was

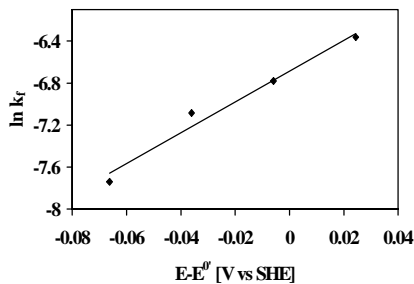made and a value of $1.25 \cdot 10^{-5}$ m s^{-1} was found.

Figure 5.21 Graphical representation of Equation 5.9 at GC electrode for the determination of k^0.

Comparison and discussion

The diffusion coefficient values calculated using rotating disk electrode are, in both cases, in harmony with the results obtained by cyclic voltammetry and with the literature values. However, the standard rate constant for both BDD and GC electrodes are higher than the values determined by low field approximation. It is necessary to take in consideration that the k^0 values were determined by extrapolation that is less precise.

3.2. Indirect in-cell electrochemical oxidation using VOH

The redox couple VOH/VO$^{\cdot}$ was tested as mediator using BDD electrode. The aim is to use the redox couple as a mediator (catalyst) between the diamond electrode and an organic compound. The oxidized form is generated at the anode to allow the oxidation of the organic. Then, the reduced form returns to the anode as shown in Figure 5.22.
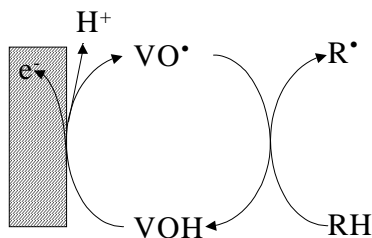
Figure 5.22 Scheme of the indirect oxidation via a mediator.

2-methoxyphenol (called guaiacol) was tested because it is a recurrent function of lignin (compound involved in pulp). The cyclic voltammetry was performed with a mixture of guaiacol and VOH (Figure 5.23).
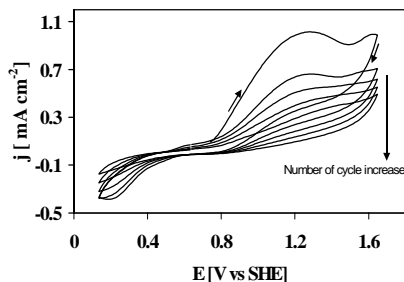

Figure 5.23 Successive cyclic voltammograms of 10 mM VA solution in 0.1 M acetate buffer (pH 4.65) and 5 mM of guaiacol at BDD electrode. $\nu = 50$ mV s^{-1}. T = 25°C.

The current density peak decreases with the number of cycles. This behavior is characteristic of the deactivation of the electrode surface. This deactivation is due to the formation of polymeric guaiacol forms deposed at the surface electrode as shown in Figure 5.24:
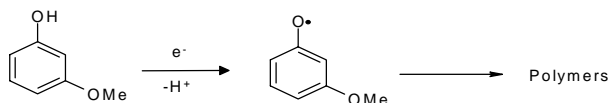
Figure 5.24 Mechanism of the oxidation of the 2-methoxyphenol.

4. CONCLUSIONS

The following table summarizes all the results calculated by the three different electrochemical techniques:

		Cyclic Voltammetry		Steady state polarization	RDE
		vs $\nu^{1/2}$	vs C		
k^0	BDD	$1.45 \cdot 10^{-7}$		$2.07 \cdot 10^{-7}$	$3 \cdot 10^{-6}$
m s^{-1}	GC	$7.28 \cdot 10^{-7}$		$3.61 \cdot 10^{-7}$	$1.25 \cdot 10^{-5}$
D_{VOH}	BDD	$2.7 \cdot 10^{-6}$	$2.8 \cdot 10^{-6}$		$5.47 \cdot 10^{-6}$
cm^2 s^{-1}	GC	$1.91 \cdot 10^{-6}$	-		$3.55 \cdot 10^{-6}$
α	BDD	0.26			
	GC	0.4			

Table 5.2 Summary of the electrochemical parameters calculated for BDD and GC electrodes.

The use of three techniques allowed us to compare the results and the validity of each method for the system studied. In spite of the different electrochemical approaches between the three techniques (stagnant solution for the cyclic voltammetry and forced convection for the rotating disk electrode), the values obtained for the diffusion coefficients are almost equal. The values obtained by cyclic voltammetry for both boron-doped diamond and glassy carbon electrodes are closer to the literature than that determined by rotating disk electrode.

Transitory and stationary regimes were approached by cyclic voltammetry and steady state polarization, respectively. These approaches gave similar values for the reaction rate constant k^0 in spite of the approximations made for the treatment of the results (especially for the steady polarization, $\alpha + \beta = 1$ and $C_{VOH} = C_{VO\bullet}$). The reaction at GC electrode is slightly more rapid than at BDD anode. However, the redox couple does not seem to be very sensitive to the presence of a higher concentration of sp^2 carbon.

This observation is in agreement with the properties of an *outer sphere* system, which implies weak interactions between the diamond electrode and the reactant. Usually, the reaction kinetics do not depend on the electrode surface. Therefore, the determined values are expected to be similar for both electrodes. However, differences can be explain even in the case of an *outer sphere* system, by the influence of the electrode material on the kinetics by affecting the electric layer and the Helmotz layer structure.

Compared to the widely investigated *outer sphere* reactions like ferri-ferro cyanide, only the reduced form of violuric acid (VOH) is present in our system and no control is possible on the concentration of the oxidized form (VO˙). Then, some approximations have been made for Equation 5.4 and Equation 5.5, as well as for the calculation of k^0 by steady state polarization.

Finally, the values of the transfer coefficient α seem to be consistent with the theory. Due to the metallic character of the GC electrode, a value close to 0.5 is indeed expected. Concerning the diamond anode, a value of 0.26 was found. It is assumed that for an ideal semi-conductor, the transfer coefficient should α should be equal to 0. But, this case is rare and the value of 0.26 can be assigned to the partial localization of the interfacial potential drop in the Helmotz layer upon the electrode polarization [10, 11].

The interesting point of this investigation is that we obtained similar parameters in spite of the use of three different techniques that deal with different mode transport (mass transport by diffusion for cyclic voltammetry, by convection for rotating disk electrode and charge transfer for steady state polarization).

The use of violuric acid as a mediator seems to be difficult for an indirect in-cell reaction occurring in the potential region of water stability. It will probably be more interesting to test a compound that cannot polymerize in order to avoid the polymerization of organics at the BDD surface.

5. REFERENCES

[1]   J.C. Angus, Y.V. Pleskov, and S.C. Eaton, *Electrochemistry of Diamond*, in *Thin-Film Diamond II*, Elsevier, Editor. 2004.

[2]   J. Ristein, *Structural and Electronic Properties of Diamond Surfaces*, in *Thin-Film Diamond II*, Elsevier, Editor. 2004.

[3]   H.-C. Kim, M. Mickel, S. Bartling, and N. Hampp, *Electrochim. Acta*, **47** (2001)

799.

[4]   K. Krikstopaitis and J. Kulys, *Electrochem. Commun.*, **2** (2000) 119.

[5]   C. Oloman, *Electrochemical Processing for the Pulp and Paper Industry*, 1996, The Electrochemical Consultancy, Hants.

[6]   V.O. Sippola and A.O.I. Krause, *J. Mol. Cat. A: Chem.*, **3816** (2002) 1.

[7]   G.K. Kiema, M. Aktay, and M.T. McDermott, *J. Electroanal. Chem.*, **540** (2003) 7.

[8]   R.L. McCreery, *Electrochemical properties of carbon surfaces*, A. Wieckowski.

[9]   Y.V. Pleskov, *Russ. Chem. Rev.*, **68** (5) (1999) 381.

[10]   I. Duo, *Control of electron transfer kinetics at boron-doped diamond electrodes by specific surface modification*, *Thesis N° 2732*. 2003, EPFL, Lausanne.

[11]   Y.E. Evstefeeva, Y.V. Pleskov, V.P. Varnin, and I.G. Teremetskaya, *Russ. J. Electrochem.*, **34** (2) (1998) 234.

Chapter 6. Detection of electrogenerated hydroxyl radicals at BDD anode

1. INTRODUCTION

BDD electrodes are known to be typical *non active* electrodes. This designation means that the electrochemical oxygen transfer reaction is mediated by hydroxyl radicals that are weakly adsorbed at the electrode surface. Consequently, the surface of the electrode does not participate in the anodic process. In order to validate this hypothesis, it is necessary to detect the presence of hydroxyl radicals during electrochemical reactions at diamond electrode.

Free hydroxyl radicals are very reactive species and have a short life time of about 10^{-9} s. These characteristics explain the difficulty to detect the radicals *in situ* (even if it is theoretically possible with spin resonance measurements). Therefore, the spin trapping represents an easier alternative to detect and identify this radical. The principle of spin trapping method is to produce a stable adduct by allowing a specific scavenger to react with a less stable radical.

Since hydroxyl radicals are supposed to be the electrogenerated intermediates

responsible for the oxidation process at boron-doped diamond, their presence was investigated at BDD electrode. The detection was made by spin trapping to allow the formation of a stable adduct, which is detectable by analytical methods. Two different experiments were performed at boron-doped diamond electrode using two different spin traps (5,5-dimethyl-1-pyrroline-N-oxide noted DMPO and 4-nitroso-N,N-dimethylaniline called *p*-nitrosoaniline or RNO) and two different analysis techniques (Electron Spin Resonance *ESR* and *UV*-visible measurement, respectively). In the case of the *ESR* analysis, a comparison with hydroxyl radicals chemically produced by Fenton reaction was also investigated to confirm the results.

As an other proof of the presence of hydroxyl radicals, the formation of hydrogen peroxide (electrogenerated intermediate) as well as the study of competitive reactions between hydroxyl radicals and carboxylic acids (oxalic and formic acids), were also investigated.

Finally, the reactivity of hydroxyl radicals at BDD anode was investigated through the hydroxylation reaction of salicylic acid. The hydroxylation of this organic is known to produce three well identified hydroxylated products: 2,3- and 2,5-dihydroxylated benzoic acid and catechol (with a concomitant decarboxylation). The electrochemical hydroxylation was carried out at BDD anode. In order to compare the reaction and the intermediates distribution, the chemical hydroxylation was also performed by Fenton reaction and *UV*-photolysis.

2. EXPERIMENTAL

2.1. Spin trapping

2.1.1. Electrolysis of DMPO and Electron Spin Resonance measurement

The electrolysis of an 8.8 mM DMPO solution in 1M perchloric acid was carried out with the electrochemical cell described in Chapter 4. Diamond was used as the working electrode and a Pt wire as counter electrode.

ESR spectra were recorded on a Brucker ECS 080 X-band spectrometer (Brucker). The measurements were performed at ambient temperature (298 K) with the following conditions: 100 kHz modulation with 1.5 G application, 10 mW microwave power, 3350 G central magnetic field and 100 G scan width. The Fenton solution used for comparison

was a mixture of 10 mM DMPO, 1M H_2O_2 and 10 mM $(NH_4)_2Fe(SO_4)_2$. All the products were purchased from Fluka.

2.1.2. Electrolysis of RNO and UV-visible measurement

The electrolysis of a 3.12 mM *p*-nitrosoaniline (RNO) yellow solution was carried out at pH 9.5 in 0.1 M borax solution $(Na_2B_4O_7)$ using the electrochemical characterization cell as described for the electrochemical measurements (Chapter 4). A sample was removed at steady time. The absorbance was recorded at ambient temperature (298 K) on a Shimadzu spectrophotometer UV-160A between 340 and 550 nm.

In the conditions of the experiment, the maximum of absorbance is found at 440 nm. The molar extinction coefficient ε was calculated from the Beer-Lambert relation ($A = \varepsilon.l.c$ with $l = 1$ cm). The obtained value for ε was $3 \cdot 10^4$ L mol^{-1} cm^{-1} (reference value $3.35 \cdot 10^4$ L mol^{-1} cm^{-1} [1]). The total organic carbon (*TOC*) of the solution was measured using a TOC-5050 Shimadzu (Shimadzu Corporation, Tokyo, Japan).

2.2. Formation of H_2O_2

The formation of hydrogen peroxide was investigated by electrolysis in the two-compartments electrochemical flow cell. Anolyte and catholyte were 1M perchloric acid solutions and were stored in two 500 mL thermoregulated tanks (T = 25°C). They were circulated through the electrolytic cell by centrifugal pumps.

2.3. Competitive reaction

The electrolysis was performed in the two-compartments electrochemical flow cell under galvanostatic conditions (Chapter 4). The anolyte was a 500 mL solution of 0.5 M formic acid and 0.5 M oxalic acids in 1 M perchloric acid. The catholyte was a 500 mL solution of 1M perchloric acid. The electrolysis was performed at 23.8 mA cm^{-2}. The concentrations of carboxylic acids were monitored by *HPLC* on a Shimadzu LC-6 Series (Shimadzu Corporation, Tokyo, Japan) with a Supelcogel C610-H column. The mobile phase was water-H_3PO_4 0.1% at a flow rate of 0.5 mL min^{-1} and the wavelength used was 210 nm. The retention time for formic and oxalic acids were 18.06 min and 8.67 min, respectively. The total organic carbon of the solution was measured using a TOC-5050 Shimadzu.

2.4. Hydroxylation of salicylic acid

Electrochemical hydroxylation

The electrochemical hydroxylation of salicylic acid (SA) was carried out using the two-compartments electrochemical flow cell described in Chapter 4. The anolyte was a solution of 7.25 mM SA in 1 M $HClO_4$ and the catholyte was 500 mL of 1 M $HClO_4$. The temperature was kept at 15°C. The concentrations of salicylic and hydroxylated intermediates were monitored on a Shimadzu LC-2010A (Shimadzu Corporation, Tokyo, Japan), using an apolar reversed phase Nucleosil 7 C8 column with a mobile phase of water-1% H_3PO_4/acetonitrile 80/20. Retention times are given in Table 6.1. The isocratic flow rate was 0.5 mL min^{-1}. The detection was performed at a wavelength λ of 294 nm.

Compounds	Formula	C8 column Retention time [min]
Salicylic acid	$C_7H_6O_3$	13.69
2,3-DHBA	$C_7H_6O_4$	7.18
2,5-DHBA	$C_7H_6O_4$	6.42

Table 6.1 Structure and retention times of detected intermediates.

Fenton reagent (H_2O_2-Fe^{2+})

Fenton reaction was performed by adding 0.1 mL of a 0.6 M Fe(II) solution to 100 mL of a 7.25 mM SA solution in 1M $NaClO_4$ followed by the addition of a solution of 3% H_2O_2. The pH of the solution was kept to 4.4 with acetate buffer (CH_3COONa/ CH_3COOH). The reaction was performed in a thermoregulated cell and the solution was allowed to react with a medium stirring. The Fenton reaction started when H_2O_2 was added. Each 20 minutes (corresponding to the *HPLC* analysis time), a sample of 1 mL was taken and immediately cooled on ice to stop the reaction.

According to the Fenton equation:

$$Fe^{2+} + H_2O_2 \rightarrow Fe^{3+} + HO^{\bullet} + HO^{-} \qquad\qquad 6.1$$
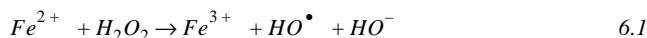
and considering that the total combustion of SA needs 14 mol of H_2O_2:

$$C_7H_6O_3 + 14H_2O_2 \rightarrow 7CO_2 + 17H_2O, \qquad\qquad 6.2$$
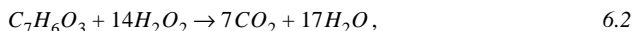
it is possible to control the production of hydroxyl radicals by changing the ratio (r) between the moles of SA and hydrogen peroxide. Therefore, the volume of added hydrogen peroxide depends on the ratio investigated. The analysis of samples were monitored on a Shimadzu LC-2010A (Shimadzu Corporation, Tokyo, Japan), using a Nucleosil 7 C8 column with a mobile phase of water-1% H_3PO_4 /acetonitrile 80/20. The isocratic flow rate was 0.5 mL min^{-1}. The detection was performed at a wavelength of 294 nm.

UV photolysis (H_2O_2-UV)

The experiments were conducted in a cylindrical cell of 100 mL containing a 7.25 mM SA solution in 1M NaClO$_4$ and 10 mL of 3% H_2O_2. The pH was kept to 4.4 with acetate buffer (CH$_3$COONa/CH$_3$COOH). The irradiation source was a 6 W photochemical reactor with a 250 W mercury light (Photochemical reactor Ltd.). Samples were taken at regular time and analyzed by *HPLC* with a Shimadzu LC-2010A (Shimadzu Corporation, Tokyo, Japan), using a Nucleosil 7 C8 column with a mobile phase of water-1% H_3PO_4 /acetonitrile 80/20. The isocratic flow rate was 0.5 mL min^{-1}. Detection was performed at a wavelength of 294 nm.

Selectivity and conversion

The selectivity of the hydroxylated intermediates (*S*) relative to the amount of salicylic acid converted and the conversion (*X*) of salicylic acid, 2,3- or 2,5-dihydroxylated benzoic acids have been defined as:

$$S = \frac{[DHBA]_t - [DHBA]_0}{[SA]_0 - [SA]_t} \times 100 \qquad\qquad 6.3$$

$$X = \frac{[R]_0 - [R]}{[R]_0} \times 100 \qquad\qquad 6.4$$

where $[DHBA]_0$ and $[DHBA]_t$ are the concentrations of 2,3- or 2,5-dihydroxylated acids

at time 0 and t, respectively (mol m^{-3}) and $[R]_0$ and $[R]_t$ are the concentrations of SA, 2,3- or 2,5-DHBA at time 0 and t, respectively (mol m^{-3}).

3. RESULTS AND DISCUSSION

3.1. *ESR* measurements with DMPO

The spin trap DMPO reacts with hydroxyl radicals to produce a stable adduct as shown in Figure 6.1. The main advantage of using DMPO is that it exhibits different spectra with hydroxyl radical and singlet oxygen. The rate constant between DMPO and hydroxyl radicals is equal to $4.3 \cdot 10^9$ M^{-1} s^{-1} [2].
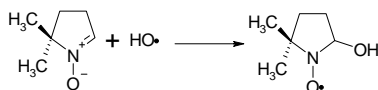
Figure 6.1 Reaction scheme of spin trapping between hydroxyl radicals and DMPO.

The electrolysis of an 8.8 mM DMPO solution in perchloric acid was performed at BDD electrode at a current density of 0.1 mA cm^{-2} for 2 hours.
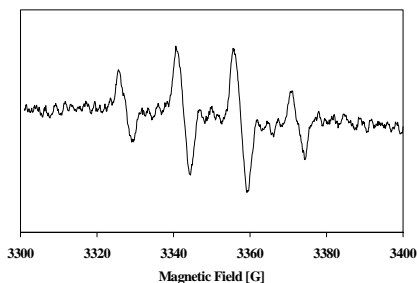
Figure 6.2 *ESR* spectrum of the DMPO-OH adduct obtained after electrolysis for 2 hours at BDD electrode. $j = 0.1$ mA cm^{-2}, T = 25°C.
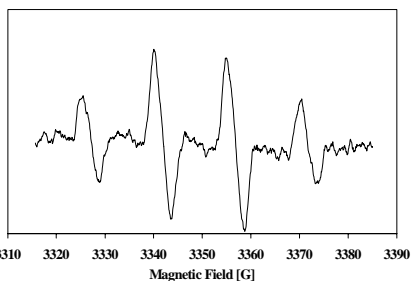
Figure 6.3 *ESR* spectrum of the DMPO-OH adduct obtained by Fenton reaction. T = 25°C.

Figure 6.2 shows the *ESR* spectrum obtained after 2 hours of electrolysis. The

spectrum exhibits four non-equivalents peaks meaning the presence of two different species. The interaction takes place between N (I = 1) and H (I = 1/2). The hyperfine splitting couplings were calculated with a fitting program (Program NMRICMA). The hyperfine couplings a_N and a_H were equal to 14.95 G. In order to compare the electrochemical production of hydroxyl radicals with the chemical one, a typical Fenton reaction was carried out. The solution was allowed to react for 60 minutes. The obtained spectrum is shown in Figure 6.3 and is similar to the one obtained with the electrolysis, showing 4 non-equivalents peaks. The fitting of the spectrum gave $a_N = a_H = 15.20$ G.

These values are typical of the spin-adduct DMPO-OH, (15 G [3, 4]). These results indicate that hydroxyl radicals are produced at boron-doped diamond and by Fenton reaction.

The same experiments were performed with an other spin trap, N-tert-butyl-α-phenylnitrone (PBN). The reaction with hydroxyl radicals is shown in Figure 6.4 [5].
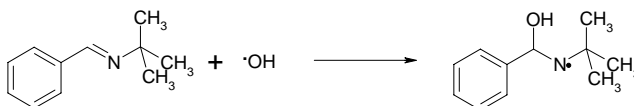
Figure 6.4 Reaction scheme of spin trapping between hydroxyl radicals and PBN.

A Fenton reaction was performed in order to obtain the PBN-OH adduct. Figure 6.5 shows the recorded spectrum.
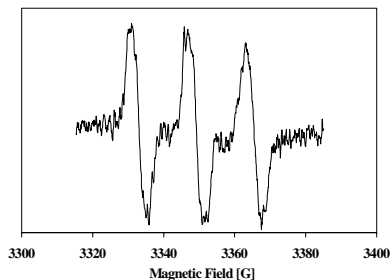
Figure 6.5 *ESR* spectrum of the PBN-OH adduct obtained by Fenton reaction.
T = 25°C.

The spectrum exhibits three equivalents peaks assigned to N (I = 1). The hyperfine splitting coupling was calculated by the software NMRICMA as $a_N = 15$ G. This value is in agreement with the typical value of PBN-OH adduct (15.3 G [3]). However, the sensitivity of the device did not allow to detect the hydrogen coupling, which is generally equal to 2.75 G. Unfortunately, when the electrochemical production of hydroxyl radicals was carried out no clear signal was found by *ESR*.

3.2. UV-Visible measurements with RNO

The reaction between hydroxyl radicals and *p*-nitroso-dimethylaniline (RNO) is shown in Figure 6.6:
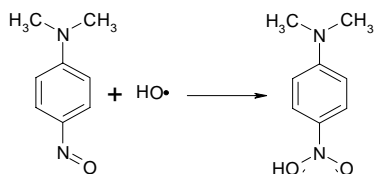
Figure 6.6 Reaction scheme of spin trapping between hydroxyl radicals and RNO.

The use of *p*-nitrosoaniline as a spin trap is interesting because RNO is, under these conditions of concentration and pH, electrochemically inactive. The reaction occurs at a very high rate constant ($1.3 \cdot 10^{10}$ M^{-1} s^{-1} [6]) and, moreover, is very selective.

The electrolysis of a RNO solution in borax medium was carried out at a current density of 0.4 mA cm^{-2}. Each 30 minutes, a sample was taken to record the absorbance and the *TOC* of the solution.
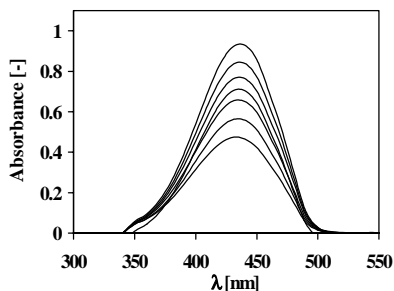
Figure 6.7 Evolution of the absorbance of a 3.1 10^{-3} M RNO solution in 0.1 M borax. Curves were recorded each 30 minutes. $j = 20$ mA cm^{-2}, T = 25°C.
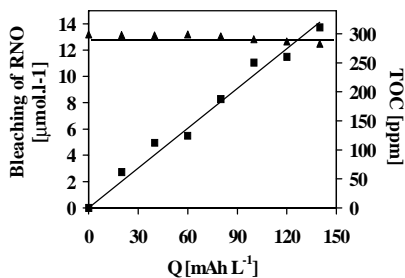
Figure 6.8 (■)Bleaching and (▲)TOC evolution of 3.1 10^{-3} M RNO solution in 0.1 M borax medium as a function of the specific charge. $j = 20$ mA cm^{-2}, T = 25°C.

Figure 6.7 shows the evolution of the absorbance spectra during the electrolysis of the RNO solution. The maximum of absorbance decreases linearly with the specific charge (or time) as presented in Figure 6.8. This behavior indicates that a direct reaction between hydroxyl radicals and the spin trap RNO takes place. In all cases, the maximum absorbance is found at 440 nm as expected. In order to check the selectivity of the reaction (if the decrease of the RNO can exclusively be assigned to the reaction between hydroxyl radicals and spin trap), the *TOC* was measured.

Figure 6.8 also represents the evolution of the total organic carbon during the electrolysis. The *TOC* remains constant as a function of the passed charge, indicating that no reaction other than the direct reaction between hydroxyl radicals and RNO occurs. The removal of RNO is representative of the formation of hydroxyl radicals and not of the RNO oxidation by an other oxidant. These results indicate that the formation of hydroxyl radicals takes place, confirming the role of BDD electrode as *non active* anode.

3.3. Hydrogen peroxide formation

The investigation was focused on the formation of hydrogen peroxide. Hydrogen peroxide is a strong oxidant (standard potential 1.8 V vs *SHE* at pH = 0 [7]). The formation of H_2O_2 can be due to the water oxidation either by a direct mechanism (Equation 6.5) or by an indirect mechanism (Equation 6.6). The latter case means that two

electrogenerated hydroxyl radicals react together.

$$2H_2O \rightarrow H_2O_2 + 2H^+ + 2e^- \qquad\qquad 6.5$$

$$2HO^\bullet \rightarrow H_2O_2 \qquad\qquad 6.6$$

The production of H_2O_2 is not caused by the reaction between ozone and water because of the slow kinetics of the reaction at very low pH. The oxidation of a 1 M perchloric acid solution was carried out at different current densities (from 230 to 1600 A m^{-2}), at 25°C. The produced H_2O_2 was measured out by permanganate titration (Figure 6.9).
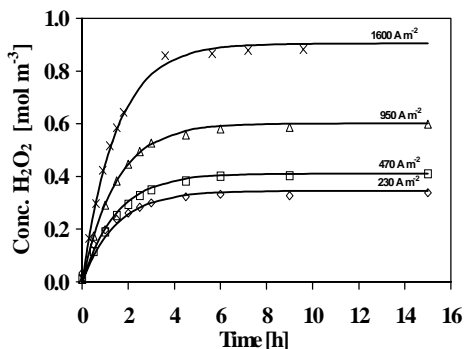

Figure 6.9 Evolution of hydrogen peroxide concentration with time at different current densities. 1 M $HClO_4$ solution, T = 25°C.

The high concentrations of hydrogen peroxide observed allowed us to conclude that a low adsorption of species at BDD (contrary to other electrode materials as Pt, SnO_2, PbO_2) takes place and that the first steps of oxygen evolution are the formation of hydroxyl radicals followed by their combination into H_2O_2. After approximately 4 hours, the concentrations reached a saturation due to oxidation.

3.4. Competitive reaction

This study highlights the presence of hydroxyl radicals by the investigation of the competition between hydroxyl radicals and carboxylic acids. When a mixture of organic

compounds is present in solution, one can consider that they are competition with the hydroxyl radicals produced during water discharge. In order to investigate this competition, the electrolysis of a formic and oxalic acids mixture was carried out.

Figure 6.10 represents the effect of formic and oxalic acids on the oxygen evolution curve in perchloric acid.
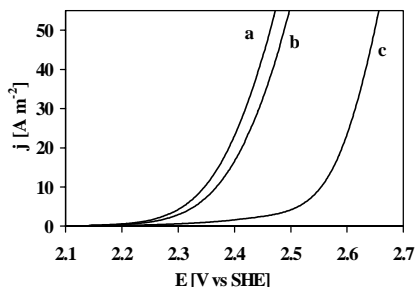

Figure 6.10 Shift of the oxygen evolution curve of (c) perchloric acid 1 M solution in presence of (a) 0.1 M formic acid and (b) 0.1 M oxalic acid, $v = 20$ m s^{-1}, T = 25°C.
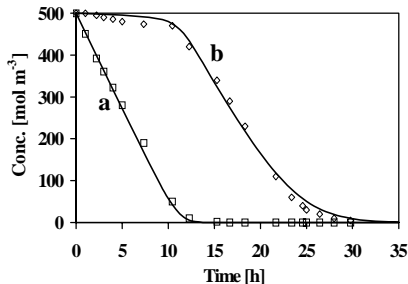
Figure 6.11 Evolution of concentrations with time during the oxidation of a mixture of (a) formic and (b) oxalic acids in perchloric acid medium. $j = 238$ A m^{-2}, T = 25°C.

The shift of the water decomposition potential indicates that the oxidation pathway involves electrogenerated hydroxyl radicals. An higher activity of BDD toward formic acid than oxalic acid is observed. Indeed, at a given potential, the current density of formic acid oxidation is higher than the one of oxalic acid. In order to understand better this difference of reactivity, the electrolysis of a mixture of formic and oxalic acids in perchloric acid was carried out at 238 A m^{-2}. The concentrations were determined by *HPLC* and their evolution are shown in Figure 6.11. The oxidation of formic acid started at the beginning of the electrolysis while the concentration of oxalic acid remained unchanged. After approximately 12 hours, the oxidation of formic acid was limited by the mass transport and the oxidation of oxalic acid started. This behavior can be explained taking into consideration that both formic and oxalic acids are in competition with hydroxyl radicals. Moreover, the rate constants between hydroxyl radicals and formic acid ($k = 10^8$ M^{-1} s^{-1}) is higher by two orders of magnitude than the one of oxalic acid ($k = 1.4 \cdot 10^6$ M^{-1} s^{-1}) [8, 9], explaining why the oxidation of formic acid occurs first.

3.5. Hydroxylation of SA

3.5.1. Electrochemical hydroxylation

The electrochemical hydroxylation of salicylic acid was investigated in order to detect the presence of hydroxyl radicals during the electrochemical process on the one hand, and, on the other hand, to determine the mechanism of hydroxyl radicals reactivity. The salicylic acid was chosen for model because its hydroxylation reaction and the intermediates are well known. Firstly, the electrochemical oxidation of SA was performed using a BDD electrode in perchloric acid medium at a current density of 20 A m^{-2}, a value lower than the limiting current to ensure a partial oxidation of the SA. The study of the reaction intermediates was performed by *HPLC* analysis allowing the identification of the mechanism of SA oxidation at diamond. The mechanism of salicylic oxidation is shown in Figure 6.12. 2,3- and 2,5-dihydroxylated benzoic acids (DHBA) are the main intermediates and when decarboxylation occurs, catechol is produced.
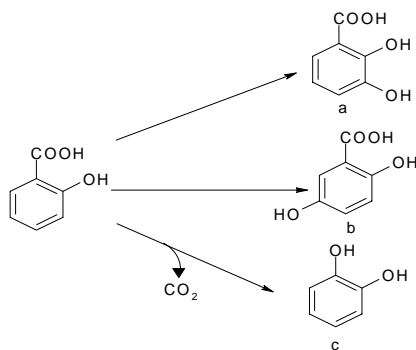
Figure 6.12 Mechanism of salicylic acid hydroxylation (a) 2,3-DHBA, (b) 2,5-DHBA, (c) Catechol.
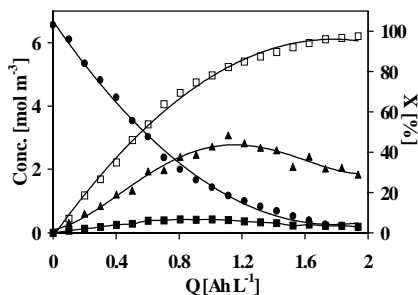
Figure 6.13 Concentrations of (●) SA, (▲) 2,5-DHBA, (■) 2,3-DHBA as a function of specific charge. Current control regime, $j = 20$ A m^{-2}, $[SA]_0 = 7.25$ mM, Electrolyte 1 M HClO$_4$, T = 25°C. (□) X of SA.
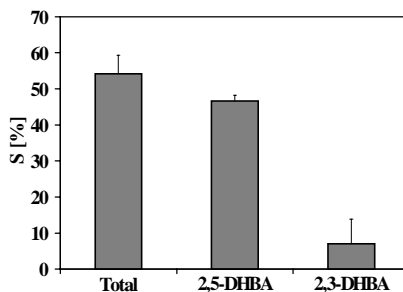
Figure 6.14 Average selectivity of dihydroxylated intermediates. Electrolysis of 7.25 mM SA solution, $j = 20$ A m^{-2}, Electrolyte 1M HClO$_4$, T = 25°C.

Figure 6.13 represents the evolution of concentrations of SA, 2,3- and 2,5-DHBA during the electrolysis as well as the conversion of SA. These results show, as expected, that the hydroxylation reaction takes place and leads to the formation of dihydroxylated intermediates (2,3- and 2,5-DHBA). Under these conditions of hydroxylation, a majority of 2,5-DHBA is produced. Figure 6.14 shows the average selectivity in dihydroxylated intermediates obtained during the electrolysis of SA. The total average selectivity is equal to 54%, for which 47% are due to 2,5-DHBA.

3.5.2. Chemical hydroxylation

A comparison with chemical production of hydroxyl radicals was also carried out. The hydroxyl radicals were produced by two chemical reactions using Fenton reaction (SA, hydrogen peroxide and Fe^{2+}) or H$_2$O$_2$ - *UV* (SA, H$_2$O$_2$ and *UV* light). The reactions were followed by *HPLC* to characterize the formation of intermediates (Figure 6.15, Figure 6.17). In harmony with the electrochemical results and according to the mechanism of the reaction between salicylic acid and hydroxyl radicals, dihydroxylated benzoic acids were produced. In these cases, a majority of 2,3-DHBA was formed compared to 2,5-DHBA. Figure 6.16 and Figure 6.18 represent the average selectivity of 2,3- and 2,5-DHBA for Fenton and *UV*-H$_2$O$_2$ reactions, respectively. The total average

selectivity is equal to 25% for Fenton and 50% for photolysis. This difference of selectivity (compared to the electrochemical experiment for which a majority of 2,5-DHBA is produced) will be discussed in more details in Chapter 10.
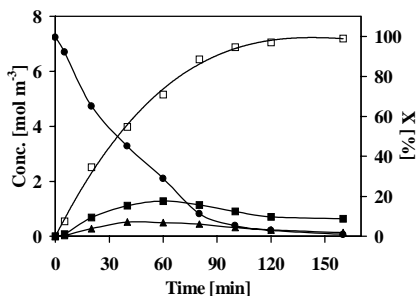

Figure 6.15 Concentrations of (●) SA, (▲) 2,5-DHBA, (■) 2,3-DHBA as a function of time. $[SA]_0 = 7.25$ mM, Fe^{2+} 0.6M $[H_2O_2]$ 3%. Electrolyte 1 M $NaClO_4$, pH 4.4. (□) X of SA.
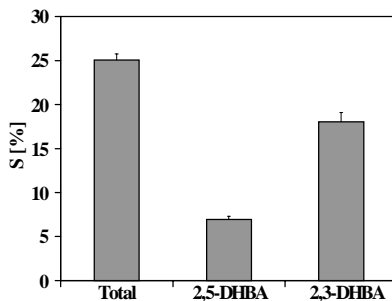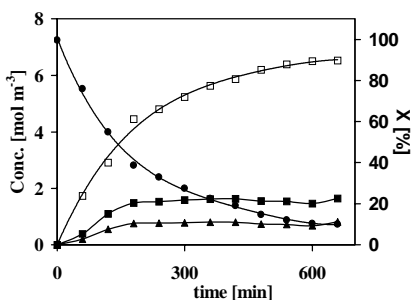

Figure 6.16 Average selectivity of dihydroxylated intermediates. $[SA]_0 =$ 7.25 mM, Fe^{2+} 0.6M $[H_2O_2]$ 3%. Electrolyte 1 M $NaClO_4$, pH 4.4, T = 25°C. $[H_2O_2]/[SA] = 7$.

Figure 6.17 Concentrations of (●) SA, (▲) 2,5-DHBA, (■) 2,3-DHBA as a function of time. $[SA]_{in} = 7.25$ mM, $[H_2O_2]$ 3%. Electrolyte 1 M $NaClO_4$, pH 4.4. (□) Conversion of SA.
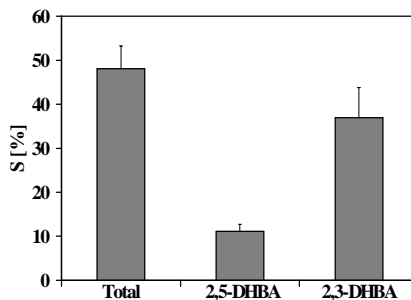

Figure 6.18 Average selectivity of dihydroxylated intermediates. $[SA]_{in} =$ 7.25 mM, $[H_2O_2]$ 3%. Electrolyte 1 M $NaClO_4$, pH 4.4.

As explained in Chapter 2, a majority of 2,3-DHBA is expected because of the stabilization of SA by resonance. Salicylic acid contains a carboxyl and a hydroxyl group in position 1 and 2, respectively. The carboxyl group is known to be a strong deactivator

(by resonance), orientating in meta- position, and the hydroxyl group is a strong activator (by resonance) in ortho- and para- positions. In this way, two hydroxylated intermediates are expected in the same concentrations: 2,3-DHBA (ortho attack) and 2,5-DHBA (para attack). However, hydrogen bonding is observed in salicylate, leading to the enhancement of the electron population in the ortho position. Because hydroxyl radicals exhibit a strong electrophilic character, the preferential attack takes place in the ortho position, producing more 2,3-DHBA than 2,5-DHBA.

3.5.3. Influence of the pH

We also note that in the electrochemical case, the ratio between 2,5- and 2,3-DHBA is almost equal to 6 while in both chemical cases, the ratios are lower than 1 (Figure 6.19).
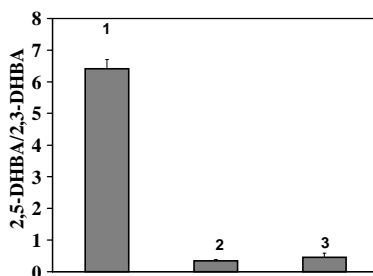

Figure 6.19 2,5-DHBA/2,3-DHBA ratio (1) electrochemical oxidation, (2) Fenton reaction, (3) UV-photolysis, $[SA]_0 = 7.25$ mM.

Some parameters could influence the selectivity for dihydroxylated intermediates. In the first place, the influence of the pH can be considered, because, the change in pH can modify the electronic density distribution. The electrochemical hydroxylation was performed at pH 1, 4.65 and 8 to investigate the influence of the pH on the reaction. As explained in the bibliographic part (Chapter 2), Fenton reaction is very sensitive to pH. Indeed, the pH has normally to be between 3 and 5 to avoid the precipitation of Fe^{2+}. However, an assay was performed in perchloric acid to determine the selectivity for dihydroxylated intermediates in acidic medium. Figure 6.20 shows the different ratios obtained for the electrochemical oxidation and the chemical oxidation at various pH.

The pH does not seem to influence significantly the distribution of the products.

Indeed, the trend of the 2,5-/2,3-DHBA ratio does not change with the pH (even if the ratio decreases with the pH). In the electrochemical case, 2,5-DHBA remains the major product while the chemical hydroxylation by Fenton reaction leads to the formation of a majority of 2,3-DHBA.
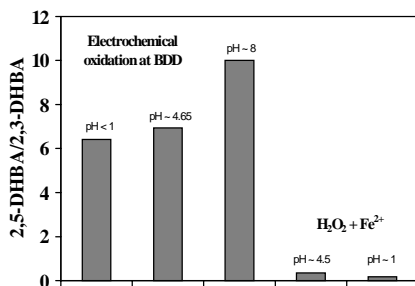

Figure 6.20 2,5-DHBA/2,3-DHBA ratio of electrochemical oxidation at different pH (1, 4.65 and 8) and Fenton reaction, (pH 4.5 and 2), $[SA]_0 = 7.25$ mM. Electrochemical conditions: $j = 20$ A m^{-2}, electrolyte 1M HClO$_4$. Chemical oxidation: $[H_2O_2]/[SA] = 7$.

3.5.4. Stability of 2,3- and 2,5-DHBA

The stabilities of 2,5- and 2,3-DHBA were also followed to verify if 2,3-DHBA was degraded more quickly, explaining why its concentration was lower than the one of 2,5-DHBA. The stability without applied potential was firstly studied and the concentration of both DHBA did not change. The oxidation of each intermediates was also investigated. The knowledge of the kinetics of each intermediates can provide information on the mechanism of hydroxylation. Figure 6.21 and Figure 6.22 represent the evolution of the concentration and the selectivity of DHBA intermediates during their electrolysis. The evolution is quite similar and no characteristic difference in the rate of decomposition is distinguishable. Altogether that means that both 2,3- and 2,5-DHBA are oxidized with similar kinetics.
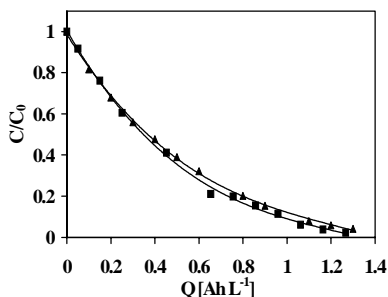
Figure 6.21 Concentrations of (▲) 2,3-DHBA and (■) 2,5-DHBA as a function of the specific charge. Electrolysis in HClO$_4$ 1M, T = 25°C, j = 20 A m^{-2}.
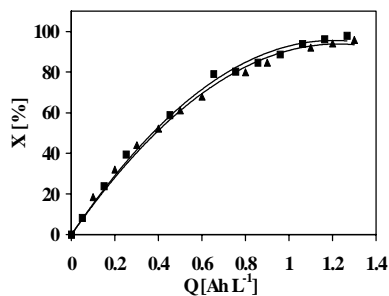
Figure 6.22 Conversion of (▲) 2,3-DHBA and (■) 2,5-DHBA as a function of the specific charge. Electrolysis in HClO$_4$ 1M, T = 25°C, j = 20 A m^{-2}.

Therefore, the stability of both 2,3- and 2,5-DHBA do not seem to influence on the dihydroxylated products ratio.

4. CONCLUSIONS

The spin trapping method permitted to highlight the presence of hydroxyl radicals. Indeed, first experiments, which consisted in trapping hydroxyl radicals that were produced either electrochemically or chemically with DMPO showed electron spin resonance spectra that were typical of this spin-adduct. The spectrum recorded of the experiment performed at boron-doped diamond gave the same hyperfine couplings than those obtained for the Fenton reaction (chemical reaction of OH radical production) at about 15 Gauss [3]. A lot of spin-trapping experiments were done with chemically produced hydroxyl radicals (Fenton, photo-oxidation...) [4, 2, 10], but it does not exist example of spin trapping recorded for an electrochemical production of hydroxyl radicals at BDD electrode.

ESR experiments were corroborated by *UV* studies of *p*-nitrosoaniline-adduct. Indeed, the analysis of the adduct by *UV* absorbance confirmed the production of hydroxyl radicals at BDD anode. The bleaching of the RNO solution was linear, indicating that the reaction of spin-trapping had taken place. The maintenance of the *TOC* concentration further indicated that the removal of RNO concentration was only due to

the reaction between hydroxyl radicals and *p*-nitrosoaniline.

During water decomposition, a lot of reactive intermediates are produced (hydroxyl radical, ozone, hydrogen peroxide, singlet oxygen, peroxo compounds...). Some are formed directly by the oxidation of water (like OH radicals) and others are obtained by recombination. Hydrogen peroxide is a good example (Equation 6.6). The concentrations of H_2O_2 measured during the electrolysis of a perchloric acid solution demonstrate the production of hydroxyl radicals at diamond anode.

The competitive reaction between organic acids and hydroxyl radicals was performed in order to study if the reactivity of each carboxylic acids was connected to the presence of hydroxyl radicals. The first behavior observed was a discrepancy between formic and oxalic acid oxidations, where the oxidation of formic acid took place before that of oxalic acid. One explanation for this difference in reactivity is the different rate constants between OH radicals and organic acids, which differ from 2 orders of magnitude (10^6 for oxalic acid vs 10^8 M^{-1} s^{-1} for formic acid). It is thus possible to establish a correlation between these rate constants and the fact that the oxidation of formic acid at boron-doped diamond anodes occurs first.

The previous experiments have emphasized the presence and the role of hydroxyl radicals electrogenerated at BDD electrode, but it is also important to know the reactivity of these radicals and their attack mechanism. The reaction of hydroxylation of salicylic acid was chosen for model. Salicylic acid is hydroxylated by hydroxyl radicals into two main dihydroxylated compounds (2,3- and 2,5-DHBA). As regards to the comparison between electrochemical and chemical hydroxylation, opposite behaviors were observed. Indeed, the chemical hydroxylation forms preferentially the ortho isomer (2,3-DHBA) while the electrochemical oxidation leads to the preferential production of the para isomer (2,5-DHBA). This difference of reactivity cannot be explained by the pH influence or by the decomposition kinetics of these intermediates. This point will be discussed in more details in the general discussion.

5. REFERENCES

[1]   M. Hatada, I. Kraljic, A. El. Samahy, and C.N. Trumbore, *J. Phys. Chem.*, **78** (9) (1974) 888.

[2]   G. Liu, J. Zhao, and H. Hidaka, *J. Photochem. Photobiol. A: Chem.*, **133** (2000) 83.

[3]   G.R. Buettner, *Free Rad. Biol. Med.*, **3** (1987) 259.

[4]   M. Hermes-Lima, N.C.F. Santos, J. Yan, M. Andrews, H.M. Schulman, and P. Ponka, *Biochim. Biophys. Acta*, **1426** (1999) 475.

[5]   R.A. Floyd and J.M. Carney, *Annals of Neur.*, **32** (1992) S22.

[6]   Wilson, *J. Rad. Phys. Chem.*, **3** (1971) 211.

[7]   E. Neyens and J. Baeyens, *J. Hazard. Mat.*, **B98** (2003) 33.

[8]   G.V. Buxton, C.L. Greenstock, W.P. Helman, and A.B. Ross, *J. Phys. Chem.*, **17** (2) (1988) 513.

[9]   www.rcdc.nd.edu/compilations/Hydroxyl/OH.htm.

[10]   Z. Ma, B. Zhao, and Z. Yuan, *Anal. Acta*, **389** (1999) 213.

Chapter 7. Electrochemical oxidation of 4-chlorophenoxyacetic acid

1. INTRODUCTION

The protection of the environment becomes a major issue for future technologies progress. Electrochemical processes are an attractive method for waste water treatment [1-4]. In this aim, several anode materials have been tested, but some of them exhibited a rapid loss of activity due to surface fouling (glassy carbon, PbO_2) or the short life time (SnO_2). Due to its exceptional properties (high anodic stability and wide potential window), boron-doped diamond proved to be a promising material for the complete combustion of organics [5, 6].

4-chlorophenoxyacetic acid (4-CPA) is known as a powerful pesticide, which was first registered in the USA in 1969. It is used in the food industry as a plant regulator to restrict root growth during seed germination of mung beans and as fruiting bloom set for tomatoes.
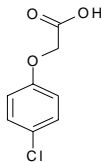
Figure 7.1 Structure of 4-chlorophenoxyacetic acid (4-CPA).

In order to validate the theoretical models developed in Chapter 3 for a one-compartment electrochemical flow cell, the electrochemical oxidation of 4-CPA was investigated at BDD anode.

4-CPA was firstly studied by cyclic voltammetry in the region of water stability as well as at higher potential in order to characterize its behavior at BDD electrode and to calculate its diffusion coefficient.

Then, bulk electrolysis in the one-compartment electrochemical flow cell was carried out to study the ability of 4-CPA to be oxidized at diamond anode. The experimental results were compared with the theoretical model for organic oxidation at *non active* anode.

2. EXPERIMENTAL

2.1. Electrochemical measurements

Cyclic voltammetry was performed in the electrochemical characterization cell described in Chapter 4. The working electrode was a Si/BDD plate of 1 cm^2 of geometric area. The counter electrode was a platinum wire and the reference was a Hg/HgSO$_4$/K$_2$SO$_4$ (sat). All potentials are given relative to the standard hydrogen electrode (SHE). The supporting electrolyte was 1 M HClO$_4$. Fluka Chemie and Riedel-de Haën chemicals, and Milli-Q water were used to prepare the solutions.

2.2. Bulk electrolysis

Bulk oxidation of 4-CPA was carried out using the one-compartment electrochemical flow cell operating in galvanostatic mode (Chapter 4). The electrolyte was a 1 M HClO$_4$ solution.

2.3. *HPLC* measurement

The concentrations of organic compounds were monitored by chromatography *HPLC* on a Shimadzu series 6 (Shimadzu Corporation, Tokyo, Japan) with an *UV* detection. Two columns were used for the identification of the oxidation products. The aromatic products were detected with a Nucleosil C18 column (Supelco) with acetonitrile/water (58/42) as mobile phase (the pH was adjusted to 2.1 using H_3PO_4 98%), with a flow rate of 0.8 mL min^{-1} and a wavelength of 254 nm. The carboxylic acids were monitored with a Supelcogel H column (Supelco) with water and 0.13% phosphoric acid solution at a flow rate of 0.5 mL min^{-1} (λ = 210 nm). All retention times are given in Table 7.1.

Compounds	Formula	Nucleosil C18 Retention time [min]	Supelcogel H Retention time [min]
4-chlorophenoxyacetic acid	$C_7H_6O_3$	3.88	-
4-chlororesorcinol	$C_7H_6O_2$	2.96	-
4-chlorophenol	C_6H_5ClO	4.74	-
Benzoquinone	$C_6H_4O_2$	3.2	-
Glycolic acid	$C_2H_4O_3$	-	14
Malic acid	$C_4H_6O_5$	-	13.5
Oxalic acid	$C_2H_2O_4$	-	8
Glyoxylic acid	$C_2H_2O_3$	-	11
Formic acid	CH_2O_2	-	18
Maleic acid	$C_4H_4O_4$	-	10

Table 7.1 Structure and retention time of detected intermediates.

3. RESULTS AND DISCUSSION

The electrochemical behavior of 4-CPA was investigated by cyclic voltammetry at BDD electrode in the potential region of electrolyte stability as well as in presence of electrolyte decomposition. The theoretical model for 4-CPA oxidation at a *non active* anode was used to predict the chemical oxygen demand and the instantaneous current

efficiency evolutions.

3.1. Cyclic voltammetry

The electrochemical oxidation of 4-CPA was investigated in a perchloric acid solution at ambient temperature.

Figure 7.2 shows consecutive cyclic voltammograms of 4.2 mM 4-CPA in 1 M $HClO_4$ at a scan rate of 50 mV s^{-1}. The solution was stirred before each cycle. As the number of cycles increased, the anodic current density peaks decreased markedly until a steady state was reached (five cycles). This deactivation is due to the deposition of an organic film on the electrode surface. Washing with an organic solvent like isopropanol did not reactivate the electrode. However, the initial activity of the electrode surface could be restored by anodic polarization in the same solution for 60 s at 2.6 V (vs SHE) as shown in Figure 7.2, curve d. The potential chosen for the reactivation of the surface was in the domain of water decomposition, a reaction that leads to the production of hydroxyl radicals.
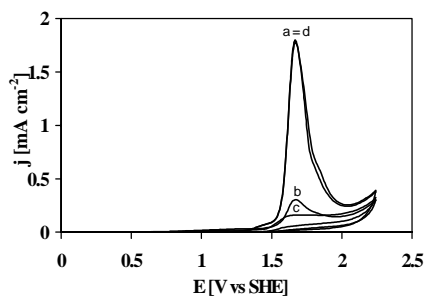
Figure 7.2 Consecutive cyclic voltammograms of 4mM 4-CPA in 1 M $HClO_4$: (a) first cycle, (b) second cycle, (c) fifth cycle, (d) after pre-treatment at 2.6 V vs for 60 s. SHE. v = 50 mV s^{-1}, T = 25°C.

Then, the effect of the concentration of 4-CPA was studied. Figure 7.3 shows the first cyclic voltammograms recorded at a scan rate of 50 mV s^{-1} for different concentrations of 4-CPA in 1 M $HClO_4$. An oxidation peak was observed at approximately 1.65 V vs SHE. As shown in Figure 7.4, the oxidation peak current density increased linearly with the 4-CPA concentration.
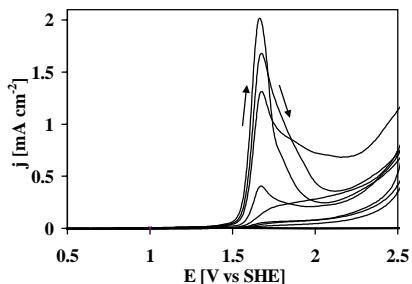
Figure 7.3 Cyclic voltammograms (1st scan) for 4-CPA in 1 M $HClO_4$ at BDD electrode. [4-CPA] = 0.5, 2, 3, 4 mM. v = 50 mV s^{-1}, T = 25°C.
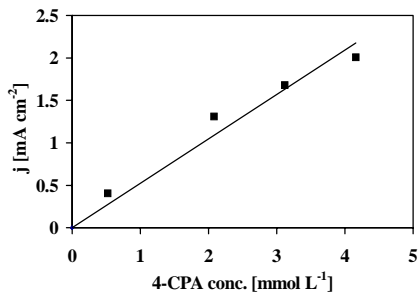
Figure 7.4 Dependence of the peak current density with the concentration of 4-CPA. [4-CPA] = 0.5, 2, 3, 4 mM. v = 50 mV s^{-1}, T = 25°C.

The increase of the peak current with the concentration of 4-CPA indicates that 4-CPA oxidation was responsible for the response of the electrode.

The value of $7.56 \cdot 10^{-5}$ cm^2 s^{-1} for the diffusion coefficient D_O was calculated from Figure 7.3 using the following relation (Chapter 3):

$$i_p = (2.69 \times 10^5)n^{3/2}AC_O^*D_O^{1/2}v^{1/2} \qquad 7.1$$

with A = 1 cm^2 and v = 50 mV s^{-1}.

The dependence of the current peak on the scan rate at a fixed 4-CPA concentration (4.16 mM) was also investigated. Figure 7.5 represents the cyclic voltammogram obtained for the 4-CPA solution in $HClO_4$ at different scan rates (from 10 to 100 mV s^{-1}). The peak potential shifted to higher potentials when the scan rate was increased, corresponding to a linear dependence of the peak current density with the square root of the scan rate (Figure 7.6).
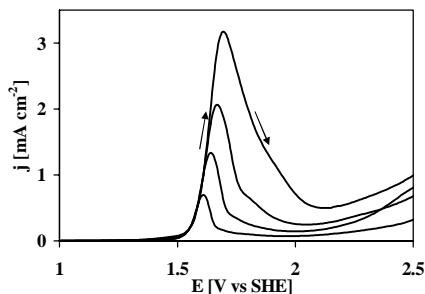
Figure 7.5 Cyclic voltammograms for a 4.6 mM 4-CPA solution in 1 M HClO$_4$ at BDD electrode at different scan rates: 10, 25, 50, 100 mV s^{-1}, T = 25°C.
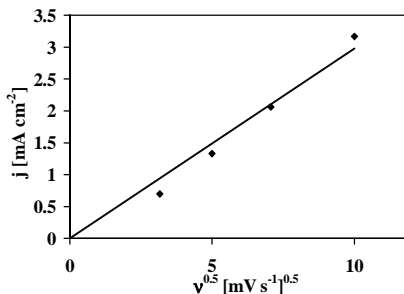
Figure 7.6 Dependence of the peak current density with the concentration of 4-CPA.

The linear relation found between peak currents and the square root of the scan rate is typical of a diffusion controlled process.

A value of $D_O = 7.63 \cdot 10^{-5}$ cm^2 s^{-1} was calculated from the Figure 7.6 using Equation 7.1. Both values of diffusion coefficient are similar and are consistent with typical values of D_O.

From the variation of the intensity of the peak potential (E_p) with the scan rate (ν) (Figure 7.7), the transfer coefficient α was calculated from the following equation:

$$E_P = E^0 + \frac{RT}{\alpha nF}\left(0.78 - \ln k^0 + \ln\sqrt{D_0\frac{\alpha nF}{RT}}\right) - \frac{RT}{2\alpha F}\ln v \qquad 7.2$$

Considering a one-electron transfer reaction, for which $n = 1$, a value of 0.36 was calculated for the anodic transfer coefficient. For metal, this value was expected to be equal to 0.5 (α + β = 1). The lower value of the transfer coefficient can be explained by the partial semiconductor character of BDD electrodes [7].
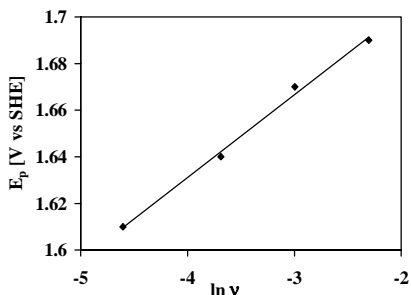
Figure 7.7 Dependence of the peak potential with the scan rate. [4-CPA]$_0$ = 4.6 mM in 1 M HClO$_4$, T = 25°C.

3.2. Bulk electrolysis

The anodic oxidation of 4-CPA was investigated using BDD anode in perchloric acid at 35°C.

The oxidation of 4-CPA is supposed to be a fast reaction under mass transport control, assisted by the electrogenerated hydroxyl radicals produced by the water decomposition (Equation 7.3):

$$C_8H_7ClO_3 + 13H_2O \rightarrow 8CO_2 + 32e^- + 33H^+ + Cl^- \qquad 7.3$$
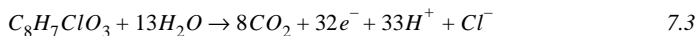
The limiting current density for the electrochemical oxidation is given by the following equation:

$$j_{lim}^0 = 4Fk_mCOD^0 \qquad 7.4$$

where j_{lim}^0 is the limiting current density (A m^{-2}) at a given time t, 4 the number of exchanged electrons, F the Faraday's constant (C mol^{-1}), k_m the mass transport coefficient (m s^{-1}) and COD^0 the initial chemical oxygen demand (mol m^{-3}).

The values of total organic carbon (*TOC*), chemical oxygen demand (*COD*), instantaneous current efficiency (*ICE*) and 4-CPA and its by-products concentrations were followed during the different experiments of bulk electrolysis. In order to study the

three different regimes (charge transfer, mass transport and mixed controls), the electrolysis of a 4-CPA solution was performed at three different current densities (300, 80 and 20 A m^{-2}).

Figure 7.8 shows the evolution of the *COD* as a function of time during the electrolysis. The experimental data were compared with the theoretical model (solid lines). A limiting current density of 247 A m^{-2} was calculated. The curve (a), corresponding to the mass-transport control, exhibited a rapid decrease, indicating a fast and total combustion of the organic. The same behavior was observed for the *ICE* evolution (Figure 7.9).

Under these conditions, *COD* and *ICE* are described by the following equations:

$$COD_{(t)} = COD^0 \exp\left(-\frac{Ak_m}{V_R}t\right) \qquad\qquad 7.5$$

$$ICE = \frac{1}{\alpha}\exp\left(-\frac{Ak_m}{V_R}t\right) \qquad\qquad 7.6$$

where α is the ratio j_{appl}/j_{lim}, COD^0 is the initial *COD* (molO$_2$ m^{-3}), A is the electrode surface, k_m is the mass transfer coefficient (m s^{-1}), V_R is the cell volume (m^3) and t is the time (s).

ICE value was under 1 and followed an exponential decrease as expected by the theoretical model.

The current controlled regime (case (c)) had a linear trend for both *COD* and *ICE,* as predicted. In this case, the *ICE* remained constant and equal to 1, meaning a partial oxidation into intermediates compounds. The evolution of *COD* is described by Equation 7.7:

$$COD_{(t)} = COD^0\left(1 - \frac{\alpha Ak_m}{V_R}t\right) \qquad\qquad 7.7$$

The third case (b) represents the mixed control, for which the two previous behaviors are observed. In fact, a linear decrease of *COD* occurred first, corresponding to an *ICE* of 1. Then, after a critical time, both *COD* and *ICE* decreased exponentially. The evolution of the global parameters are described by these equations:

$$COD_{(t)} = \alpha COD_0 \exp\left(-\frac{Ak_m}{V_R}t + \frac{1-\alpha}{\alpha}\right) \qquad\qquad 7.8$$

$$ICE \;=\; \exp\!\left(-\,\frac{A k_m}{V_R}t + \frac{1-\alpha}{\alpha}\right) \qquad\qquad 7.9$$
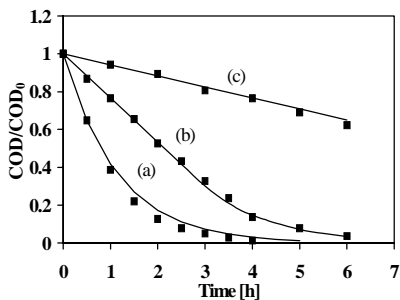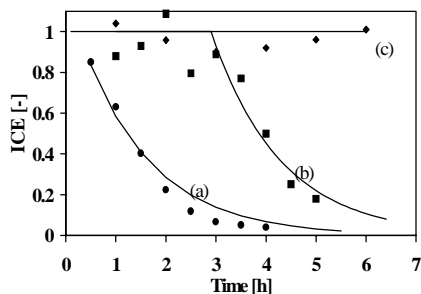

Figure 7.8 Evolution of COD during the electrochemical oxidation of a 4.6 mM 4-CPA solution in 1M $HClO_4$ at BDD anodes at different current densities: (a) mass-transfer control at 300 A m^{-2}, (b) mixed control at 80 A m^{-2}, (c) current control at 20 A m^{-2}. T = 35°C. Comparison between experimental data (points) and theoretical model (solid lines). $COD^0 = 32$ $molO_2$ m^{-3}.

Figure 7.9 Evolution of ICE during the electrochemical oxidation of a 4.6 mM 4-CPA solution in 1M $HClO_4$ at BDD anodes at different current densities: (a) mass-transfer control at 300 A m^{-2}, (b) mixed control at 80 A m^{-2}, (c) current control at 20 A m^{-2}. T = 35°C. Comparison between experimental data (points) and theoretical model (solid lines). $COD^0 = 32$ $molO_2$ m^{-3}.

The formation of oxidation intermediates was monitored by *HPLC*. From the intermediates identified, we proposed the following mechanism for complete incineration of 4-CPA. 4-CPA is firstly hydroxylated in 4-chlorophenol and glycolic acid (1), then 4-chlorophenol is hydroxylated in 4-chloro-resorcinol (2), which is then oxidized in 1,2,4-benzenetriol (4). The cleavage of the benzenic ring leads to the formation of malic acid and oxalic acid (5). Malic acid can produce either oxalic acid (7) or glycolic acid (6). Glycolic acid, also formed in the first step, produces glyoxylic acid (3), which is transformed into oxalic acid, formic acid and finally carbon dioxide and water. These reactions are illustrated in the following reaction scheme (Figure 7.10).
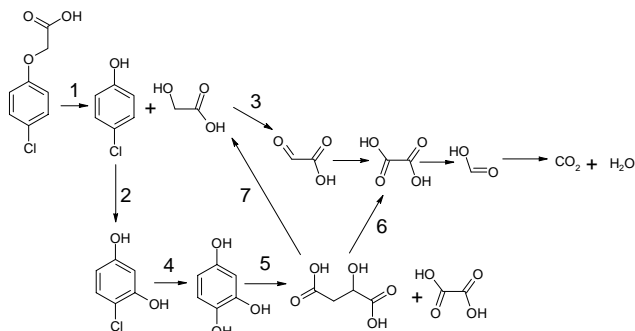
Figure 7.10 Possible mechanism for the complete oxidation of 4-CPA at BDD electrode.

As described in the theoretical part (Chapter 3), the oxidative process can be described in terms of flux by means of the parameters γ and ν, where γ is the ratio between the rate of hydroxyl radicals production and the flux of organics and the ν is the ratio between hydroxyl radicals moles and 4-CPA moles.

The electrolysis of 4-CPA was carried out at two different current densities (16 and 300 A m^{-2}). The parameters ν and γ, as well as the percentage of CO$_2$ and aromatics, were calculated in both cases (Chapter 3).

Figure 7.11 shows the results obtained for the electrolysis at high current density (300 A m^{-2}). At this current density, the complete incineration of 4-CPA is assumed to require 32 hydroxyl radicals (or 32 electrons):

$$C_8H_7ClO_3 + 32HO^{\bullet} \rightarrow 8CO_2 + HCl + 19H_2O \qquad 7.10$$

In this case, according to the γ–ν model (Chapter 3), γ is equal to 37 and ν is equal to 32, respectively. The percentage of aromatics was almost nil while the percentage of CO$_2$ was equal to 90% (Figure 7.11). These results confirm the rapid total oxidation of 4-CPA into CO$_2$. Indeed, a γ higher than ν means that the production of OH radicals is higher than the flux of organics. Therefore, the process is under mass transport control.

On the opposite case, at low potential, selective oxidation of 4-CPA takes place implying 2 hydroxyl radicals (or 2 electrons) (ν is equal to 2):

$$C_8H_7ClO_3 + 2HO^{\bullet} \rightarrow C_6H_5ClO_2 + C_2H_4O_3 \qquad 7.11$$
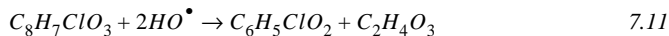
At this current density (16 A m^{-2}), according to the model, γ is equal to 1.97 and ν to 2. γ is lower than ν, indicating that the production of OH radicals is less important (compared to the previous case) and that the organics can slowly react with the radicals. The electrolysis is under charge transfer control and leads to the selective oxidation of 4-CPA in aromatics compounds, then carboxylic acids, and finally CO_2. In confirmation of that, Figure 7.12 shows the high percentage of aromatics (95%) and the low percentage of CO_2 (15%) obtained during this experiment.
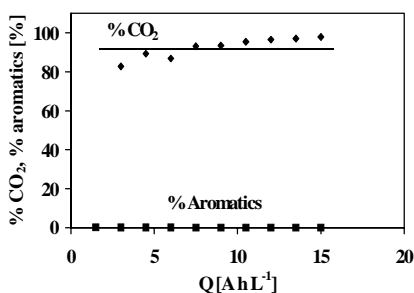
Figure 7.11 Trend of the percentage of ($\blacklozenge$) 4-CPA converted into CO_2 and ($\blacksquare$) 4-CPA converted in aromatics during the electrolysis of a 4.2 mM 4-CPA solution in 1M $HClO_4$ at 300 A m^{-2}. T = 35°C.
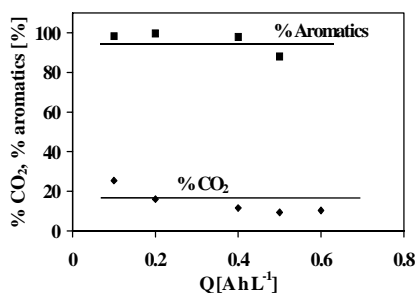
Figure 7.12 Trend of the percentage of ($\blacklozenge$) 4-CPA converted into CO_2 and ($\blacksquare$) 4-CPA converted in aromatics during the electrolysis of a 4.2 mM 4-CPA solution in 1M $HClO_4$ at 20 A m^{-2}. T = 35°C.

4. CONCLUSIONS

The electrochemical oxidation of 4-chlorophenoxyacetic acid at boron-doped diamond was studied in the potential region of water stability. A blocking phenomenon was observed at the diamond surface, as a result of the formation of a polymeric film. The electrochemical behavior was also performed and investigated by cyclic voltammetry in the potential region of electrolyte decomposition (after reactivation of the electrode surface by anodic polarization at high potential). These measurements have allowed to calculate the diffusion coefficient D_O of the 4-CPA and the anodic transfer coefficient α of the BDD electrode.

The bulk electrolysis of 4-CPA was also performed in order to characterize the

oxidation process mechanism. We can conclude that it is possible to fully oxidize 4-chlorophenoxyacetic acid at BDD electrode. It also appears, as regards of these results and previous experiments made in our lab, that either partial oxidation or complete combustion of a large range of organic compounds can be performed at diamond anode [8, 9]. The theoretical model developed for the oxidation of organics at *non active* electrode is consistent with the experimental data. A reaction pathway for the total combustion of 4-CPA was also proposed.

5. REFERENCES

[1]   F. Bonfatti, S. Ferro, F. Lavezzo, M. Malacarne, G. Lodi, and A. De Battisti, *J. Electrochem. Soc.*, **146** (1999) 2175.

[2]   Ch. Comninellis and E. Plattner, *Chimia*, **42** (1988) 250.

[3]   Ch. Comninellis and C. Pulgarin, *J. Appl. Electrochem.*, **23** (1993) 108.

[4]   M. Panizza, C. Bocca, and G. Cerisola, *Water Research*, **34** (9) (2000) 2601.

[5]   M. Fryda, D. Herrmann, L. Schäfer, C.P. Klages, A. Perret, W. Haenni, Ch. Comninellis, and D. Gandini, *New Diamond Frontier Carbon Technol.*, **9** (3) (1999) 229.

[6]   D. Gandini, E. Mahé, P.-A. Michaud, W. Haenni, A. Perret, and Ch. Comninellis, *J. Appl. Electrochem.*, **30** (2000) 1345.

[7]   Y.V. Pleskov, V.P. Varnin, I.G. Teremetskaya, and A.V. Churikov, *J. Electrochem. Soc.*, **144** (1) (1997) 175.

[8]   J. Iniesta, P.-A. Michaud, M. Panizza, and Ch. Comninellis, *Electrochem. Commun.*, **3** (2001) 346.

[9]   M.A. Rodrigo, P.-A. Michaud, I. Duo, M. Panizza, G. Cerisola, and Ch. Comninellis, *J. Electrochem. Soc.*, **148** (5) (2001) 60.

Chapter 8. Oxidation of salicylic acid using a two-compartments electrochemical flow cell

1. INTRODUCTION

This chapter deals with the electrochemical oxidation of salicylic acid using a two-compartments electrochemical flow cell. This cell is similar to the one-compartment electrochemical flow cell described in the previous chapter, but, as shown in Chapter 4, cathode and anode are separated by a Nafion® membrane. Because of its configuration, hydrodynamic conditions are not very well established and the prediction of the mass transport coefficient is difficult due to the presence of local turbulences (inlet and outlet zones). Indeed, the only way to obtain the average value of the mass transport coefficient is to measure it with a ferri/ferro cyanide system. However, in spite of the fact that the mass transport coefficient has to be measured and cannot be predicted by theory, this electrochemical flow cell present some advantages. Indeed, the presence of two compartments allows to separate the reactions occurring at both the cathode and the anode

and eventually to measure the gas evolution of each part. Moreover, the high surface area of the electrode (63.6 cm^2) permits to treat a large volume of organics (500 mL). The interest of this cell also resides in the possibility to work with a continuous stirred tank reactor in order to investigate the reactions more precisely.

In this chapter, the electrochemical characterization of SA was performed by cyclic voltammetry. Then, the oxidation of salicylic acid was investigated at different current densities through the measure of global parameters (chemical oxygen demand and instantaneous current efficiency). The oxidation reaction was also studied by the characterization of the intermediates produced during the reaction, and a carbon balance was established to propose a mechanism for SA oxidation. The effect of the supporting electrolyte on the reaction was also studied by comparing $HClO_4$ with H_2SO_4.

Finally, the models developed in our laboratory for the one-compartment electrochemical flow cell operating in a batch recirculation mode under galvanostatic conditions (Chapter 3) were applied to the two-compartments electrochemical cell to predict *COD* and *ICE* evolutions and compare these values with the experimental results obtained during the oxidation process.

2. EXPERIMENTAL

2.1. Electrochemical measurements

Cyclic voltammetry was performed in the electrochemical cell described in Chapter 4. The working electrode was a BDD plate. All values of potential are given relative to the standard hydrogen electrode (*SHE*) and the current densities are calculated with respect to a geometric area of 1 cm^2. The supporting electrolyte was either 1 M $HClO_4$ or 1 M H_2SO_4. Fluka Chemie and Riedel-de Haën chemicals and Milli-Q water were used to prepare the solutions.

2.2. Bulk electrolysis

The bulk oxidation of salicylic acid was carried out using the two-compartments electrochemical flow cell in galvanostatic mode (Chapter 4). The anolyte was a solution of 7.25 mM salicylic acid in 1 M $HClO_4$, and the catholyte a 1M $HClO_4$ solution.

Selectivity and conversion

The selectivity (*S*) toward hydroxylated intermediates, relative to the amount of salicylic acid converted, and the conversion (*X*) of SA have been defined as:

$$S = \frac{[DHBA]_t - [DHBA]_0}{[SA]_0 - [SA]_t} \times 100 \qquad\qquad 8.1$$

$$X = \frac{[SA]_0 - [SA]}{[SA]_0} \times 100 \qquad\qquad 8.2$$

where $[DHBA]_0$ and $[DHBA]_t$ are the concentrations (mol m^{-3}) of 2,3- or 2,5-dihydroxylated acids at time 0 and *t*, respectively, and $[SA]_0$ and $[SA]_t$ are the concentrations (mol m^{-3}) of salicylic acid at time 0 and *t*, respectively.

2.3. Determination of the mass transport coefficient k_m

The mass transfer coefficient k_m was determined with an equimolar mixture of the redox couple ferri/ferro cyanide (0.02 to 0.08 M) in 1 M NaOH solution [1]. For the measure, both the cathode and the anode were nickel disks. Considering the symmetry of the electrochemical cell and supposing that the diffusion coefficients are the same for the reduced and the oxidized species, it was possible to calculate k_m from the limiting current according to the following relation:

$$k_m = \frac{j_{lim}}{nFAC} \qquad\qquad 8.3$$

The limiting current was measured by linear sweep voltammetry for different concentrations of Fe(CN)$_6$ III/II at a flow of 200 L h^{-1}. k_m of $1.97 \cdot 10^{-5}$ m s^{-1} was calculated. A second measure was performed by measuring the evolution of the limiting current as a function of the flow rate $\dot{V}$ (from 30 to 200 L h^{-1}) at a given ferri/ferro concentration (80 mol m^{-3}). In the latter case, the following relation was established:

$$k_m = 2.78.10^{-6} \dot{V}^{0.38} \qquad\qquad 8.4$$

In relation to Equation 8.4, it appears that experimental conditions influence a lot the value of the mass transfer coefficient.

For a laminar flow, the Leveque's relation [2] (Equation 8.5) allows to estimate k_m for a laminar flow in a rectangular channel. The relation between Sherwood (Sh), Reynolds (Re) and Schmidt (Sc) numbers is given by:

$$Sh = 1.85\left[Re.Sc.\frac{d_h}{L}\right]^{1/3} \qquad\qquad 8.5$$

$$\text{with } Sc = \frac{\nu}{D} \text{ , } Re = \frac{\nu L}{\nu} \text{ and } Sh = \frac{k_m d_h}{D} \qquad\qquad 8.6$$

where ν is the kinematic viscosity ($m^2\,s^{-1}$), D the diffusion coefficient ($m^2\,s^{-1}$), v the rate ($m\,s^{-1}$), L the length (m), and d_h the hydraulic diameter (m).

k_m can thus be calculated by the following relation:

$$k_m = \frac{Sh.D}{d_h} \qquad\qquad 8.7$$

Considering a flow rate of 200 L h^{-1}:

$$Sc = \frac{\nu}{D} = \frac{0.01}{5.10^{-6}} = 2000$$

The width h is calculated as $h = \frac{\pi}{4}L = 6.28\,cm$

and the section $A = h.e = 6.28\,cm^2$

and $d_h = \frac{4.\text{section}}{\text{perimeter}} = \frac{4(6.28)}{2(6.28 + 1)} = 1.725\ cm$
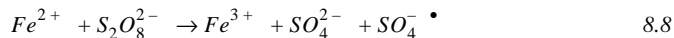
Then, it is possible to calculate the Reynolds number:

$$Re = \frac{\dot{V}d_h}{A\nu} = 1526$$

According to Equation 8.5, Sh is equal to 161 and k_m is equal to 4.66 10^{-6} m s^{-1}. For this two-compartments electrochemical flow cell, if we compare the measured k_m (ferri/ferro cyanide system) with the k_m calculated by Leveque's relation (even if in this calculation, the circular geometry of the electrode is reduced to a rectangular form), the experimental mass transport coefficient is about 4.5 times higher than the calculated one.

This result confirms the non homogeneity of the flow in the cell. This heterogeneity is due to the turbulence zones. In this work, the value for k_m of $2 \cdot 10^{-5}$ m s^{-1} was kept.
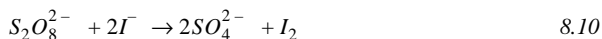
2.4. Persulfate titration

The titration methods are based on the reaction of either ferrous iron or iodine. The first one consists to the oxidation of ferrous ions in ferric ions by persulfates:

$$Fe^{2+} + S_2O_8^{2-} \rightarrow Fe^{3+} + SO_4^{2-} + SO_4^{-} \bullet \qquad \text{8.8}$$

$$Fe^{2+} + SO_4^{-} \bullet \rightarrow Fe^{3+} + SO_4^{2-} \qquad \text{8.9}$$
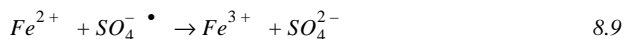
However, persulfate concentrations cannot be determined directly by reduction with iron (II) because the reaction is too slow. Therefore, an excess of iron (II) is added and the excess is back-titrated with a standard cerium (IV) sulfate solution. The measure can be distorted by the presence of organic compounds. Kolthoff *et al.* [3] have shown that the organic can also react with the radical sulfate (Equation 8.8). Consequently, the concentration of persulfate is underestimated. Even if it seems possible to avoid this problem by using bromine, the iodometric titration, more specific and more adapted, was used in this work.

This method is based on the direct titration of iodine produced by oxidation of the iodure:

$$S_2O_8^{2-} + 2I^{-} \rightarrow 2SO_4^{2-} + I_2 \qquad \text{8.10}$$

$$I_2 + 2S_2O_3^{2-} \rightarrow 2I^{-} + S_4O_6^{2-} \qquad \text{8.11}$$

In practice, the pH of the sample becomes acid by adding 3 ml of 20% sulfuric acid. Then, some drops of a 1% ammonium molybdate tetrahydrate solution are added as catalyst, followed by an excess of KI (4 g). The mixture is allowed to react for 15 minutes while stirring. Then, the titration is performed with a 0.01 M solution of thiosulfate. When the solution is almost clear, some drops of a starch solution is added giving to a blue coloration. The titration with thiosulfate continued until the equivalent point.

2.5. *HPLC* measurement

The concentrations of products were monitored by *HPLC* on a chromatograph LC-2010A (Shimadzu Corporation, Kyoto, Japan) with *UV* detection. During this study, two columns were used depending on the investigated products. The first analysis concerned the detection of aromatic compounds: salicylic acid, 2,3-, 2,4-, 2,5-dihydroxylated benzoic acid, catechol, benzoic acid, benzoquinone and hydroquinone. In this analysis, an apolar reversed phase column (silica particles), Nucleosil 7 C8 25 cm x 4.6 mm (HPLC Technology, Macherey Nagel, Macclesfiel Cheshire, UK) was used.

Compounds	Formula	C8 column Retention time [min]	Supelcogel C610-H Retention time [min]
Salicylic acid	$C_7H_6O_3$	13.69	-
Benzoic acid	$C_7H_6O_2$	11.09	-
2,4-DHBA	$C_7H_6O_4$	7.62	-
2,3-DHBA	$C_7H_6O_4$	7.18	-
2,5-DHBA	$C_7H_6O_4$	6.42	-
Catechol	$C_6H_6O_2$	5.49	-
Hydroquinone	$C_6H_6O_2$	4.26	-
Fumaric acid	$C_4H_4O_4$	-	21.94
Maleic acid	$C_4H_4O_4$	-	11.33
Oxalic acid	$C_2H_2O_4$	-	8.67

Table 8.1 Structure and retention times of detected intermediates.

The polar mobile phase was a mixture of 80/20 water-H_3PO_4 1%/acetonitrile. The elution was performed at an isocratic flow rate of 0.5 mL min^{-1} and at ambient temperature. The injection volume of the samples was 10 mL. The wavelength was equal to 296 nm. The second analysis was used to detect aliphatic compound. Fumaric, maleic and oxalic acids were monitored with an ion exclusion column (sulfonated polystyrene/divinylbenzene copolymer, counter ion H$^+$, Supelcogel C610-H, Supelco, Buchs, CH). The retention is based on the electrostatic repulsion. The wavelength was equal to 210 nm. The method consists in pH and flow gradients. The first step was an elution at 0.5 mL min$^-$

[1] with a mobile phase composed of water-H_3PO_4 0.1% (pH 2.1) allowing the detection of the carboxylic acids. Then, the elution was performed with 100% ultrapure water (pH 6-7) as mobile phase at a flow rate of 0.8 mL min^{-1} in order to purge the column of the aromatic compounds.

2.6. *COD* correction

With sulfuric acid, it is necessary to correct the measured value of COD because of the interference of persulfate with the hydrogen peroxide produced during the reaction. In order to establish the calibration curve for the *COD* determination, the oxidation of a 1 M sulfuric acid solution was carried out at 1 A. The titration of the samples was done following the iodometric method.
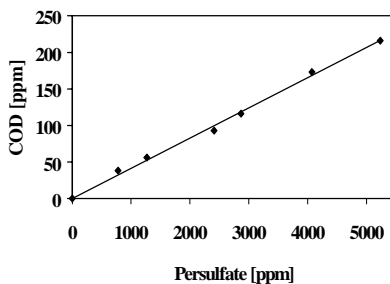
Figure 8.1 *COD* calibration curve for persulfate. 1 M H_2SO_4 solution, $j = 157$ A m^{-2}, T = 25°C.

This linear relation allowed us to establish the following correlation between the measured *COD* value and the real value:

$$COD_{real} = COD_{measured} - 0.0414[S_2O_8^{2-}] \qquad 8.12$$

3. RESULTS AND DISCUSSION

3.1. Electrochemical characterization

The electrochemical behavior of salicylic acid and the influence of the supporting electrolyte were investigated using cyclic voltammetry.

3.1.1. Cyclic voltammetry

Perchloric acid

Figure 8.2 represents the cyclic voltammetry of a SA solution in 1 M $HClO_4$ recorded at a scan rate of 20 mV s^{-1}. As the number of cycles increased, the anodic current density peak (1.75 V vs SHE) decreased markedly until a steady state was reached (cycles 3 and 4). This behavior reveals a deactivation of the electrode surface. This deactivation was attributed to the deposition of an organic film on the electrode surface. Washing the electrode surface with a solvent (e.g. isopropanol) did not reactivate the BDD anode. However, the initial activity was restored by anodic polarization in the same solution for 60 s at 2.6 V vs. SHE. The curve (e) obtained after the reactivation was perfectly superposed to the first one, meaning that the electrode activity was totally restored.
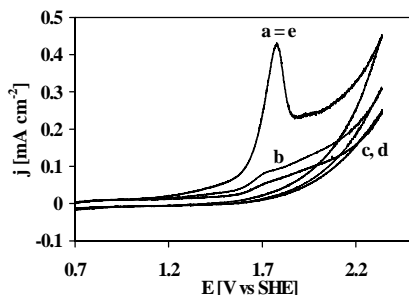
Figure 8.2 Cyclic voltammogram of 7.5 mM SA in 1M $HClO_4$, (a) cycle 1, (b) cycle 2, (c) cycle 3, (d) cycle 4, (e) after-pretreatment at 2.6 V vs *SHE* for 60 s, scan rate 20 mV s^{-1}, T = 25°C.

Sulfuric acid

The cyclic voltammetry was also performed in sulfuric acid medium. Firstly, the voltammogramms were recorded in absence of organics (Figure 8.3). A cathodic peak at -0.75 V vs *SHE* appears, which corresponds to the reduction of species formed during the anodic polarization. Since this behavior is not observed with perchloric acid, these species should be persulfate. Serrano *et al.* [4] have observed the same behavior; the addition of commercial persulfate had for consequence to increase the cathodic peak, confirming the persulfate reduction.

Figure 8.4 shows the first cyclic voltammogramm recorded in presence of salicylic acid. The anodic peak at about 1.75 V vs SHE corresponds to the salicylic acid oxidation (as observed with perchloric acid).
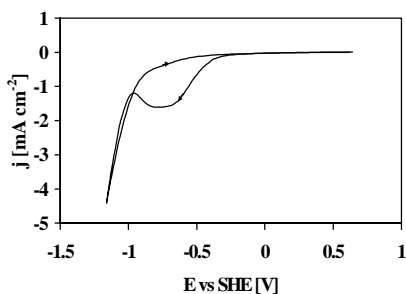
Figure 8.3 Cyclic voltammogram (2nd scan) of 1M H_2SO_4 at BDD electrode. T = 25°C, $\nu = 20$ mV s^{-1}.
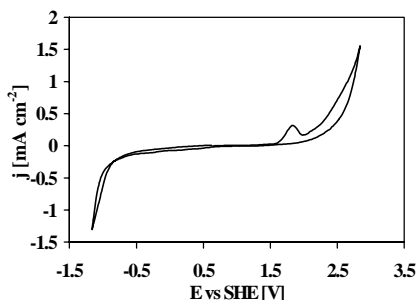
Figure 8.4 Cyclic voltammogram (1st scan) of 7.5 mM SA solution in 1 M H_2SO_4 at BDD electrode, T = 25°C, $\nu = 20$ mV s^{-1}.

3.2. Bulk electrolysis in perchloric acid

Bulk electrolysis in the two-compartments electrochemical flow cell was focused on the identification and the quantification of all the intermediates of SA oxidation. This investigation allowed us on the one hand to validate the models and on the other hand to establish the carbon balance by identification of the by-products. Moreover, the effect of the supporting electrolyte was studied comparing the reaction in perchloric or sulfuric acid media.

Salicylic acid oxidation

For salicylic acid oxidation, the global equation of oxidation is:

$$C_7H_6O_3 + 11H_2O \rightarrow 7CO_2 + 28e^- + 28H^+ \qquad\qquad 8.13$$
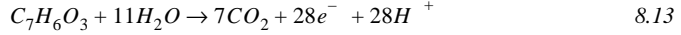
The limiting current density for the electrochemical oxidation of SA depends on the mass transport coefficient k_m and on the COD :

$$C_7H_6O_3 + 7O_2 \rightarrow 7CO_2 + 3H_2O \qquad\qquad 8.14$$
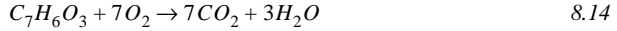
$$j_{lim}^0 = 4Fk_mCOD^0 \qquad\qquad 8.15$$

where j_{lim}^0 is the limiting current density (A m^{-2}) at a given time t, 4 the number of exchanged electrons, F the Faraday's constant (C mol^{-1}), k_m the mass transport coefficient (m s^{-1}) and COD^0 the initial chemical oxygen demand (mol m^{-3}).

The experimental conditions were chosen in order to investigate the oxidation reactions under both current control and mass transport control. All the experimental data were compared with the theoretical COD-ICE model (Chapter 3).

Figure 8.5 and Figure 8.6 show the evolution of COD and ICE, respectively, during the electrolysis of SA at two current densities (15.7 and 470 A m^{-2}).

The COD values exhibited a linear decrease with time under low current density condition (15.7 A m^{-2}) while the ICE remained almost equal to 1, as predicted by the theoretical model:

$$COD_{(t)} = COD^0 \left(1 - \frac{\alpha A k_m}{V_R} t \right) \qquad\qquad 8.16$$

where α is the ratio j_{appl} / j_{lim}, COD^0 is the initial COD (molO$_2$ m^{-3}), A is the electrode surface, k_m is the mass transfer coefficient (m s^{-1}), V_R is the cell volume (m^3) and t is the time (s).
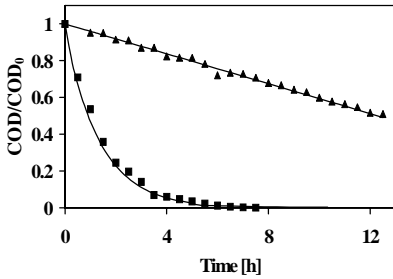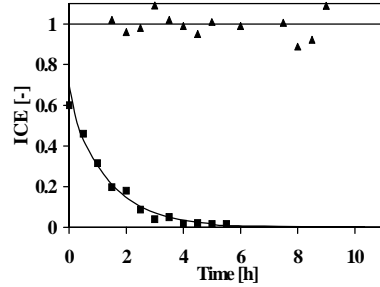
Figure 8.5 Evolution of COD as a function of time. SA oxidation at (▲) 15.7 A m^{-2}, (■) 470 A m^{-2} 1M HClO$_4$,T = 25°C. The solid lines represent the theoretical model. COD^0 = 50 mol O$_2$ m^{-3}.

Figure 8.6 Evolution of ICE as a function of time. SA oxidation at (▲) 15.7 A m^{-2}, (■) 470 A m^{-2} 1M HClO$_4$,T = 25°C. The solid lines represent the theoretical model. COD^0 = 50 mol O$_2$ m^{-3}.

In the second case (470 A m^{-2}), the reaction was controlled by mass transport. Both *COD* and *ICE* exhibited the same trend; an exponential decrease with time as predicted by the model (Equation 8.17, Equation 8.18):

$$COD_{(t)} = COD^0 \exp\left(-\frac{Ak_m}{V_R}t\right) \qquad\qquad 8.17$$

$$ICE = \frac{1}{\alpha}\exp\left(-\frac{Ak_m}{V_R}t\right) \qquad\qquad 8.18$$

According to the theoretical model, we can expect that, during the electrolysis at low current density, the oxidation reaction of SA is predominant against the side reactions leading to the formation of a lot of intermediates. In the opposite case, at high current density, the reaction is limited by the mass transport. Consequently, the direct combustion takes place nearly without intermediates formation.

In order to check these hypotheses and to validate the ν-γ model, the percentage of carbon dioxide and aromatics (2,3- and 2,5-DHBA) were calculated. Figure 8.7 represents the first step of SA oxidation into hydroxylated products: 2,3- and 2,5-dihydroxylated benzoic acid and catechol.
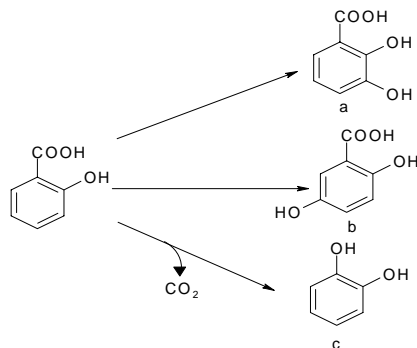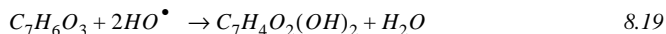
Figure 8.7 Scheme of salicylic acid hydroxylation (a) 2,3-DHBA, (b) 2,5-DHBA, (c) Catechol.

Typical results of *HPLC* analysis of the solution for the electrolysis carried out at low current density (15.7 A m^{-2}) are given in Figure 8.8. Under these conditions, it is assumed that the reaction implies 2 hydroxyl radicals (or 2 electrons):

$$C_7H_6O_3 + 2HO^{\bullet} \rightarrow C_7H_4O_2(OH)_2 + H_2O \qquad 8.19$$

In this case, according to the model (Chapter 3), γ is equal to 1.2 and ν is equal to 2. Under these conditions, the concentration of SA decreased linearly (Equation 8.19) with the specific charge, forming mainly 2,5- and 2,3-DHBA while the *TOC* remained constant.

$$[R] = [R]_0 - \frac{j_{app}A}{2FV}t \qquad 8.20$$

Figure 8.9 confirms the selective oxidation of SA into dihydroxylated intermediates. According to the model (Chapter 3), the percentage of aromatic intermediates formed was calculated at 60%, while the percentage of CO_2 formed was about 10%. Under these conditions, a longer electrolysis leads to a higher SA conversion, where aliphatic compounds and finally CO_2 are produced.
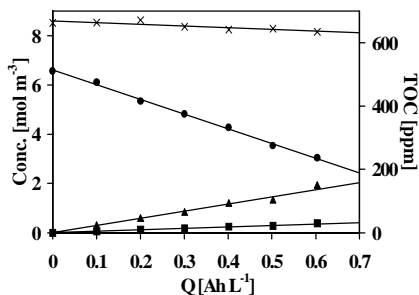
Figure 8.8 Variation of the concentration of (○) SA, (▲) 2,5-DHBA, (■) 2,3-DHBA and (✕) TOC during SA electrolysis. 1 M $HClO_4$, $[SA]_0$ = 6.56 mM, T = 25°C, γ =1.2, v = 2, j = 15.7 A m^{-2}. Solid lines represents model prediction for SA concentration.
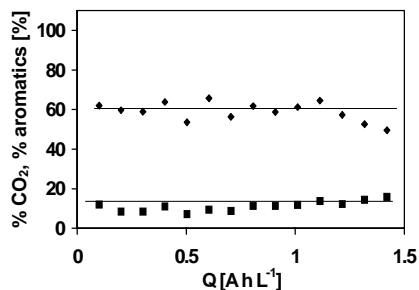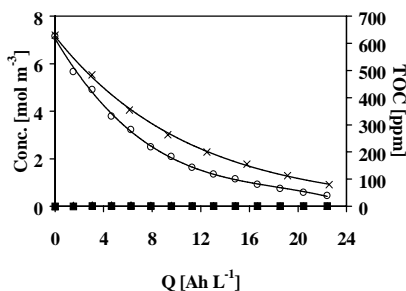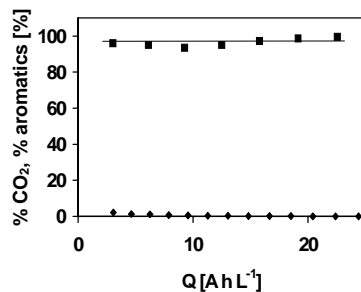
Figure 8.9 Trend of the percentage of (■) SA converted into CO_2 and (▲) SA converted to dihydroxylated compounds during SA electrolysis. 1 M $HClO_4$, $[SA]_0$ = 6.56 mM, T = 25°C, j = 15.7 A m^{-2}.

The results shown in Figure 8.10 were obtained during electrolysis at high current density (470 A m^{-2}).

Figure 8.10 Variation of the concentration of (○) SA, (▲) 2,5-DHBA, (■) 2,3-DHBA and (✕) TOC during SA electrolysis. 1 M $HClO_4$, $[SA]_0$ = 7.17 mM, T = 25°C, γ =34, v = 28, j = 470 A m^{-2}.

Figure 8.11 Trend of the percentage of (■) SA converted into CO_2 and (▲) SA converted to dihydroxylated compounds during SA electrolysis. 1 M $HClO_4$, $[SA]_0$ = 7.17 mM, T = 25°C, γ =34, v = 28, j = 470 A m^{-2}.

Under these conditions, SA was totally incinerated. The reaction implies 28 hydroxyl

radicals (or 28 electrons):

$$C_7H_6O_3 + 28HO^{\bullet} \rightarrow 7CO_2 + 17H_2O \qquad\qquad 8.21$$
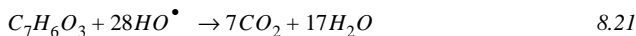
where γ is equal to 34 and ν is equal to 28 (Chapter 3). The similar evolution of SA and *TOC* concentrations confirms that complete combustion of SA occurred. The model for SA removal is in good agreement with experimental data. Confirming the complete combustion of SA to CO_2, the percentage of aromatic intermediates formed was less than 1%, while the percentage of CO_2 formed was about 100% (Figure 8.11).

Figure 8.12 represents the selectivity of 2,3 and 2,5-DHBA. A majority of 2,5-DHBA was produced.
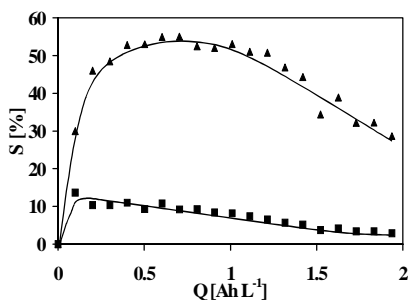

Figure 8.12 Selectivity of (▲) 2,5-DHBA and (■) 2,3-DHBA as a function of the specific charge Q. $[SA]_0 = 7.17$ mM, T = 25°C, j = 470 A m^{-2}.

We have observed that a large amount of aromatics was produced as intermediates at low current density. Therefore, the carbon molar balance was established at 15.7 A m^{-2}. Two main classes of products were expected: aromatic compounds having a similar structure to salicylic acid and aliphatic compounds formed by the cleavage of the benzenic ring. Figure 8.13 shows the evolution of the concentration of some aromatic intermediates: 2,3-, 2,4-, 2,5-DHBA, catechol and hydroquinone due to the presence of hydroquinone, benzoquinone was also detected during experiments. The major product detected was 2,5-DHBA.

Figure 8.14 exhibits the concentrations of aliphatic compounds. Four aliphatic intermediates were identified: formic, maleic, oxalic and fumaric acids. The higher

concentration was attributed to formic acid. This result is not surprising because formic acid is the last intermediate of the oxidation chain, just before the formation of CO_2 and H_2O.
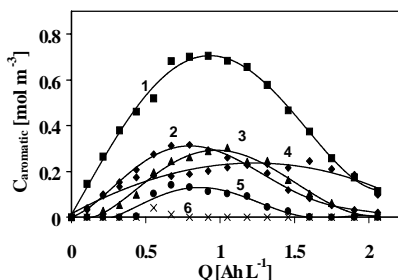

Figure 8.13 Concentrations of (1) 2,5-DHBA, (2) 2,3-DHBA, (3) catechol, (4) hydroquinone, (5) benzoic acid and (6) 2,4-DHBA as a function of specific charge Q. 1M $HClO_4$, T = 25°C, j= 15.7 A m^{-2}.
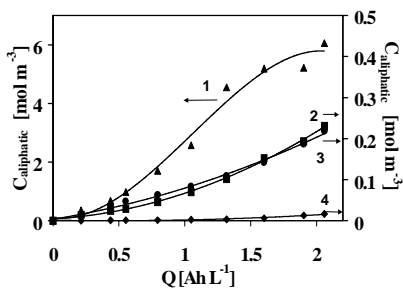
Figure 8.14 Concentrations of (1) formic acid, (2) maleic acid, (3) oxalic acid and (4) fumaric acid as a function of specific charge Q. 1M $HClO_4$, T = 25°C, j = 15.7 A m^{-2}.

Figure 8.15 represents the carbon molar balance taking into consideration the degradation of SA and the formation of aromatic intermediates, aliphatic compounds and finally carbone dioxide. According to our results, it was possible to propose a putative mechanism for SA oxidation (Figure 8.16).
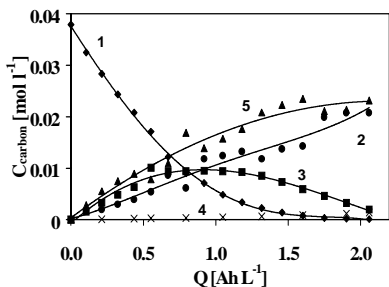

Figure 8.15 Carbon balance of (1) SA, (2) CO_2, (3) aromatics (4) aliphatics and (5) others as a function of specific charge Q. 1M $HClO_4$, T = 25°C, j= 15.7 A m^{-2}.
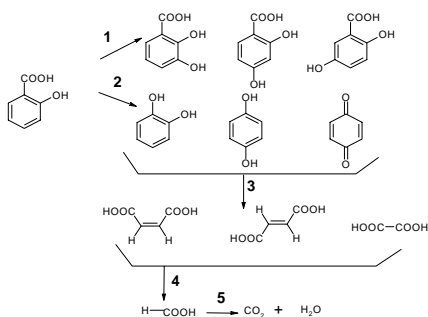
Figure 8.16 Possible mechanism of SA combustion.

The first step (1) consists in the hydroxylation reaction of SA by hydroxyl radicals, leading to the formation of dihydroxylated intermediates (2,3-, 2,4-DHBA and a majority of 2,5-DHBA). When decarboxylation takes place (2), catechol, hydroquinone and benzoquinone are mainly produced. The cleavage of the benzenic ring (3) forms aliphatic carboxylic acids such as maleic, fumaric and oxalic acids. Then the oxidation of these compounds leads to the formation of formic acid (4) and finally carbon dioxide and water (5).

3.2.1. Comparison with sulfuric acid

To investigate the possible effect of persulfate in the hydroxylation reaction, the electrolysis of salicylic acid was performed at three different temperatures (25, 60 and 70°C) in either 1 M $HClO_4$ or 1M H_2SO_4.

Sulfuric acid cannot be considered as an inert supporting electrolyte like perchloric acid. Indeed, in aqueous solution, sulfuric acid dissociates into hydrogen sulfate HSO_4^- and sulfate SO_4^{2-}. It is assumed that the hydrogen sulfate anion reacts with the hydroxyl radicals electrogenerated at BDD electrode to form a new sulfate radical:

$$HSO_4^- + HO^\bullet \rightarrow SO_4^{-\bullet} + H_2O \qquad\qquad 8.22$$
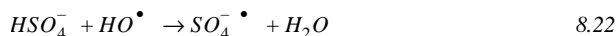
which then dimerize to form peroxodisulfate:

$$2SO_4^{-\bullet} \rightarrow S_2O_8^{2-} \qquad\qquad 8.23$$

Salicylic acid oxidation

The aim of this part was the investigation of the influence of the supporting electrolyte on the rate of SA oxidation and, to a lesser extent, to verify if the same selectivity in dihydroxylated product is observed.

All the experiments were carried out at 1 A (157 A m^{-2}) and at three different temperatures (25, 60 and 70°C). The concentration evolution shown in Figure 8.17 was recorded at 25°C. One can observe a slower decrease of the salicylic acid concentration in perchloric acid compared to sulfuric acid. The trend of the *COD* is shown in Figure 8.18 At this current density, the oxidation is under mixed control, where the *COD* decreases linearly and changes to an exponential time dependence, after a critical time. It is

interesting to correlate the production of persulfates from a sulfuric solution with the oxidation rate. Indeed, according to Figure 8.19, the highest concentration of persulfate is produced at the lowest temperature investigated (25°C). At this temperature, the oxidation of salicylic acid can also be performed in the bulk by the persulfates, a phenomenon which is not expected with perchloric acid.
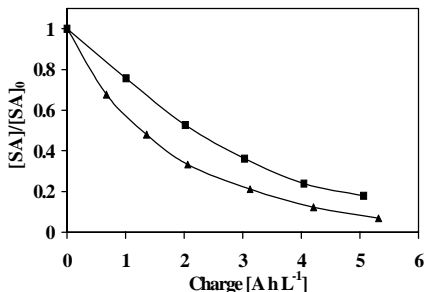

Figure 8.17 Evolution of SA concentration as a function of the specific charge during galvanostatic electrolysis in (▲) H_2SO_4, (■) $HClO_4$, T = 25°C, j = 157 A m^{-2}, $[SA]_0$ = 6 mM.
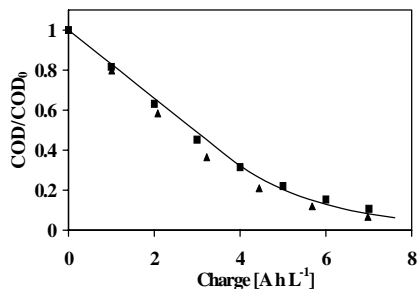
Figure 8.18 Evolution of the *COD* as a function of the specific charge. Electrolyte (▲) H_2SO_4, (■) $HClO_4$, T = 25°C, j = 157 A m^{-2}, $[SA]_0$ = 6 mM. The solid line represent the prediction of the theoretical model.
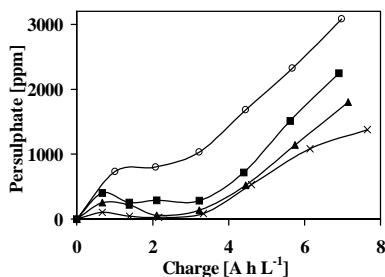

Figure 8.19 Persulfate production during galvanostatic electrolysis as a function of temperature. (○) 25°C, (■) 60°C, (▲) 70°C and (×) 80°C. j = 157 A m^{-2}.

A similar comparison between perchloric and sulfuric acid media was also made at higher temperature. Figure 8.20 and Figure 8.21 represent both the SA and COD

evolutions at 60°C. On the one hand, the oxidation of salicylic acid occurred more rapidly in both electrolytes compared to the previous experiment, and on the other hand, the oxidation in perchloric acid was also slightly faster. The increase of the reaction rate can only be assigned to the temperature increase, which speeds up the reaction and favor the formation of oxidizing intermediates.
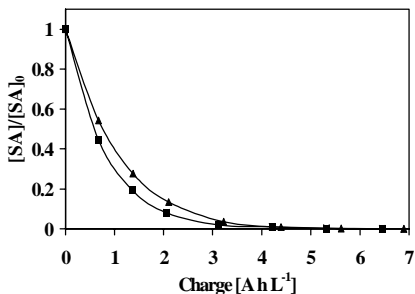

Figure 8.20 Evolution of the concentration of SA as a function of the specific charge. Electrolyte: (▲) H_2SO_4, (■) $HClO_4$, T = 60°C, j = 157 A m^{-2}. $[SA]_0$ = 6 mM.

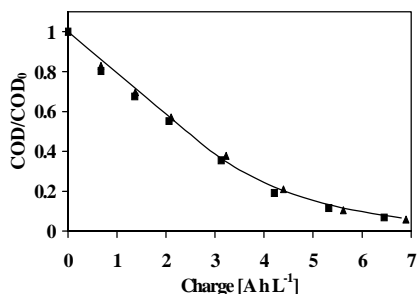**Figure 8.21** Evolution of the *COD* as a function of the specific charge. Electrolyte: (▲) H_2SO_4, (■) $HClO_4$, T = 60°C, j = 157 A m^{-2}. The solid line represent the prediction of the theoretical model. $[SA]_0$ = 6 mM.
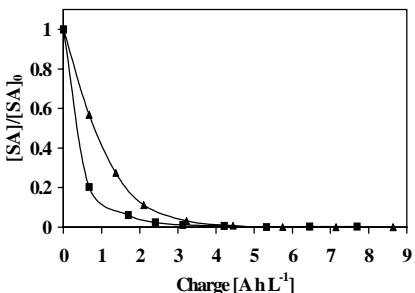
Figure 8.22 Evolution of the SA concentration. Electrolyte: (▲) H_2SO_4, (■) $HClO_4$, T = 70°C, j = 157 A m^{-2}. $[SA]_0$ = 6 mM.

Figure 8.23 Evolution of the COD. Electrolyte: (▲) H_2SO_4, (■) $HClO_4$, T = 70°C, j = 157 A m^{-2}. The solid line represent the prediction of the theoretical model. $[SA]_0$ = 6 mM.

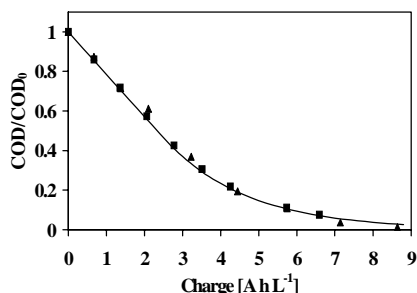At 70°C (Figure 8.22 and Figure 8.23), the oxidation in sulfuric acid remained almost

the same, while the oxidation in perchloric acid was once again faster.

At high temperatures, the oxidation of salicylic acid does not seem to be influenced by the presence of persulfates in solution. The decrease of persulfate with the increase of temperature (Figure 8.19) can be explained by the persulfate decomposition.

Figure 8.24 gives the result of the evolution of the concentrations of SA and 2,5-DHBA. The current density was high (higher than the limiting current) and, consequently, the conditions for the partial hydroxylation were not fulfilled. It was thus possible to observe some intermediates of the reaction. As seen in the previous experiments, 2,5-DHBA was formed as a by-product while the presence of 2,3-DHBA was not observed.
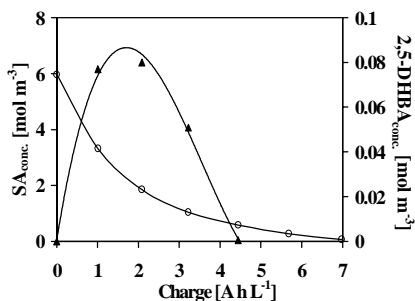
Figure 8.24 Variation of the concentration of ($\bigcirc$) SA and ($\blacktriangle$) 2,5-DHBA during SA electrolysis. 1M H_2SO_4, $[SA]_0$ = 6 mM, j = 157 A m^{-2}, T = 25°C.

The chemical oxidation of SA by addition of persulfate was performed step by step ($6.26 \cdot 10^{-4}$ mol every 6 minutes) at 70°C as shown in Figure 8.25 and Figure 8.26. The oxidation of salicylic acid resulted in the formation of a majority of 2,3-DHBA compared to 2,5-DHBA. This behavior is reminiscent of that observed with the chemical hydroxylation of salicylic acid in ortho position by both Fenton reaction and *UV*-photolysis.

Figure 8.25 Evolution of (○) SA concentration and (■) *COD* as a function of time. Chemical oxidation of SA with $K_2S_2O_8$, T = 70°C. $[SA]_0$ = 7.25 mM.

Figure 8.26 Evolution of (▲) 2,5-DHBA and (■) 2,3-DHBA as a function of time. Chemical oxidation of SA with $K_2S_2O_8$, T = 70°C. $[SA]_0$ = 7.25 mM.
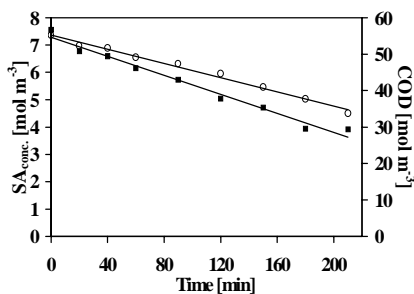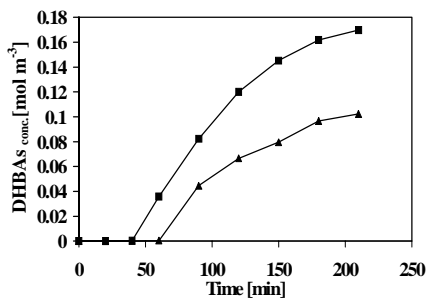
4. CONCLUSIONS

In this chapter, we have investigated the oxidation of salicylic acid in a two-compartments electrochemical flow cell. In spite of the difficulty to describe the hydrodynamic conditions of the cell (because of the existence of turbulence zones), it was possible to perform bulk electrolysis at BDD electrode and predict the evolution of the reaction.

From the measured value of the mass transfer coefficient, it was possible to compare the experimental data with the two theoretical models developed for BDD electrode. Salicylic acid oxidation occurred through an indirect reaction involving electrogenerated hydroxyl radicals formed at the diamond anode by the water decomposition. As predicted by the *COD-ICE* model, we observed different regimes (current, mass transport or mixed controls) depending on the applied current density. Under current control, we observed the production of a large quantity of intermediates while at high current density, only few intermediates were formed. The γ–ν model, which takes into consideration both stoichiometric and kinetics parameters confirmed the predictions of the *COD-ICE* model. Indeed, when the reaction was under current control, a large percentage of aromatics were detected. On the contrary, mass transport control resulted in a high percentage of carbon dioxide as a result of the formation of a large amount of hydroxyl radicals relative to organics.

Through *HPLC* and *TOC* measurements, the carbon mass balance could be established and a mechanism for salicylic acid was proposed. This mechanism highlights the role of hydroxyl radicals in the formation of dihydroxylated intermediates as first by-intermediates.

Finally, the influence of the supporting electrolyte on the oxidation process was studied. It appeared that, except at ambient temperature, where the concentration of produced persulfate was maximum, the oxidation of salicylic acid is not faster in sulfuric acid than in perchloric acid. The intermediates during the oxidation process in sulfuric acid were also the dihydroxylated compounds with the same isomer distribution, namely, a majority of 2,5-DHBA. However, the chemical oxidation by persulfate gives a majority of 2,3-DHBA relative to 2,5-DHBA.

5. REFERENCES

[1]   P.-A. Michaud, *Comportement anodique du diamant synthétique dopé au bore*, *Thesis N°2595*. 2002, EPFL, Lausanne.

[2]   M.A. Leveque, *Ann. Mines*, **12-13** (1928) 201.

[3]   I.M. Kolthoff, A.I. Medalia, and H.P. Raaen, *J. Am. Chem. Soc.*, **73** (1951) 1733.

[4]   K. Serrano, P.-A. Michaud, Ch. Comninellis, and A. Savall, *Electrochim. Acta*, **48** (2002) 431.

Chapter 9. Oxidation of salicylic acid using a new type of electrochemical cell (turbine cell)

1. INTRODUCTION

In this chapter, we will describe the electrochemical oxidation of salicylic acid using a new type of electrochemical cell, where well defined hydrodynamic conditions are established by stirring the electrolyte with a turbine. This enables us to control the mass transfer of the species during bulk electrolysis.

In a first step, a theory based on the resolution of the convective-diffusion equation was developed to determine hydrodynamic parameters and predict the mass transfer coefficient. Then, the optimization of the cell was made by determining the optimal operating conditions such as the domain of the angular velocity, the organic concentration and the position of the turbine according to the validity domain of Levich equation. After, the mass transfer coefficient k_m of the electrochemical cell was measured with the ferri/ferro system.

Finally, the oxidation of salicylic acid was studied by the measure of global parameters (*COD* and *ICE*) and the comparison of experimental data with the theoretical model. The mechanism of the reaction was investigated by the study of the intermediates produced during the reaction and the isomer distribution.

2. THEORETICAL PART

2.1. Turbine electrochemical cell

Hydrodynamic methods concern all the methods involving the convective mass transport of reactants and products. The main advantage is that a steady state is quickly reached, resulting in a high precision of the measurements.

The principal interest of the use of well defined hydrodynamic conditions in electrochemical systems is the possibility to predict the performance of the system when the mass transport is the rate determining step. There are mainly two types of hydrodynamics methods: (1) the electrode induces a flow in the cell by its rotation (classical RDE, vibrating electrode, streaming Hg electrode) and (2) the flow is forced over the electrode surface whilst the electrode is stationary (channel, microjet or wall jet electrode) [1, 2]. Rotating disk electrode has been widely used (to establish well defined hydrodynamic conditions) but this system has some limitations namely blocking of the surface due to bubble formation and electrode manufacturing. While they were studying, Landolt *et al.* [3] developed a new cell for inverted rotating disk electrode in order to avoid problems due to the bubbles but could not solved all the problems. Furthermore, in our case, the manufacturing of a RDE based on diamond is not easy. These considerations have motivated the development of the turbine cell.

In this work, we have developed the hydrodynamic theory for the turbine cell. In this configuration, the electrode is stationary while the flow is induced over the electrode. The turbine electrochemical cell is described in Chapter 4.

The treatment of the turbine cell is based on the diffusion layer approach. We made the assumption that the convection maintains the concentrations of all species uniform and equal to the bulk values beyond a distance δ (very thin layer) from the electrode. Below this δ value, no solution movement takes place and mass transfer occurs by diffusion. Then, the convection problem can be dealt with a diffusion approach. However, it is more rigorous to consider a convective-diffusion approach and the velocity profiles

in solution.

Mass balance [4]

Considering the species *j,* the general equation for the flux of species, *Jj,* can be defined by the convective-diffusion equation (Equation 9.1):

$$J_j = -D_j \nabla C_j - \frac{z_j F}{RT} D_j C_j \nabla \phi + C_j \vec{v} \qquad 9.1$$

In this equation, the first term represents the diffusion, the second the migration and the last the convection. The diffusion term is obtained by the first Fick's law. The concentration gradient in the electrolyte creates the flux. Close to the electrode, only the molecular diffusion is considered. The migration term corresponds to the motion due to the ionic conduction. The last term reveals the macroscopic movement of the species *j*, where $\vec{v}$ represents the motion of the solution. When the solution contains an excess of supporting electrolyte, the ionic migration term can be neglected and the relation can be simplified as:

$$J_j = -D_j \nabla C_j + C_j \vec{v} \qquad 9.2$$

Considering the total variation of the particles number and the mass conservation, one can write:

$$\int_V \frac{\partial C_j}{\partial t} dV = -\int_S J_j dS \qquad 9.3$$

This relation can also be written as:

$$\int_V \frac{\partial C_j}{\partial t} dV = -\int_S -\text{div} J_j dV \qquad 9.4$$

Assuming a very small volume, the variation of C_j with time can thus be written as:

$$\frac{\partial C_j}{\partial t} = -\text{div} J_j = -\nabla \cdot v \qquad 9.5$$

Considering that the flux of the species D_j is not a function of the coordinates, we can define, by combination of Equation 9.3 and Equation 9.5, the equation describing the general convective-diffusion relation (Equation 9.6):

$$\frac{\partial C_j}{\partial t} = D_j \nabla^2 C_j - v \nabla C_j \qquad\qquad 9.6$$

For symmetry reasons (because the symmetry axis passes through the turbine axis and in the middle of the electrode), the cylindrical coordinates (Figure 9.1) are appropriate. In these coordinates, the equation becomes the general diffusion convective equation:

$$\frac{\partial C_j}{\partial t} = D_j \left[\frac{\partial^2 C_j}{\partial y^2} + \frac{\partial^2 C_j}{\partial r^2} + \frac{1}{r}\frac{\partial^2 C_j}{\partial r^2} + \frac{1}{r^2}\frac{\partial^2 C_j}{\partial \varphi^2} \right] - \left[v_r \frac{\partial C_j}{\partial r} + \frac{v_\varphi}{r}\frac{\partial C_j}{\partial \varphi} + v_y \frac{\partial C_j}{\partial y} \right] \qquad 9.7$$

Determination of the velocity profile [4]

Considering the Navier Stockes equation (Equation 9.8) and the continuity equation (Equation 9.9), it is possible to develop the velocity profile, assuming that the hydrodynamic equations are under steady state conditions.

$$\rho \frac{d\vec{v}}{dt} = -\vec{\nabla} P + \mu \vec{\nabla}^2 \vec{v} + \vec{f} \qquad\qquad 9.8$$

The first term is the pressure force, the second the viscosity forces and the last corresponds to the gravity force.

$$\nabla \cdot \vec{v} = 0 \qquad\qquad 9.9$$

The resolution can be made through cylindrical coordinates because one can consider a symmetry axis at the center of the electrode (Figure 9.1).

The regime is considered permanent and the gravity force is considered as negligible. Therefore Equation 9.8 becomes:

$$-\vec{\nabla} P + \mu \vec{\nabla}^2 \vec{v} = 0 \qquad\qquad 9.10$$
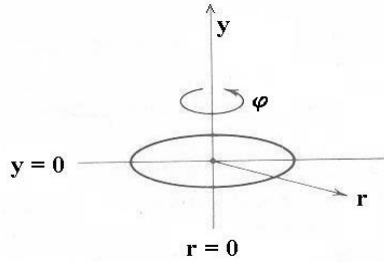
Figure 9.1 System of cylindrical coordinates (y, r, φ).

According to the system described in Figure 9.1, we can write the Navier Stockes equation (Equation 9.8) according to the radial, tangential and axial directions:

$$\frac{v_\varphi}{r}\frac{\partial v_r}{\partial \varphi} + v_r\frac{\partial v_r}{\partial r} + v_y\frac{\partial v_r}{\partial y} - \frac{v_\varphi^2}{r} = -\frac{1}{\rho}\frac{\partial P}{\partial y} + \mu\left(\frac{\partial}{\partial r}\left(\frac{1}{r}\frac{\partial}{\partial r}(rv_r)\right) + \frac{1}{r^2}\frac{\partial^2 v_r}{\partial \varphi^2} - \frac{2}{r^2}\frac{\partial v_\varphi}{\partial \varphi} + \frac{\partial^2 v_r}{\partial y^2}\right)$$ *9.11*

$$\frac{v_\varphi}{\varphi}\frac{\partial v_\varphi}{\partial \varphi} + v_r\frac{\partial v_\varphi}{\partial r} + \frac{v_r v_\varphi}{r} + v_y\frac{\partial v_\varphi}{\partial y} = -\frac{1}{\rho r}\frac{\partial P}{\partial \varphi} + \mu\left(\frac{\partial}{\partial r}\left(\frac{1}{r}\frac{\partial}{\partial r}(rv_\varphi)\right) + \frac{1}{r^2}\frac{\partial^2 v_\varphi}{\partial \varphi^2} + \frac{2}{r^2}\frac{\partial v_r}{\partial \varphi} + \frac{\partial^2 v_\varphi}{\partial y^2}\right)$$ *9.12*

$$\frac{v_\varphi}{r}\frac{\partial v_y}{\partial \varphi} + v_r\frac{\partial v_y}{\partial r} + v_y\frac{\partial v_y}{\partial y} = -\frac{1}{\rho}\frac{\partial p}{\partial y} + \mu\left(\frac{1}{r}\frac{\partial}{\partial r}\left(r\frac{\partial v_y}{\partial r}\right) + \frac{1}{r^2}\frac{\partial^2 v_y}{\partial \varphi^2} + \frac{\partial^2 v_y}{\partial y^2}\right)$$ *9.13*

and the continuity equation (Equation 9.9) becomes:

$$\frac{1}{r}\frac{\partial v_\varphi}{\partial \varphi} + \frac{\partial v_r}{\partial r} + \frac{v_r}{r} + \frac{\partial v_y}{\partial y} = 0$$ *9.14*

It is necessary to make some assumptions for boundary conditions:

• at the electrode surface, the solution has the same velocity than the turbine and is driven with an angular velocity ω, $v_y = 0$, $v_r = 0$ and $v_\varphi = \omega r$ (where r is the electrode radius).

• in the bulk, far from the electrode, the flow is directed toward the electrode direction and is parallel to the symmetry axis with a limiting velocity U_0 and $v_r = 0$, $v_\varphi = 0$. When y $\rightarrow \infty$, $v_y = - U_0$ (Figure 9.2).

• the pressure is considered as constant

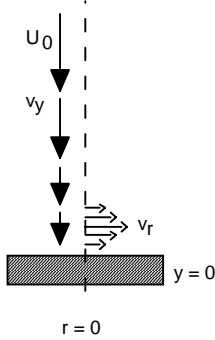• for symmetry considerations, all derivatives compared to φ are neglected

Figure 9.2 Vector representation of fluid velocities near the electrode.
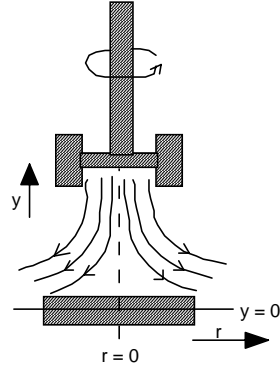
Figure 9.3 Schematic resultant streamlines.

Consequently, Navier Stockes can be simplified as:

$$v_r \frac{\partial v_r}{\partial r} + v_y \frac{\partial v_r}{\partial y} - \frac{v_\varphi^2}{r} = \mu \left(\frac{\partial^2 v_r}{\partial r} + \frac{1}{r} \frac{\partial v_r}{\partial r} - \frac{v_r}{r^2} + \frac{\partial^2 v_r}{\partial y^2} \right) \qquad 9.15$$

$$v_r \frac{\partial v_\varphi}{\partial r} + \frac{v_r v_\varphi}{r} + v_y \frac{\partial v_\varphi}{\partial y} = \mu \left(\frac{\partial^2 v_\varphi}{\partial r} + \frac{1}{r} \frac{\partial v_\varphi}{\partial r} - \frac{v_\varphi}{r^2} + \frac{\partial^2 v_y}{\partial y^2} \right) \qquad 9.16$$

$$v_r \frac{\partial v_y}{\partial r} + v_y \frac{\partial v_y}{\partial y} = \mu \left(\frac{\partial^2 v_y}{\partial r^2} + \frac{1}{r} \frac{\partial v_y}{\partial r} + \frac{\partial^2 v_y}{\partial y^2} \right) \qquad 9.17$$

Therefore, according the boundary conditions previously described, we can establish the relations for v_r and v_y by mathematical treatment of the Navier Stockes and continuity equations:

$$v_r = 0.51 r\omega \sqrt{\frac{\omega}{\mu}} y - \frac{r\omega^2}{2\mu} y^2 + \frac{0.616}{3} r\omega \left(\sqrt{\frac{\omega}{\mu}} \right)^3 y^3 \qquad 9.18$$

$$v_y = -0.51 \sqrt{\frac{\omega^3}{\mu}} y^2 + \frac{1}{3}\frac{\omega^2}{\mu} y^3 \qquad\qquad 9.19$$

From the adimensional number of Schmidt (Sc), it is possible to estimate the ratio between the thickness of the diffusion boundary layer δ and the hydrodynamic boundary layer δ_v, the ratio δ_v / δ being equal to $Sc^{1/3}$. For liquids, one can consider that the Schmidt number is higher than 10^3. Therefore, $\delta < (\delta_v / 10)$ and δ is considered as a part of δ_v.

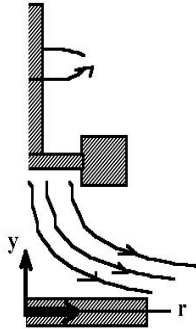According to the system of coordinates in the Figure 9.4:

Figure 9.4 Half-turbine cell.

the following profiles are obtained for v_y and v_r (Equation 9.20 and Equation 9.21.) Taking into consideration that a gradient of concentration exists only in the diffusion layer and that the hydrodynamic boundary layer is almost 10 times more sizeable than the diffusion one, we can only consider a little part of the velocity profiles corresponding to δ (Figure 9.5 and Figure 9.6).

Close to the electrode, only the first terms are considered and the velocities become:

$$v_r = 0.51 r\omega \sqrt{\frac{\omega}{\mu}} y = 0.51 \omega^{3/2} \mu^{-1/2} ry \qquad\qquad 9.20$$
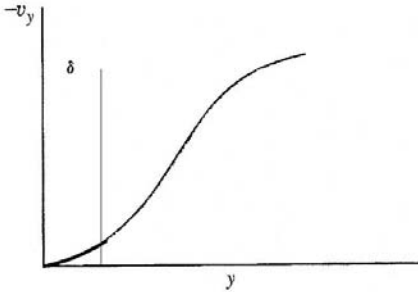
$$v_y = -0.51 \omega^{3/2} \mu^{-1/2} y^2 \qquad\qquad 9.21$$

Figure 9.5 Variation of the normal fluid velocity v_y as a function of y. δ is the diffusion boundary layer.
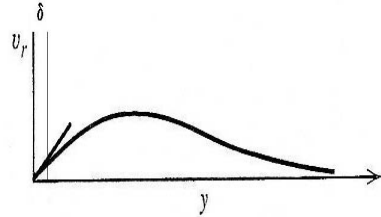
Figure 9.6 Variation of the radial fluid velocity v_r as a function of y. δ is the diffusion boundary layer.

Convective-diffusion equation

It is now possible to solve the convective-diffusion equation. We have already seen the equation in cylindrical coordinates:

$$\frac{\partial C_j}{\partial t} = D_j\left[\frac{\partial^2 C_j}{\partial y^2} + \frac{\partial^2 C_j}{\partial r^2} + \frac{1}{r}\frac{\partial^2 C_j}{\partial r^2} + \frac{1}{r^2}\frac{\partial^2 C_j}{\partial \varphi^2}\right] - \left[v_r\frac{\partial C_j}{\partial r} + \frac{v_\varphi}{r}\frac{\partial C_j}{\partial \varphi} + v_y\frac{\partial C_j}{\partial y}\right] \qquad 9.22$$

Assuming that:

• close to the electrode, the concentration of the species is time-independent, $\dfrac{\partial C_j}{\partial t} = 0$
(the velocity profile becomes stable with the agitation influence)

• v_y is independent of r, $\dfrac{\partial C_j}{\partial r} = 0$

• C_j is independent of v_φ because of the symmetry, $\dfrac{\partial C_j}{\partial \varphi} = \dfrac{\partial^2 C_j}{\partial \varphi^2} = 0$

Equation 9.22 can be simplified as:

$$v_y\left(\frac{\partial C_j}{\partial y}\right) = D_j\frac{\partial^2 C_j}{\partial y^2} \qquad 9.23$$

By combination with Equation 9.21, one obtains

$$-0.51\omega^{3/2}v^{-1/2}y^2\left(\frac{\partial C_j}{\partial y}\right) = D_j\frac{\partial^2 C_j}{\partial y^2} \tag{9.24}$$

which can be written as follows:

$$\frac{-y^2}{B}\left(\frac{\partial C_j}{\partial y}\right) = \frac{\partial^2 C_j}{\partial y^2} \quad (B = cst) \tag{9.25}$$

By integrating twice, this equation becomes:

$$C_j^* = \left(\frac{\partial C_j}{\partial y}\right)_{y=0} 0.8934\left(\frac{3D_j\omega^{-3/2}v^{1/2}}{0.51}\right)^{1/3} \tag{9.26}$$

The limiting current is equal to the flux at the electrode surface as:

$$I_{lim} = nFAD_j\left(\frac{\partial C_j}{\partial y}\right)_{y=0} \tag{9.27}$$

Combining Equation 9.27 with Equation 9.26, the limiting current can be defined as:

$$I_{lim} = 0.62nFAD_j^{2/3}\omega^{1/2}v^{-1/6}C_j^* \tag{9.28}$$

Diffusion boundary layer

The mass transport coefficient k_m can also be related to the diffusion boundary thickness (δ) [5] using the diffusion layer approach.

Indeed, k_m is directly related to δ:

$$J_j = D_j\frac{C_j(\infty)}{\delta} = k_mC_j(\infty) \tag{9.29}$$

From the Equation 9.26, one can write:

$$J_j = 0.622D_j^{2/3}\omega^{1/2}v^{-1/6}C_j(\infty) \tag{9.30}$$

and therefore

$$k_m = 0.622D_j^{2/3}\omega^{1/2}v^{-1/6} \tag{9.31}$$

From the previous equations, it is possible to give the following relation describing δ:

$$\delta = 1.61D_j^{1/3}\omega^{-1/2}v^{1/6} \tag{9.32}$$

3.   EXPERIMENTAL

3.1. Determination of the mass transport coefficient k_m

The mass transfer coefficient k_m was determined with an equimolar mixture of the redox couple ferri/ferro cyanide (10, 20, 60 and 100 mM) in 1 M NaOH. It is possible to calculate k_m with the measurement of the limiting current according to the following relation:

$$k_m = \frac{j_{lim}}{nFAC} \qquad\qquad 9.33$$

The limiting current was measured by linear sweep voltammetry for different equimolar concentrations of $Fe(CN)_6$ III/II at an angular velocity of 400 rpm.

3.2. Selectivity and conversion

The selectivity for the hydroxylated intermediates (S), relative to the amount of converted salicylic acid and the conversion of SA (X) have been defined as:

$$S_{2,3\text{-DHBA}} = \frac{[2,3\text{-}DHBA]_t - [2,3\text{-}DHBA]_0}{[SA]_0 - [SA]_t} \times 100 \qquad\qquad 9.34$$

$$S_{2,5\text{-DHBA}} = \frac{[2,5\text{-}DHBA]_t - [2,5\text{-}DHBA]_0}{[SA]_0 - [SA]_t} \times 100 \qquad\qquad 9.35$$

$$X = \frac{[SA]_0 - [SA]}{[SA]_0} \times 100 \qquad\qquad 9.36$$

where $[DHBA]_0$ and $[DHBA]_t$ are the concentrations of 2,3- or 2,5-dihydroxylated acids at time 0 and t, respectively (mol m^{-3}) and $[SA]_0$ and $[SA]_t$ the concentrations of salicylic acid at time 0 and t, respectively (mol m^{-3}).

3.3. *HPLC* measurement

The concentrations of products were monitored by *HPLC* on a chromatograph LC-2010A (Shimadzu Corporation, Kyoto, Japan) with *UV* detection. An apolar reversed phase column (silica particles) Nucleosil 7 C8 25 cm x 4.6 mm (HPLC Technology,

Macherey Nagel, Macclesfiel Cheshire, UK) was used to detect the following aromatic compounds: salicylic acid, 2,3-, 2,4- and 2,5-DHBA. Retention times are given in Table 9.1. The mobile phase was a polar mixture of 80/20 water-H_3PO_4 1%/acetonitrile. The elution was performed at an isocratic flow rate of 0.5 mL min^{-1} and at ambient temperature. The injection volume of the samples was 10 µL. The wavelength used for the detection was $\lambda = 296$ nm.

Compounds	Formula	C8 column Retention time [min]
Salicylic acid	$C_7H_6O_3$	13.69
2,3-DHBA	$C_7H_6O_4$	7.18
2,5-DHBA	$C_7H_6O_4$	6.42

Table 9.1 Structure and retention times of detected intermediates.

4. RESULTS AND DISCUSSION

4.1. Optimization of the turbine electrochemical cell

This study concerns the characterization of the turbine electrochemical cell. The design of the cell is presented in Chapter 4. It order to establish the best hydrodynamic conditions, it is necessary to take into consideration the agitation parameters. The aim of this investigation was to validate the appropriate operating domain. The results were compared with both RDE under similar conditions and the Equation 9.28. In order to define the mass transport coefficient of the cell, three parameters were investigated: the angular velocity, the electrolyte concentration and the position of the turbine.

4.1.1. Influence of the angular velocity

The limiting current of a $Fe(CN)_6$ III/II 20 mM equimolar solution was measured between 0 and 0.5 V for 13 angular velocities ω (from 200 to 800 rpm with 50 rpm steps). Figure 9.7, presenting the I-E graph for all ω values, points out the increase of the limiting current with ω. The same measurements (data not shown) performed with RDE gave similar results. As determined in the theoretical part (Equation 9.28), and according to the Levich relation, the variation of j_{lim} with $\omega^{1/2}$ has to be linear [6] and is given by the

following relation:

$$j_{lim} = 0.62nFD^{2/3}\omega^{1/2}v^{-1/6}C_0 \qquad\qquad 9.37$$

where n is the number of electrons ($n = 1$), F the Faraday's constant (96485 C mol^{-1}), D the diffusion coefficient of the redox couple ($5 \cdot 10^{-6}$ cm^2 s^{-1}), v the kinematic viscosity of water (0.01 cm^2 s^{-1}) and C_0 the concentration of Fe(CN)$_6$ (mol cm^{-3}).

This relation is showed in Figure 9.8. In order to validate the Levich equation for the turbine electrochemical cell, results were compared to those of the rotating disk electrode. Both exhibited a linear variation of j_{lim} vs $\omega^{1/2}$. With regard to Figure 9.8, it is possible to define precisely the validity domain of the Levich relation for rotating electrolyte (where no deviation with the rotating electrode exists). In our case, this domain was situated between 400 and 700 rpm (between 6.47 and 8.56 s$^{-1/2}$).
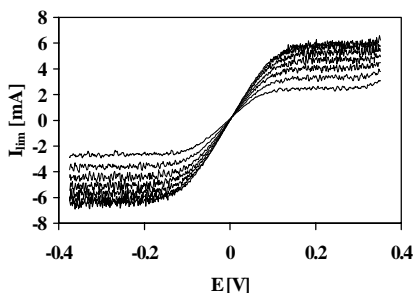

Figure 9.7 I-E graph as function of the angular velocity ω (200-800 rpm), Fe(CN)$_6$ III/II 20 mM in NaOH 1M, $v = 0.001$ V s^{-1}.
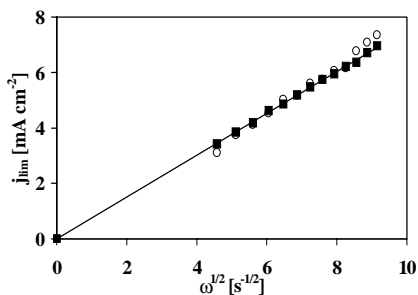
Figure 9.8 Relation j_{lim} vs $\omega^{1/2}$ (■)RDE, (○) Turbine cell. Fe(CN)$_6$ III/II 20 mM. The solid line represents Equation 9.37.

4.1.2. Influence of the electrolyte concentration

Equation 9.37 can be simplified, taking into consideration the mass transport coefficient k_m into [6]:

$$i_{lim} = nFAk_mC_0 \qquad\qquad 9.38$$

Measurements (Figure 9.9) of the limiting current as a function of the concentration

of the redox couple (from 0 to 100 mmol l^{-1}) were performed at a given angular velocity of 500 rpm (in the domain of validity of Equation 9.37). As for previous experiments, RDE results were compared to those of the turbine, and the Levich relation was validated on the entire concentration range (from 0 to 100 mM).

I-E measurements are useful to determine the mass transfer coefficient of the cell. The slope of the straight line (Figure 9.10) allowed us to calculate a mass transport coefficient k_m of $3 \cdot 10^{-5}$ m s^{-1}. The same value was obtained for an angular velocity of 400 rpm.
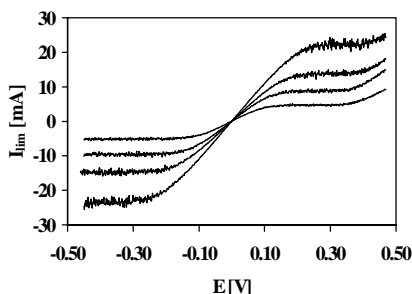

Figure 9.9 I-E graph as function of Fe(CN)$_6$ III/II concentration (10, 20, 60, 100 mM in NaOH 1M, ω = 500 rpm, ν = 0.001 V s^{-1}.
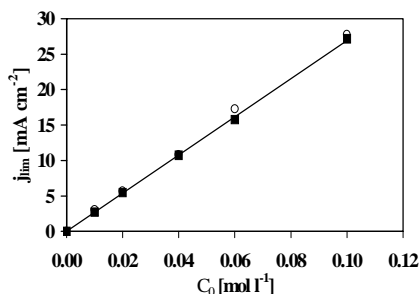
Figure 9.10 Relation j_{lim} vs C_0 (■) RDE, (○) Turbine cell. ω = 500 rpm. The solid line represents Equation 9.37.

4.1.3. Influence of the turbine position

The reaction of the redox couple was also investigated for different turbine positions (at the level of the extremity of the blade) relative to the working electrode (8, 13, 19, 27 and 31 mm). Figure 9.11 shows the relation between j_{lim} and $\omega^{1/2}$ for two turbine positions (8 and 31 mm). Positions 13 and 19 mm gave the same results than those of the 8 mm position. The pattern for the position 27 mm was similar to that of 31 mm position. According to the angular velocity range chosen (from 400 to 700 rpm), the validity of the model (Equation 9.37) is respected for distances lower than 27 mm.
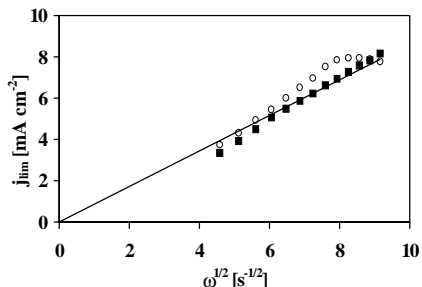
Figure 9.11 Relation j_{lim} vs $\omega^{1/2}$ for(■) 8 mm,(○) 31 mm. $\omega = 500$ rpm. The solid line represents Equation 9.37.

With respect to previous optimizations, the use of the turbine electrochemical cell is possible with well defined hydrodynamic conditions. Therefore, it seems appropriate to use this setup to induce an hydrodynamic flow and to investigate the response. Kralj *et al.* [2] investigated a rotating paddle cell, which can be compared to the turbine cell, and also found a good correlation with the Levich theory for rotating disk confirming the validity of this technique.

The following parameters were set up for the measurements with the turbine electrochemical cell: an angular velocity between 400 and 700 rpm, a maximum organic concentration of 100 mM, and a turbine position from 8 to 19 mm.

The diffusion coefficient $D_{Fe(CN)6\,II}$ was calculated as $5.3 \cdot 10^{-6}$ cm^2 s^{-1} ($5 \cdot 10^{-6}$ cm^2 s^{-1} in the RDE case). The mass transport coefficient k_m was defined as $3 \cdot 10^{-5}$ m s^{-1} (8 mm and 400 rpm).

## 4.2. Bulk electrolysis

The electrochemical oxidation of salicylic acid at boron-doped diamond is described by Equation 9.39:

$$C_7H_6O_3 + 11H_2O \rightarrow 7CO_2 + 28e^- + 28H^+ \qquad 9.39$$
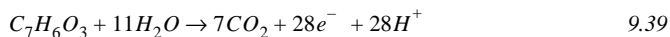
The values of total organic carbon (*TOC*), chemical oxygen demand (*COD*) and organics concentrations were measured for each assay. According to the three regimes of

oxidation: galvanostatic, mixed and diffusional, different currents were investigated (1, 5, 40 and 60 mA). The limiting current density, j_{lim}, can be expressed from the *COD* value (Equation 9.41).

$$C_6H_7O_3 + 7O_2 \rightarrow 7CO_2 + 3H_2O \qquad\qquad 9.40$$
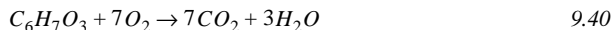
$$j_{lim}^0 = 4Fk_mCOD^0 \qquad\qquad 9.41$$

where j_{lim}^0 is the limiting current density (A m^{-2}) at a given time t, 4 the number of exchanged electrons, *F* the Faraday's constant (C mol^{-1}), k_m the mass transport coefficient (m s^{-1}) and COD^0 the initial chemical oxygen demand (mol m^{-3}).

The study focused on the formation of the main hydroxylated intermediates (2,3- and 2,5-dihydroxybenzoic acids) even if a carbon balance was established. The reactions were monitored by *HPLC* and *COD* measurements.

4.2.1. Salicylic acid oxidation

The oxidation of a 7.25 mM SA solution in 1M perchloric acid medium was carried out at four currents (from 1 to 60 mA). In the case of a 7.25 mM SA solution, the limiting current was found to be equal to 47 mA. Every 30 minutes, a sample was taken and analyzed. Figure 9.12 represents the decrease of salicylic acid concentrations during electrolysis at different current.

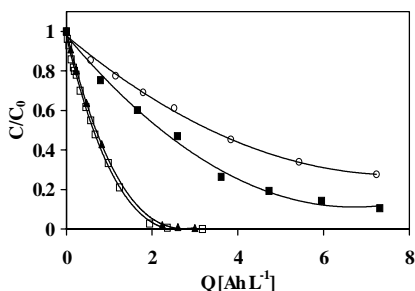**Figure 9.12**. Concentrations of SA as a function of specific charge Q. Electrolyte HClO$_4$ 1M, T = 25°C, (□) 1 mA, (▲) 5 mA, (■) 40 mA, (○) 60 mA. [SA]$_0$ = 7.25 mM.
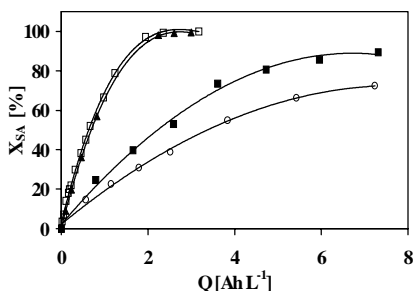
Figure 9.13 Conversion of SA as a function of specific charge Q. Electrolyte HClO$_4$ 1M, T = 25°C, (□) 1 mA, (▲) 5 mA, (■) 40 mA, (○) 60 mA. [SA]$_0$ = 7.25 mM.

For all investigated currents, the oxidation was complete and reached a total conversion. For the two lower currents (1 and 5 mA), the results of concentration and conversion evolution were the same (Figure 9.13). The values were normalized to the initial values to allow a correct comparison between all the experiments. Figure 9.14 and Figure 9.15 show the evolution of the chemical oxygen demand (*COD*) and the instantaneous current efficiency (*ICE*) for the oxidation of salicylic acid at 60 mA, respectively. The experimental data (points) were compared with theoretical values from the model (solid lines).

In the case of mass transport control ($j_{appl} > j_{lim}$), both *COD* and *ICE* decreased exponentially with Q as predicted by the model:

$$COD_{(t)} = COD^0 \exp\left(-\frac{Ak_m}{V_R}t\right) \qquad\qquad 9.42$$

$$ICE = \frac{1}{\alpha}\exp\left(-\frac{Ak_m}{V_R}t\right) \qquad\qquad 9.43$$

where α is the ratio j_{appl}/j_{lim}, A is the electrode surface (m^2), k_m is the mass transfer coefficient (m s^{-1}), V_R is the cell volume and t is the time (s).
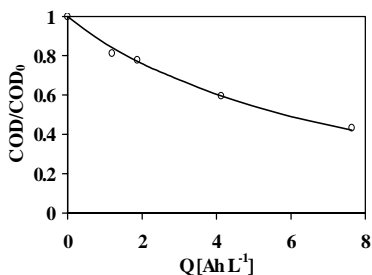

Figure 9.14 Evolution of the chemical oxygen demand (*COD*) during SA oxidation at 60 mA (mass transfer control) in HClO$_4$ 1M at BDD anode. Comparison between experimental data (points) and the theoretical model (solid lines). $COD^0 = 50$ mol O$_2$ m^{-3}.
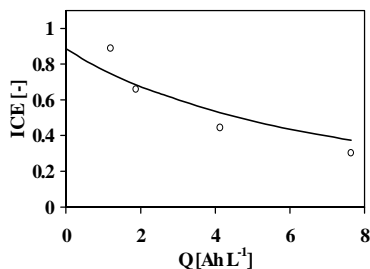
Figure 9.15 Evolution of the instantaneous current efficiency (*ICE*) during SA oxidation at 60 mA (mass transfer control) in HClO$_4$ 1M at BDD anode. Comparison between experimental data (points) and the theoretical model (solid lines). $COD^0 = 50$ mol O$_2$ m^{-3}.

In the case of current regime (5 mA), the applied current density is lower than the

limiting one and the evolution of *COD* is described by Equation 9.44:

$$COD_{(t)} = COD^0\left(1 - \frac{\alpha A k_m}{V_R}t\right)$$ *9.44*

Figure 9.16 and Figure 9.17 show the evolution of the chemical oxygen demand (*COD*) and the instantaneous current efficiency (*ICE*) for the oxidation of salicylic acid at 5 mA, respectively.

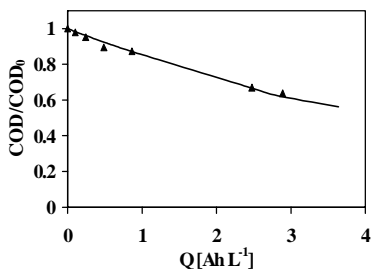The experimental data (points) were compared with theoretical values from the model (solid lines).

Figure 9.16 Evolution of the chemical oxygen demand (*COD*) during SA oxidation at 5 mA (current control) in HClO$_4$ 1M at BDD anode. Comparison between experimental data (points) and the theoretical model (solid lines). *COD^0* = 50 mol O$_2$ m^{-3}.
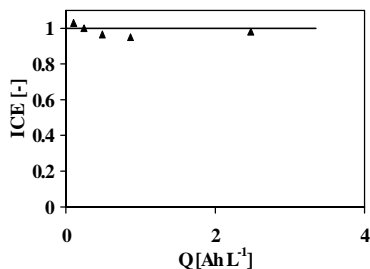
Figure 9.17 Evolution of the instantaneous current efficiency (*ICE*) during SA oxidation at 5 mA (current control)in HClO$_4$ 1M at BDD anode (turbine cell). Comparison between experimental data (points) and the theoretical model (solid lines). COD^0 = 50 mol O$_2$ m^{-3}.

COD decreased linearly with the specific charge whilst the *ICE* stayed almost equal to 1, meaning that all current was used for the SA oxidation and that there is no side reaction.

4.2.2. Intermediates formation (2,3- and 2,5-DHBA)

The reaction intermediates were monitored by *HPLC* in order to specify the reaction mechanism by identification of the intermediates and to evaluate the quantity of intermediates.
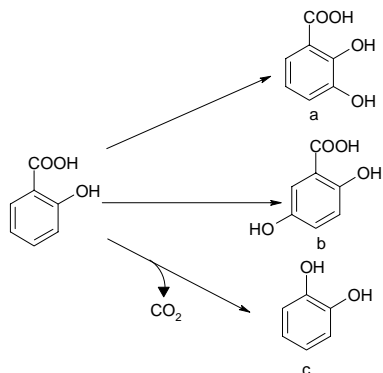
Figure 9.18 Salicylic acid hydroxylation (a) 2,3-DHBA, (b) 2,5-DHBA, (c) Catechol.

Figure 9.18 represents the first step of salicylic acid oxidation into hydroxylated products 2,3- and 2,5-dihydroxylated benzoic acid and catechol.

Depending on the imposed current, different concentrations of intermediates should be observed: high in the case of the partial oxidation and low when SA combustion takes place. The formation of the intermediates was evaluated in terms of concentration and selectivity. Figure 9.19 and Figure 9.20 summarize the concentrations recorded during bulk electrolysis at 1, 5, 40 and 60 mA. Only the main dihydroxylated intermediates were detected. As expected, the lower the current density, the higher the concentrations of the intermediates concentration. Indeed, the maximum concentrations were recorded at 1 mA for both 2,3- and 2,5-DHBA.

It is interesting to note that, irrespective of the current density, 2,5-dihydroxylated benzoic acid was the principal intermediate produced.

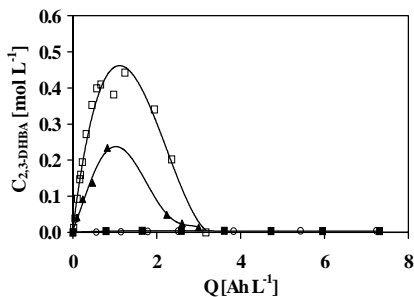**Figure 9.19** Concentrations of 2,3-DHBA as a function of the specific charge. Electrochemical oxidation of SA in HClO$_4$ 1M, T = 25°C, (□) 1 mA, (▲) 5 mA, (■) 40 mA, (○) 60 mA. [SA]$_0$ = 7.25 mM.
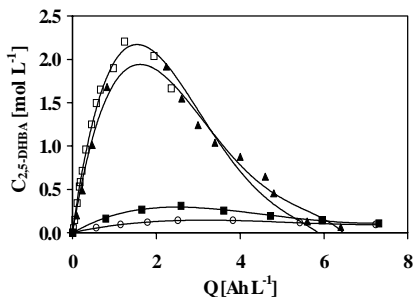
Figure 9.20 Concentrations of 2,5-DHBA as a function of the specific charge. Electrochemical oxidation of SA in HClO$_4$ 1M, T = 25°C, (□) 1 mA, (▲) 5 mA, (■) 40 mA, (○) 60 mA. [SA]$_0$ = 7.25 mM.
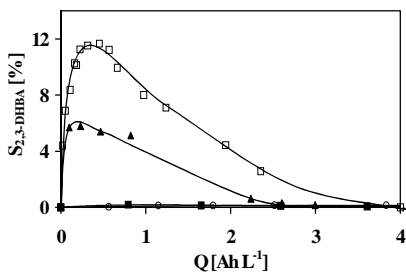
Figure 9.21 Selectivity of 2,3-DHBA (compared to SA removal) as a function of the specific charge Q. Electrochemical oxidation of SA in HClO$_4$ 1M, T = 25°C, (□) 1 mA, (▲) 5 mA, (■) 40 mA, (○) 60 mA. [SA]$_0$ = 7.25 mM.
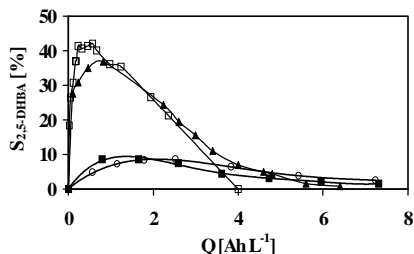
Figure 9.22 Selectivity of 2,5-DHBA (compared to SA removal) as a function of the specific charge Q. Electrochemical oxidation of SA in HClO$_4$ 1M, T = 25°C, (□) 1 mA, (▲) 5 mA, (■) 40 mA, (○) 60 mA. [SA]$_0$ = 7.25 mM

Figure 9.21 and Figure 9.22 represent the selectivity (compared to the quantity of SA consumed) for each intermediates (2,3- and 2,5-DHBA) and for four currents. As predicted by the theoretical model for electrochemical oxidation at BDD anode, it was possible to define two regimes (current control when the current is lower than the limiting current and mass transfer control in the opposite case) depending on the imposed current. In the current control domain (1 and 5 mA), partial oxidation was observed, leading to the

formation of a high quantity of intermediates. At higher current, total combustion of salicylic acid took place, forming only a few intermediates. These behaviors were confirmed by the values for the selectivity. The maximum selectivity for dihydroxylated acids was observed with the lower current, with a total percentage of 54% (42% for 2,5-DHBA and 12% for 2,3-DHBA), while at high current the total selectivity was equal to 8.74%.

5. CONCLUSIONS

This chapter deals with the development and the use of a new electrochemical cell, the turbine cell. In this set-up, the working electrode was fixed, while a turbine created the solution motion. This configuration permitted to investigate electrochemical reactions with well established hydrodynamic conditions. Indeed, this cell allowed a good control on the mass transport coefficient.

The theoretical development of the turbine cell was based on the diffusion layer approach and on the resolution of the convective diffusion equation. The optimization of the cell parameters was performed by comparison with the rotating disk electrode (using the Levich equation) and, the range of angular velocity, as well as the range of concentration, were defined. The position of the turbine with respect to the working electrode was also been studied in order to measure the mass transport coefficient k_m of the cell as well as the diffusion coefficient D for the ferri-ferro cyanide couple.

The turbine electrochemical cell was then used as electrochemical reactor for the salicylic acid oxidation at boron-doped diamond electrode. Bulk electrolysis were performed at different current densities in order to compare the experimental data with the theoretical model developed for the oxidation at BDD anode. The evolution of global parameters (*COD* and *ICE*) were in good agreement with the predictions of the model. The experimental data obtained with the turbine cell confirmed the validity of the theoretical model that was developed for a two-compartments electrochemical flow cell and for which a good mass transport is not always provided.

The analysis of the by-products of the SA oxidation has confirmed that, depending on the conditions of current, reactions of hydroxylation take place. Indeed, 2,3- and 2,5-dihydroxylated benzoic acids were detected as main intermediates. It is interesting to note that the second isomer (2,5-DHBA) is produced in majority during the reaction.

6. REFERENCES

[1]   J.A. Cooper and R.G. Compton, *Electroanal.*, **10** (3) (1998) 141.

[2]   B. Kralj and R.A.W. Dryfe, *Electrochem. Commun.*, **5** (2003) 325.

[3]   P.E. Bradley and D. Landolt, *J. Electrochem. Soc.*, **144** (6) (1997) L145.

[4]   F. Coeuret, *Ingénierie des procédés électrochimiques*, 2003, Ellipses, Paris.

[5]   J. Josserand, *Modélisation des processus de l'électrodéposition continue (approche couplée hydrodynamique et électrochimique*, *INPG*. 1994, Grenoble.

[6]   A.J. Bard and L.R. Faulkner, *Electrochemical methods - fundamentals and applications*, 2001, John Wiley & Sons, Inc, New York, 791.

Chapter 10. General Discussion

In this chapter, we will summarize the principal studies of this work. The first part concerns the electrochemical characterization of BDD anode, which was studied by different electrochemical techniques and compared with glasssy carbon electrode. Then, we will discuss the advantages of the turbine cell, a new electrochemical cell with well established hydrodynamic conditions.

As the mechanism of electrogeneration of hydroxyl radicals depends on the electrode material and the potential, it is primordial to distinguish between the region of water stability and that of oxygen evolution. Then, we will discuss the results concerning the detection of hydroxyl radicals at BDD anode, which was performed by investigating spin trapping reactions, hydrogen peroxide formation, competitive reaction and, finally, salicylic acid hydroxylation. The reactivity of hydroxyl radicals was underlined by investigating both chemical (Fenton and *UV*-photolysis) and electrochemical (at BDD electrode) hydroxylation of salicylic acid and with the study of the intermediates distribution. Theoretical models (*COD-ICE* and γ–ν models) will also be given to illustrate the role of hydroxyl radicals in the oxidation process at BDD electrode. Finally,

some perspectives will be proposed.

1. ELECTROCHEMICAL CHARACTERIZATION OF BBD ANODE

The electrochemical characterization of boron-doped diamond was performed (Chapter 5) using different electrochemical techniques (cyclic voltammetry, steady state polarization and rotating disk electrode). The redox couple investigated was violuric acid (Figure 10.1), an *outer-sphere* system.
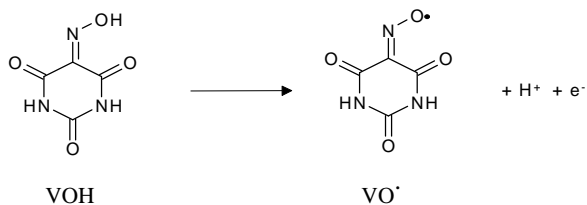
Figure 10.1 Scheme of the redox reaction of violuric acid.

The results were compared with a glassy carbon electrode in order to study the influence of sp^2 carbon. The experiments allowed to determine the key parameters (diffusion coefficient, anodic transfer coefficient and standard electrochemical rate constant) of the system. This investigation showed that, in spite of the use of techniques with different electrochemical approaches, the results remained relatively comparable. As regards to the results similar to those of glassy carbon, and considering the doping level of BDD (3000-4000 ppm of boron), we can assumed that BDD exhibits a quasi metallic character.

2. TURBINE CELL

In both one and two-compartments electrochemical cells (described in Chapter 4), we have shown that it exists some uncertainty concerning the hydrodynamic conditions. It is difficult to predict the mass transport coefficient because of the presence of local turbulences. In Chapter 9, a new type of electrochemical cell, called turbine cell, which presents some advantages, was developed. From the resolution of the convective diffusion equation, it has been possible to establish the hydrodynamic parameters, and to

predict the mass transfer coefficient. We obtained a good correlation with the rotating disk electrode, and consequently with the Levich equation. In this configuration, we can also consider only a small region close to the electrode for the determination of the hydrodynamic conditions. As explained in the theoretical part, the diffusion layer is lower than the hydrodynamic one by a factor of 10. Therefore, the gradient of concentration can be only considered in the diffusion layer, and a linear velocity profile can be considered (Chapter 9). This electrochemical cell proved to be an efficient cell for bulk electrolysis. The obtained selectivities in dihydroxylated intermediates were similar to those of two-compartments electrochemical flow cell. The predictive *COD-ICE* model was also validated for this reactor.

3. ELECTROGENERATION OF HYDROXYL RADICALS

Among the produced intermediates during anodic processes, hydroxyl radicals play a major role. In order to well understand their function, it is firstly essential to know their formation mechanism and reactivity, which depends on the electrode material. It is very important to distinguish between electrocatalytic material like platinum, *active* electrode like IrO_2 and *non active* material like BDD.

3.1. Production of OH radicals at Pt in the potential region of water stability

At platinum, a typical electrocatalytic material, the electrochemical oxygen transfer reaction (EOTR) is possible at very low potential. This reaction implies hydroxyl radicals, which are produced by two consecutive reactions: dissociative adsorption of water (Equation 10.1) followed by hydrogen discharge (Equation 10.2).

$$(H_2O)_{ads} \rightarrow (H^\bullet)_{ads} + (HO^\bullet)_{ads} \qquad\qquad 10.1$$

$$(H^\bullet)_{ads} \rightarrow H^+ + e^- \qquad\qquad 10.2$$
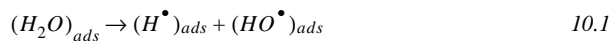
Hydroxyl radicals, formed during the first reaction, are strongly adsorbed at the platinum surface by strong chemical bonds. Then, the reaction with an organic takes place via either Eley-Rideal mechanism or that of Langmuir-Hinshelwood. The oxidation of

organic compounds is a process widely investigated. Between all the studies, the example of methanol is well described. The mechanism occurs via several steps of adsorption, dissociation of various intermediates. Among these adsorbed species, CO is the most problematic, which is responsible of the poisoning of the surface, phenomenon well known in electrocatalysis. To avoid the poisoning, it is necessary to improve the kinetics of the overall reactions. The addition of a second metal, on which water is more easily dissociated at lower potential can allow on the one hand to increase the adsorbed OH coverage and on the other hand to minimize the formation of CO species. The bifunctional mechanism for methanol oxidation is illustrated by Figure 10.2.
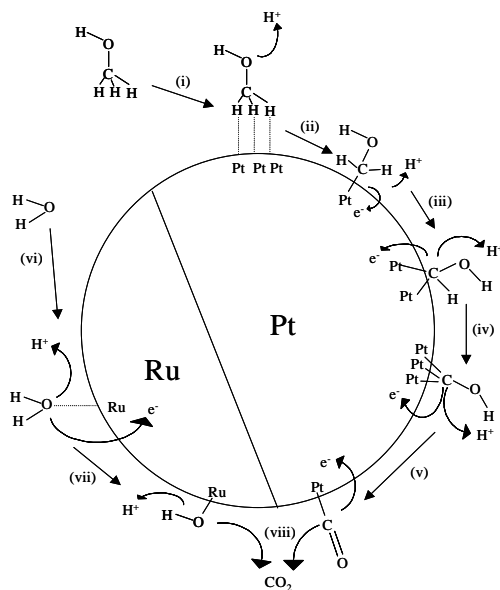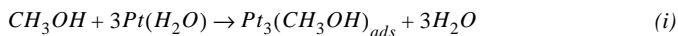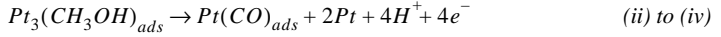

Figure 10.2 Reaction scheme of the possible methanol electrooxidation process at Pt-Ru electrode.

The first step is the electrosorption of methanol at platinum surface:

$$CH_3OH + 3Pt(H_2O) \rightarrow Pt_3(CH_3OH)_{ads} + 3H_2O \qquad (i)$$

Then, dehydrogenations take place in a fast reaction leading to Pt(CO)$_{ads}$:

$$Pt_3(CH_3OH)_{ads} \rightarrow Pt(CO)_{ads} + 2Pt + 4H^+ + 4e^- \qquad \text{(ii) to (iv)}$$

Adsorbed OH radicals are produced at rhutenium according to the following reaction:

$$Ru + H_2O \rightarrow Ru(OH)_{ads} + H_{aq}^+ + e^- \qquad \text{(vi) to (vii)}$$
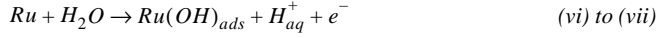
Finally, the reaction between $Pt(CO)_{ads}$ and $Ru(OH)_{ads}$ takes place via a Langmuir-Hinshelwood mechanism:

$$Pt - (CO)_{ads} + Ru(OH)_{ads} \rightarrow Pt + Ru + CO_2 + H_{aq}^+ + e^- \qquad \text{(viii)}$$
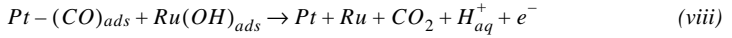
3.2. Production of OH radicals in the potential region of O_2 evolution

When the potential is higher than the thermodynamic potential of water decomposition in acidic medium (1.23 V vs SHE), another mechanism of OH radicals production has to be considered, where OH radicals are produced by water discharge (Equation 10.3) forming intermediates (mainly hydroxyl radicals) of oxygen evolution:

$$H_2O \rightarrow HO^\bullet + H^+ + e^- \qquad 10.3$$

The interaction between the surface electrode and hydroxyl radicals, which are physisorbed, depends on the electrode material. Two classes of material can be defined: *active* and *non active* electrodes. The differences between both mechanism are shown in the model (Figure 10.3). The common step is the discharge of water molecules to OH radicals (reaction a). At *active* electrodes, there is a strong interaction between the electrode (M) and hydroxyl radicals. The radicals may interact with the anode, with a possible oxygen transfer from hydroxyl radicals to the anode surface and the formation of an higher oxide (reaction b). Then, the surface redox couple (MO/M) can act as a mediator in the partial oxidation of organics (reaction c). This reaction is in competition with the oxygen evolution due to the decomposition of the higher oxide (reaction d).

At *non active* electrodes like diamond, there is a weak interaction between the electrode and hydroxyl radicals. The oxidation is therefore mediated by the radicals

(reaction e). The reaction is in competition with the concomitant oxygen evolution by hydroxyl radical discharge that takes place without any participation of the electrode surface.
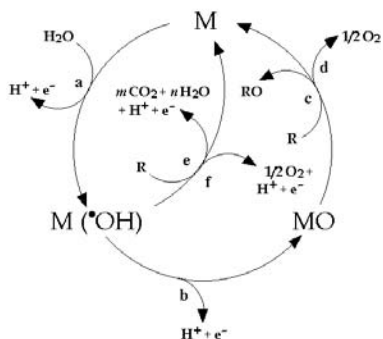
Figure 10.3 Scheme of the electrochemical oxidation of organic compounds on *active* anodes (reactions a, b, c, d) and on *non active* anodes (reactions a, e, f). M designates an active site at the anode surface.

4. DETECTION OF OH RADICALS AT BDD ELECTRODE

These three different mechanisms highlight the preponderant role of hydroxyl radicals in EOTR. Their presence was thus investigated at boron-doped diamond electrode and different experiments were performed in order to confirm the presence of these radicals.

4.1. Spin trapping

The direct detection of free hydroxyl radicals is difficult because of their short life time and low concentrations. Spin trapping, which consists into trapping a radical with a scavenger in order to produce a stable adduct, was performed at BDD electrode. The trapping of OH radicals was carried out by electrolyzing a solution of 5,5-dimethyl-1-pyrroline-N-oxide (DMPO). It was possible to record an electron spin resonance (*ESR*) spectrum (Figure 10.4), whose characteristics were typical of a DMPO-OH adduct ($a_N = a_H$ equal to 15 G). The spectrum was compared with that obtained with chemically produced hydroxyl radicals by Fenton reaction (Figure 10.5). Both spectra showed the

same hyperfine couplings.
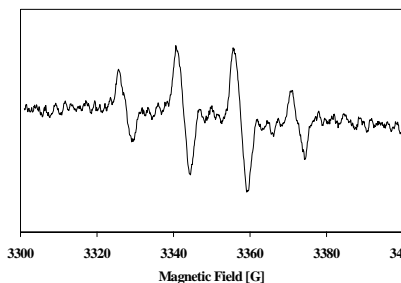
Figure 10.4 *ESR* spectrum of the DMPO-OH adduct obtained after electrolysis for 2 hours at BDD electrode. j = 0.1 mA cm^{-2}, T = 25°C.
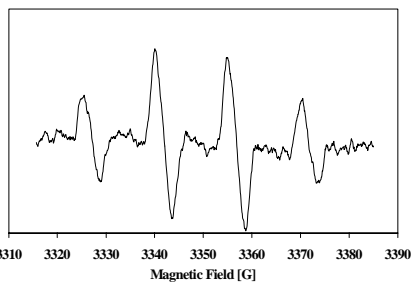
Figure 10.5 *ESR* spectrum of the DMPO-OH adduct obtained by Fenton reaction. T = 25°C.

A second spin trapping experiment was performed at BDD anode by performing an electrolysis of a solution of 4-nitroso-N,N-dimethylaniline (RNO) and measuring its *UV* absorbance (Figure 10.6).
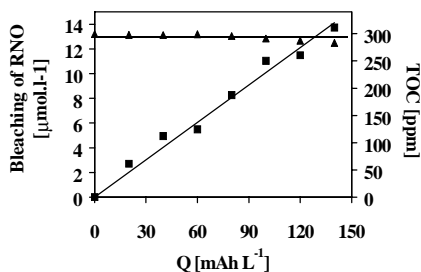
Figure 10.6 (■) Bleaching and (▲) *TOC* evolution of a 3.1 10^{-3} M RNO solution in 0.1 M borax medium as function of the specific charge. *j* = 20 mA cm^{-2}, T = 25°C.

We observed a decrease of the maximum of absorbance (at 440 nm), meaning that a reaction between hydroxyl radicals and RNO took place. The concentration of the total organic carbon remained constant, confirming that the bleaching of RNO could

exclusively be assigned to the reaction with hydroxyl radicals.

4.2. H$_2$O$_2$ formation and competitive reaction

The formation of hydrogen peroxide can be attributed to the combination of two hydroxyl radicals produced by the water discharge.

$$2HO^{\bullet} \rightarrow H_2O_2 \qquad\qquad 10.4$$

This production was investigated by performing different electrolysis at several current densities. The high concentrations of H$_2$O$_2$ produced increased with the current density, confirming the involvement of hydroxyl radicals.

From the observation of the oxygen evolution curves of formic and oxalic acids, we concluded to a different activity of the BDD electrode toward both organics. The electrolysis of a mixture of both compounds was thus performed, showing that formic acid oxidation occurs at first. An explanation for this behavior is that both organic compounds are in competition for hydroxyl radicals. The rate constant between OH radicals and formic acid is higher by two orders of magnitude than that of oxalic acid explaining the shift of potential oxidation and confirming the presence of hydroxyl radicals.

4.3. Salicylic acid hydroxylation

Aromatic hydroxylation, and especially salicylic acid hydroxylation, is often used to measure the production of hydroxyl radical because the hydroxylated intermediates are well defined [1-3]. The reaction between hydroxyl radicals and salicylic acid yields 2,3- and 2,5-dihydroxylated benzoic acid (Figure 10.7), and when decarboxylation occurs, catechol is produced.
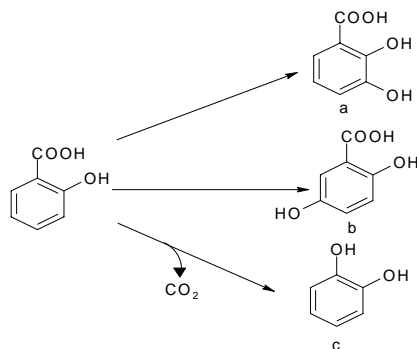
Figure 10.7 Mechanism of salicylic acid hydroxylation (a)
2,3-DHBA, (b) 2,5-DHBA, (c) Catechol.

The hydroxylation was performed at boron-doped diamond electrode in order to identify the produced intermediates. The reaction was compared with chemical hydroxylations of salicylic acid by Fenton reaction and *UV*-photolysis (Chapter 6). In all cases, the expected intermediates (2,3- and 2,5-DHBA) were produced with a total selectivity of 55%, 25% and 48%, respectively, confirming the presence of hydroxyl radicals.

5. REACTIVITY OF HYDROXYL RADICALS

As seen in the previous part, the mechanism of electrogeneration of hydroxyl radicals depends on the type of electrode material. Therefore, the reactivity of the radical is also different. On electrocatalytic materials like platinum, both OH radicals and organics have to be activated, resulting in a coadsorption. The chimisorption results in strong chemical bondings. On *active* and *non active* electrodes, hydroxyl radicals are produced by water discharge (Equation 10.3) and they are weakly adsorbed at the electrode surface. Zhi *et al.* have followed the oxidation of phenol by chronoamperometry [4]. They assumed that either direct electron transfer reaction at the surface electrode or indirect oxidation by mediation of electrogenerated intermediate occurred. Considering that the concentration of water is constant (and consequently that of hydroxyl radicals), the current should be independent of the organic concentration. On the contrary, if one consider a direct oxidation, the current should be dependent on the organic concentration. As regards to the

current increase during phenol oxidation, they concluded that the process can partially be attributed to a direct electrochemical oxidation at BDD surface.

It can be assumed that hydroxyl radicals react with organic compounds involving an electrochemical step (Equation 10.5). The hydroxylation at BDD electrode can thus be summarized by the following equation:

$$RH + HO^\bullet \rightarrow ROH + H^+ + e^-$$
10.5

The second step can also explain the shift of potential observed for the anodic overpotential when an organic is oxidized with concomitant oxygen evolution reaction at BDD anode. For example, the cases of formic and oxalic acids are presented in the following figures. In both cases, the anodic current curves are affected upon the addition of the organic. Indeed, the anodic potential decreases when the concentration of organics increases. This behavior is due to an important change in the electrochemical activity of BDD electrode. The direct reaction of OH radicals with organic compounds has for effect to decrease the overvoltage and,consequently, to shift the potential.
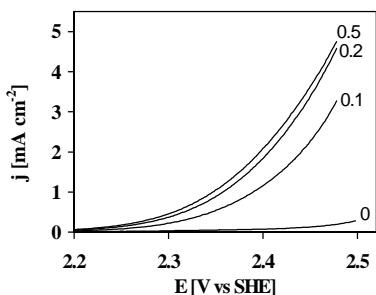
Figure 10.8 Effect of formic acid on the polarization curve for oxygen evolution at BDD electrode for 0, 0.1, 0.25 and 0.5 mol L^{-1}. $v = 50$ mV s^{-1}, T = 25°C.
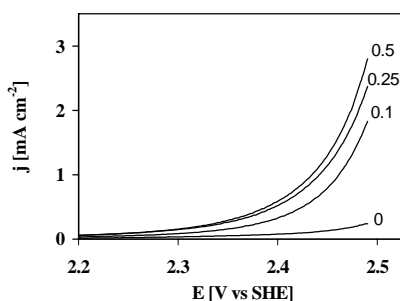
Figure 10.9 Effect of oxalic acid on the polarization curve for oxygen evolution at BDD electrode for 0, 0.1, 0.25 and 0.5 mol L^{-1}. $v = 50$ mV s^{-1}, T = 25°C.

5.1. Hydroxylation of salicylic acid at BDD electrode

Our previous results have shown that hydroxyl radicals were produced at boron-doped diamond electrode, we investigated their reactivity by studying the hydroxylation of salicylic acid (SA) and its hydroxylated intermediates (2,3- and 2,5-DHBA) (Figure

10.7).

The hydroxylation of SA was carried out at BDD electrode and the intermediates were quantified. The reaction was also performed with hydroxyl radicals produced chemically by Fenton reaction (H_2O_2 and Fe^{2+}) and *UV*-photolysis (H_2O_2 and *UV*). In all experiments, both 2,3- and 2,5-DHBA were found, as expected. However, we obtained a different isomer distribution depending on the production method of hydroxyl radicals (chemical or electrochemical) (Figure 10.10). In the case of chemical production, 2,3-DHBA (ortho isomer) was the majoritary product, while at BDD electrode, a majority of 2,5-DHBA (para isomer) was produced.
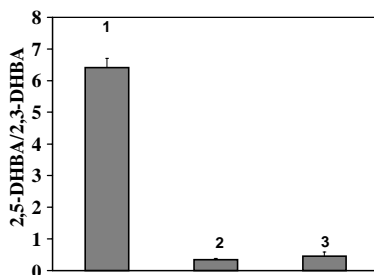
Figure 10.10 2,5-DHBA/2,3-DHBA ratios (1) electrochemical oxidation, (2) Fenton reaction, (3) *UV*-photolysis, $[SA]_0 = 7.25$ mM.

This inversion of isomer distribution was also observed with phenol, where hydroquinone was the main product of the electrochemical oxidation [5].

The mechanism of hydroxylation of phenol was widely studied. The OH radical exhibits a strong preference for the addition at the positions activated by the OH group, which is a strong activator in ortho and para positions. As regards to the resonance forms of phenol (Chapter 2), the OH radical is more likely to attack in the ortho position, because it exists two position ortho for one para. However, the hydroxylation reaction of phenol can theoretically produce three hydroxylated isomeric radicals (ortho, meta and para isomers, Figure 10.11) [6].
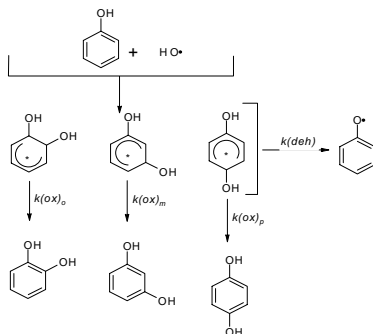
Figure 10.11 Hydroxylation and dehydratation reactions of phenol [6].

The oxidation reaction (leading to the formation of catechol, resorcinol or hydroquinone) is in competition with the dehydratation reaction (producing a phenoxyl radical). They found that $k(ox)_m/k(deh)_m < k(ox)_p/k(deh)_p < k(ox)_o/k(deh)_o$. Consequently, the fraction of $^{\bullet}$OH attacks at the ortho, meta and para positions of phenol were found to be equal to 48%, 8% and 36%, respectively. These results confirm the strong preference of the electrophilic OH radical for the ring positions activated by the phenolic OH group.

It is possible to make an analogy between phenol and salicylic acid, in which a concerted effect of OH (strong activator, orientating in ortho- and para-) and carboxyl (weak desactivator, orientating in meta-) substitutions exists [7]. Moreover, the formation of a intramolecular hydrogen bonding (between the hydroxyl group and the carbonyl) implies a geometry similar to that of phenol [8]. Therefore, the hydroxylation of salicylic acid should produce a majority of the ortho isomer (2,3-DHBA). This was confirmed by the results obtained upon hydroxylation by chemically produced OH radicals (Fenton reaction and *UV*-photolysis). In contrast, we showed that the isomer distribution is inverted (more 2,5- than 2,3-) upon electrochemical hydroxylation at BDD electrode. In the next part, we will propose some explanations concerning this inversion during electrochemical hydroxylation.

Influence of pH and stability of the hydroxylated products

The influence of pH has already been discussed (Chapter 3) [9]. The direction of the

OH attack could be modified by the pH, which could change the electronic density population (because of the presence of both carboxyl and hydroxyl groups). However, changing the pH did not have any impact on the isomer distribution. Irrespective of the pH, 2,5-DHBA was the major product of salicylic acid hydroxylation. Another factor was considered; the stability of each intermediates. No difference was observed in the stability and the rate of oxidation of both dihydroxylated intermediates. The isomer distribution can thus not be explained by the stability or by the decomposition kinetics of each intermediate.

Singlet oxygen $^1O_2$

Studies of Feix *et al.* [10] have shown that the singlet oxygen reacts with salicylic acid via the formation of an 1,2- or 2,5-endoperoxide. 1,2-endoperoxide is unstable and yields to ring opening while the 2,5-endoperoxide leads to the formation of 2,5-DHBA. Among the short-lived intermediates produced by water decomposition, singlet oxygen has been detected [11]. Therefore, the reaction between salicylic acid and singlet oxygen could occur at BDD electrode. However, it is likely that only a very low concentration of singlet oxygen is produced and, consequently, this phenomenon cannot explain the high concentrations of 2,5-DHBA observed. Moreover, the spin trap DMPO is known to give different *ESR* spectra depending on whether it reacts with OH radical or singlet oxygen. The *ESR* spectrum obtained with DMPO was relatively well defined. In conclusion, it is not excluded that a reaction between SA and $^1O_2$ exists, but this cannot explain the big difference of isomer distribution obtained upon chemical or electrochemical hydroxylation.

Steric effect

It has been concluded from biological experiments that the formation of 2,3-DHBA is a proof of the presence of free hydroxyl radicals while the formation of 2,5-DHBA arises from an enzymatic reaction. The investigation was made with the cytochrome P450, a coenzyme implicated in numerous metabolic oxidation mechanisms. Cytochrome P450 catalyzes either hydroxylation or epoxidation, where the formed intermediates are dictated by the direction of adsorption in the enzyme. It is possible to make an analogy with boron-doped diamond electrode, for which the preferential attack can also be

dictated by steric effect (in considering that the position 5 is the most accessible).

Mechanism of hydroxylation at BDD electrode

Hydroxyl radicals are electrochemically produced by the water discharge (Equation 10.3). The mechanism of hydroxylation can be described by the following global equation, which takes place between salicylic acid and the hydroxyl radical:

$$RH + HO^\bullet \rightarrow ROH + H^+ + e^- \qquad\qquad 10.6$$

Omura *et al.* [12] have investigated the hydroxylation of phenols by the photodecomposition of hydrogen peroxide and have proposed two possible mechanism for this reaction. The first one consists in an abstraction of hydrogen atom from the phenolic compound yielding a phenoxyl radical, followed by the addition of hydroxyl radical giving the hydroxylated product. The second pathway involves firstly the attack of the phenolic ring by OH radical forming a cyclohexadienyl radical, which is converted further abstraction of a hydrogen atom to the hydroxylated product. The last pathway is in agreement with the work of Raghavan *et al.* [6] (Figure 10.11). By analogy, we can propose a mechanism for hydroxylation of salicylic acid at boron-doped diamond electrode (Figure 10.12).

The first step is the water discharge at BDD electrode leading to the formation of hydroxyl radicals (reaction a). These radicals add to salicylic acid forming a cyclohexadienyl radical (reaction b). According to structural considerations, OH radicals can attack the salicylic acid in position 3 and 5 (ortho an para positions toward the hydroxyl group). Then, the abstraction of an hydrogen atom is performed by an electrochemical step (reaction c), which yields to the formation of dihydroxylated intermediates (2,3- and 2,5-dihydroxybenzoic acid).
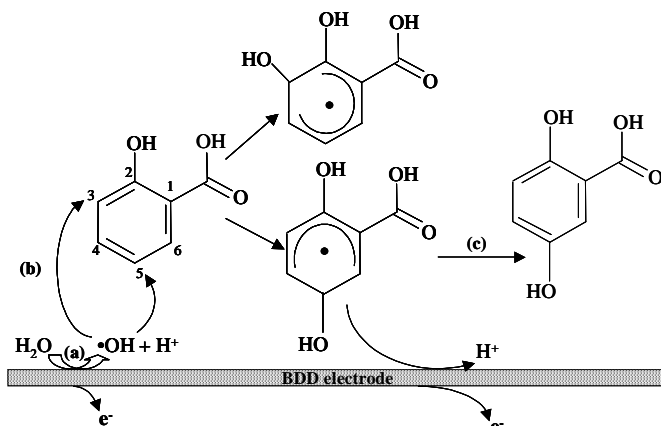
Figure 10.12 Hydroxylation of salicylic acid.

The hydroxylation occurs in the reaction cage (a region very close to the diamond surface electrode), where hydroxyl radicals are electrogenerated, and can then react with salicylic acid. We can consider that, because of steric effect, the hydroxylation is easier in position 5 (ortho-position), yielding a majority of 2,5-DHBA (Figure 10.12). It is also possible to take into consideration the nature of the oxidant, which dictates the distribution of isomer. During the chemical hydroxylation through Fenton reaction, the reaction between hydrogen peroxide and ferrous ion produces ferric ions as oxidant, and the major product is 2,3-DHBA. On the contrary, 2,5-DHBA is formed by the electrochemical oxidation.

A similar mechanism can be considered for the electrochemical hydroxylation of phenol, where OH radicals can theoretically react in positions ortho forming resorcinol and para producing hydroquinone. However, for steric considerations, a majority of catechol is produced at BDD electrode.

It is now possible to generalize this mechanism. The first step is the water decomposition:

$$H_2O \rightarrow HO^\bullet + H^+ + e^-\qquad\qquad 10.7$$

Then, the addition of OH radical takes place at the aromatic ring (R):

$$HO^{\bullet} + RH \rightarrow HO - {}^{\bullet}RH \qquad\qquad 10.8$$

Finally, the abstraction of an hydrogen atom leads to the hydroxylated product formation:

$$HO - {}^{\bullet}RH \rightarrow ROH + H^{+} + e^{-} \qquad\qquad 10.9$$

Generally, we can thus assumed that the intermediates of the hydroxylation depend on three factors: the nature of the directing group, the steric effect and the nature of the oxidant.

5.2. *COD-ICE* and γ–ν models

The *COD-ICE* model allowed to predict the evolution of the global parameters during the EOTR of organic compounds. From the concept of the limiting current density, it is possible to define two regimes (charge transfer or diffusional controls). Therefore, depending on the conditions (applied current, conversion), it is possible to obtain either partial oxidation or complete incineration of an organic compound. Both pathways can be described by the evolution of *COD* and *ICE*. For the charge transfer control, since *ICE* is equal to 1, *COD* follows a linear trend. In the case of mass transport control, both *ICE* and *COD* decrease exponentially. All equations are summarized in the following table:

Control	COD [molO$_2$ m^{-3}]	ICE [-]
Charge transfer	$COD(t) = COD^0\left(1 - \dfrac{\alpha A k_m}{V_R}t\right)$	1
Mass transport	$COD(t) = COD^0\exp\left(-\dfrac{A k_m}{V_R}t\right)$	$ICE = \dfrac{1}{\alpha}\exp\left(-\dfrac{A k_m}{V_R}t\right)$
Mixed	$COD(t) = \alpha COD^0\exp\left(-\dfrac{A k_m}{V_R}t + \dfrac{1-\alpha}{\alpha}\right)$	$ICE = \exp\left(-\dfrac{A k_m}{V_R}t + \dfrac{1-\alpha}{\alpha}\right)$

Table 10.1 Equations for the theoretical model predicting the COD and ICE as a function of time in the electrochemical oxidation of organic compounds at BDD electrode (Chapter 3).

The oxidation of organic compound like 4-chlorophenoxyacetic acid (Chapter 7) and salicylic acid (Chapters 6, 8 and 9) at boron-doped diamond electrode permitted to

validate the models.

One of interesting aspect of this model is that it has been developed for a system under galvanostatic conditions. In some processes, the oxidizing power is controlled by the applied potential. In this case, the anodic process is controlled by the applied current, which can be directly related to the flux of species.

Therefore, as seen with the γ–ν model (Chapter 3), the oxidation process can be described in terms of flux. Considering that the reaction takes place in the reaction cage, region very close of the electrode surface, we have shown that it is possible to give a model based on the production rate of hydroxyl radicals produced at the electrode (dependent to the applied current) and on the flux of organic compound from the bulk (which depends on the mass transport coefficient and the organic concentration). Supposing that *ICE* is equal to 1, the parameter γ is defined as the ratio between the production rate of hydroxyl radicals and the flux of organics:

$$\gamma = \frac{r_{HO^{\bullet}}}{r_R} = \frac{j_{app}}{Fk_m[R]} \qquad\qquad 10.10$$

The stoechiometric factor ν is defined as the ratio between the number of moles of hydroxyl radicals (equal to the number of electrons exchanged) involved in the reaction and the number of moles R (Equation 10.11):

$$\nu = \frac{\text{mol HO}^{\bullet}}{\text{mol R}} \qquad\qquad 10.11$$

On the basis of our model, Moraõ *et al.* [13, 14] validated them and proposed to describe the multi component process of oxidation by defining the fractions of current and consequently the variation of concentrations of each component. Cañizares *et al.* [15-18] have developed another model. For the model, the electrochemical reactor is divided in three interconnected zones (two electrochemical zones and one chemical) that allow the simplification of concentration profiles of compounds. The model takes into consideration the mass transfer and kinetics characteristics.

6. PERSPECTIVES

As regards of the electrochemical properties and the large applications, boron-doped diamond electrode remains a promising material for electrochemistry. The highlight of

the hydroxyl radical permitted to clarify the mechanism of oxidation process. The different reactivity of hydroxyl radicals between chemistry and electrochemistry could be applied for the synthesis of hydroxylated isomer, which cannot be produced by chemical pathway (or produced in minority).

Numerous points of BDD electrochemistry have to be yet investigated especially concerning the surface properties of diamond. The knowledge of the exact role of the diamond surface is essential to well understand and control oxidation processes. Among the actual works concerning boron-doped diamond, the manufacturing (support, technique of deposition...), the pretreatment of the surface, the use of BDD as substrate with the dispersion of particles are widely investigated.

7. REFERENCES

[1]   F. Blandini, E. Martignoni, R. Ricotti, F. Di Jeso, and G. Nappi, *J. Chromato. B*, **732** (1999) 213.

[2]   C. Coudray and A. Favier, *Free Rad. Biol. Med.*, **29** (11) (2000) 1064.

[3]   X. Luo and C. Lehotay, *Clin. Chem.*, **30** (1) (1997) 41.

[4]   J.-F. Zhi, H.-B. Wang, T. Nakajima, T.N. Rao, and A. Fujishima, *J. Phys. Chem. B*, **107** (48) (2003) 13389.

[5]   Ch. Comninellis and A. De Battisti, *J. Chim. Phys.*, **93** (4) (1996) 673.

[6]   N.V. Raghavan and S. Steenken, *J. Am. Chem. Soc.*, **102** (10) (1980) 3495.

[7]   G. Albarran and R.H. Schuler, *Rad. Phys. Chem.*, **67** (2003) 279.

[8]   C. Chen and S.-F. Shyu, *J. Mol. Struct.*, **536** (2001) 25.

[9]   J.-F. Jen, M.-F. Leu, and T.C. Yang, *J. Chromato. A.*, **796** (1998) 283.

[10]   J.B. Feix and B. Kalyanamaran, *Archives of Biochem. and Biophys.*, **291** (1) (1991) 43.

[11]   D. Wabner and C. Grambow, *J. Electroanal. Chem.*, **195** (1985) 95.

[12]   K. Omura and T. Matsuura, *Tetrahed.*, **24** (1968) 3475.

[13]   A. Fernandes, A. Morão, M. Magrinho, A. Lopes, and I. Gonçalves, *Dyes & Pigments*, **61** (2004) 287.

[14]   A. Morão, A. Lopes, M.T. Pessoa de Amorim, and I.C. Gonçalves, *Electrochim. Acta*, **49** (2004) 1587.

[15]   P. Cañizares, M. Diaz, J.A. Dominguez, J. Garcia-Gomez, and M.A. Rodrigo, *Ind. Eng. Chem. Res.*, **41** (2002) 4187.

[16]   P. Cañizares, J. Garcia-Gomez, J. Lobato, and M.-A. Rodrigo, *Ind. Eng. Chem. Res.*, **42** (2003) 956.

[17]   P. Cañizares, J. García-Gómez, J. Lobato, and M.-A. Rodrigo, *Ind. Eng. Chem. Res.*, **43** (2003) 1915.

[18]   P. Cañizares, J. García-Gómez, J. Lobato, and M.-A. Rodrigo, *Ind. Eng. Chem. Res.*, **43** (2003) 1923.

CURRICULUM VITAE

Béatrice Marselli
Ch. Pépinières, 7
CH-1020 Renens

Personal information

November 6, 1975
French
Single

Education

Swiss Federal Institute of Technology (EPFL), Lausanne, Switzerland Institute of Chemical Sciences and Engineering - Group of Electrochemical Engineering   2001 - 2004

Ph.D. in electrochemical Engineering under the supervision of Prof. Ch. Comninellis (July 2004) «Electrochemical Oxygen Transfer Reaction on Synthetic Boron-Doped Diamond Thin Film Electrode»

University of Geneva, Switzerland - Department of Chemistry

M.S., Chemistry   2000

B.S., Chemistry   1996

Professional Experience

Firmenich S.A., Geneva, Switzerland - Department of Analysis, R & D   1996

Intern for three months

Publications

B. Boye, P.-A. Michaud, B. Marselli, M.M. Dieng, E. Brillas, and C. Comninellis, *New Diam. Front. C. Technol.*, **12** (2) (2002) 63.

B. Marselli, J. Garcia-Gomez, P.-A. Michaud, M.A. Rodrigo, and C. Comninellis, *J. Electrochem. Soc.*, **150** (2003) D79.

C. Comninellis, I. Duo, P.-A. Michaud, and B. Marselli, *Application of synthetic boron-doped diamond electrodes in electro-oxidation*, in *Electrochemistry of diamond*, A. Fujishima, Editor. 2004, BKC Inc. Tokyo.

Oral Presentations

B. Marselli, Ch. Comninellis, *Oxidation of Organic compounds at Boron Doped Diamond Electrodes*, 3rd International Workshop Diamond, Braunschweig, Germany, 17th -18th May 2001.

B. Marselli, Ch. Comninellis, *Electrochemical Oxidation of Organic Compounds at BDD Electrodes*, 53rd annual ISE Meeting 2002, Düsseldorf, Germany, 15th -20th September 2002.

B. Marselli, Ch. Comninellis, *Detection of Hydroxyl Radicals during the Electrochemical Oxidation of Organic Compounds at BDD Electrodes*, 203rd ECS Meeting 2003, Paris, France, 27th April -2nd May 2003.

B. Marselli, Ch. Comninellis, *Electrochemical Hydroxylation using Boron Doped Diamond Anode*, 54th annual ISE Meeting 2003, Saõ Pedro, Brazil, 31st August -5th September 2003.